Exploratory Measurement of Recession Rates of Low Temperature Ablators Subjected to Mach 6 Flow

THESIS

Ross H. Kellet, Captain, USAF

AFIT-ENY-MS-22-M-296

DEPARTMENT OF THE AIR FORCE
AIR UNIVERSITY

AIR FORCE INSTITUTE OF TECHNOLOGY

Wright-Patterson Air Force Base, Ohio

AFIT-ENY-MS-22-M-296

EXPLORATORY MEASUREMENT OF RECESSION RATES OF LOW TEMPERATURE ABLATORS SUBJECTED TO MACH 6 FLOW

THESIS

Presented to the Faculty

Department of Aeronautics and Astronautics

Graduate School of Engineering and Management

Air Force Institute of Technology

Air University

Air Education and Training Command

in Partial Fulfillment of the Requirements for the

Degree of Master of Aeronautical Engineering

Ross H. Kellet, BS

Captain, USAF

March 24, 2022

AFIT-ENY-MS-22-M-296

EXPLORATORY MEASUREMENT OF RECESSION RATES OF LOW TEMPERATURE ABLATORS SUBJECTED TO MACH 6 FLOW

THESIS

Ross H. Kellet, BS
Captain, USAF

Committee Membership:

Mark M. Reeder, PhD
Chair

Rama S. Gorla, PhD
Member

Lt Col Robert B. MacDermott, PhD
Member

Adedeji B. Badiru, PhD
Dean, Graduate School of Engineering and Management

Abstract

The high speed/high-temperature effect of heat shield ablation was simulated in the low-enthalpy AFRL Mach 6 Ludwieg Tube using solid dry ice as a low-temperature sublimator. The experiments utilized both 21° half-angle cones and bi-conic models with a 7° half-angle leading edge followed by a 26° half-angle base contained within a cryogenic-cooled stainless steel holder. A method of fabricating dry ice test articles was developed using commercially procured dry ice and custom-made aluminum molds. Tests were performed at Mach 6.1 with a stagnation temperature of 490 K and stagnation pressures ranging from 40 - 500 psi. Unit Reynolds number ranged from 2.6 x 10^6 to 23 x 10^6 m^{-1}. High-speed Schlieren photography with a frame rate of 20 kHz was used for visualization and data analysis. Nose recession rates were determined by overlaying time-sequenced images and measuring the loss of material at the leading edge. The observed ablation rates compared favorably to previous research and were analyzed using the Fay-Riddell stagnation point heating correlation. While the test program yielded good results, there are several opportunities for improvement. One challenge was maintaining the dry ice model position and shape during the evacuation of the test section. This exploratory effort demonstrated the potential for other uses of dry ice test models in the facility, including for store separation experiments and localized particle-based flow visualization.

Acknowledgements

This work would not have been accomplished without the combined efforts of all the members of AFIT and AFRL who have supported and guided me through this process. Foremost, I would to thank my advisor, Dr. Reeder, for all of the time you dedicated to making this research successful. Thank you in particular for the many hours spent in the lab, discussing updates and avenues for further analysis, editing this thesis, and practicing the defense presentation with me. I also want to thank the members of my committee, Dr. Gorla and Lt Col MacDermott for your feedback and efforts to improve the quality and accuracy of this thesis.

This research would not have been possible without the help of the laboratory and machine shop staff. Thank you Dr. Borg for your support and all the time spent brainstorming ways to accomplish this research. To Lt Moore and Luke Hill, thank you for the long hours spent working in the LT, for answering hundreds of questions, and for adjusting the schlieren setup every time I misaligned (bumped into) a component. I would like to give a special thanks to Brian Crabtree and Chris Harkless at the machine shop. The speed and quality of your work were truly astounding. Thank you for offering your design expertise and the quick production times.

I would also like to thank the faculty and staff of AFIT for providing all of us with a rigorous, challenging, and ultimately rewarding graduate school experience despite the many challenges caused by the global pandemic. In particular, I would like to thank Dr. Polanka, who taught a quarter of my classes at AFIT. Although your final exams have likely imparted life-long trauma on me, the knowledge I gained from each of one of your classes was critical to understanding the problem that is analyzed in this thesis.

A special thanks to the boys, Jinhee and Jeff. I can't say that I loved all the late

nights spent working together on Teams, but I could not ask for a better group to do it with. I hope we have another opportunity to work together in the future.

Finally, I would like to thank my wife for your constant love and support during these past 20 months. This truly would not have been possible without you. Thank you for everything.

Ross H. Kellet

Table of Contents

Page

List of Figures

List of Tables

EXPLORATORY MEASUREMENT OF RECESSION RATES OF LOW TEMPERATURE ABLATORS SUBJECTED TO MACH 6 FLOW

I. Introduction

A resurgence of interest in hypersonic flight vehicles has spurred an increase of research. There are numerous supported efforts into overcoming the many challenges presented by operating in the hypersonic environment. Since the 1970s, heat shield research in the aerospace community has been primarily focused on the development of reusable materials, such as the ceramic tiles on the Space Shuttle. There is now a renewed focus on capsule-like designs, and with it comes a resurgence in studies on ablating heat shield designs. The coupling of shape change and aerodynamics can lead to unexpected risks in flight.

1.1 Motivation and Background

One of the primary concerns of hypersonic flight is thermal management. The Apollo command module experienced temperatures exceeding 5,000°F [9]. Most hyper-velocity crafts do not experience such extreme temperatures, however, they are generally unable to survive the hypersonic environment using conventional aircraft materials. Ablative heat shields are commonly employed to protect aircraft from high-temperature flows. Ablative heat shields protect the aircraft by absorbing energy from the flow and expending it in a solid to gaseous phase change of the shield material. Ablative thermal protection systems have proven to be reliable and capable of withstanding the extreme temperatures of re-entry conditions. However, fully capturing the chemical, thermal, and aerodynamic processes that occur around

an ablative heat shield has proven to be difficult.

There are many methods used for simulating a heat shield's operational environment, but each has drawbacks which are discussed in Chapter II. By using low-temperature sublimators, such as solid carbon dioxide (dry ice), the high-temperature environment does not need to be produced, and tests can be completed at room temperature in more conventional test facilities. This research explored the validity of testing dry ice models in a Mach 6 Ludwieg Tube.

1.2 Research Objectives

Before the present work, there was no methodology to test low-temperature ablators with a super-cooled model in the Air Force Research Laboratory (AFRL) Mach 6 Ludwieg Tube. Ideally, a repeatable, systematic process must be devised that allows low-temperature ablator models to be fabricated and tested with a high success rate. This study employed commercially produced dry ice blocks and machined molds to produce two different dry ice models. Previous work to construct dry ice models has been successfully demonstrated in the Air Force Institute of Technology's (AFIT) small supersonic tunnel, although maintaining consistent model integrity presented a challenge.

After this capability was devised, tests were performed to observe the ablation characteristics of dry ice in a hypersonic flow generated by the AFRL Ludwieg Tube. It must first be established that dry ice is operationally sound within the Ludwieg Tube. Upon proving that, the coupling of shape change and ablation patterns were investigated, as well as the possibility of using dry ice model ablation to capture boundary layer changes.

High-speed Schlieren imagery was used to provide a non-intrusive way to capture the flow and measure nose recession rates. With these images, a comparison of the

dry ice models throughout the course of the run was used to provide temporal data on the ablation process.

1.3 Organization of the Thesis

A review of literature is presented in Chapter II regarding the historical research efforts into hypersonic flight, thermal protection systems, and high and low-temperature ablative studies. Chapter III describes the test facility, the test article, the dry ice cone manufacturing process, the cooling system, and the high-speed Schlieren set-up. The overall findings of the experiments are presented in Chapter IV. Conclusions for the effort and recommendations for follow-on experiments are given in Chapter V.

II. Literature Review

Chapter II presents a background of the hypersonic flight regime and the various flow phenomena that make it both unique and challenging. The significant heat loads encountered during atmospheric reentry necessitate the use of thermal protection systems. Ablating heat shields are nearly ubiquitous in atmospheric reentry vehicles. The process of ablation is complex, and has proved to be difficult to simulate via computational and experimental methods. A variety of methods have been developed which aim to simplify analysis of the ablation process, which will be discussed in this chapter. Section 2.1 gives a broad overview of the hypersonic regime, Section 2.2 discusses thermal protection systems, Section 2.3 covers high temperature ablation studies, Section 2.4 discusses low temperature ablation studies, Section 2.5 discusses the predecessor to this research, and Section 2.6 gives a brief overview of the material properties of carbon dioxide.

2.1 Characteristics of the Hypersonic Regime

Unlike the strict demarcation between subsonic and supersonic flight, the transition from supersonic to hypersonic flow is difficult to define. The hypersonic regime is commonly simplified to flow speeds of Mach five or greater, but it is actually better defined by a variety of aerodynamic and aerothermal phenomena that distinguish it from subsonic and supersonic flight. While there are numerous features that make the hypersonic regime unique, the primary characteristics are thin shock layers, large viscous interactions, high temperatures, low densities, and entropy gradients. Each of these characteristics will be presented in the following subsections.

2.1.1 Thin Shock Layers

The region between the shock wave and the body is defined as the shock layer. Oblique shock theory predicts that for a given wedge body deflection angle, the density increase across the shock wave becomes progressively larger as the Mach number is increased. The higher density allows a greater mass flow to fit through the shock layer. For hypersonic speeds, the shock layer can be quite thin compared to supersonic flows. It follows from oblique shock theory that the shock angle of the flow will decrease as the Mach number increases. For example, an 18° half-angle wedge in Mach 36 flow will induce a shock that is only 3° wider than the body. Additionally, including the effects of ongoing chemical reactions further decreases the shock wave angle. Furthermore, a shock is closer to the body of a cone compared to a wedge due to three dimensional relieving effect. The shock wave angle can become so thin that it merges with the thick, viscous boundary layer on the body [2]. This problem is especially important at low Reynolds numbers where viscous forces dominate. While high-speed flows are typically associated with high Reynolds numbers, the low air densities often encountered by hypersonic vehicles at high altitudes can result in low Reynolds numbers. However, at higher Reynolds numbers where the shock layer is essentially inviscid, the fluid dynamic approach created by Issac Newton in 1687 becomes relevant. Newtonian theory can make accurate approximations for pressure distributions over a hypersonic body [23].

2.1.2 Viscous Interaction

High velocity flows naturally carry a large amount of kinetic energy. The flow rapidly decelerates as it progresses through the leading shock wave and approaches the stagnation regions of the forward surface of the body. Friction between the fluid elements within the boundary layer converts this kinetic energy into internal energy

and endothermic chemical reactions through a process known as viscous dissipation [34]. In turn, the temperature of the fluid within the boundary layer is significantly increased compared to a subsonic or supersonic boundary layer. For reference, typical temperature profile within boundary layers for an adiabatic wall at a wide variety of Mach numbers are shown in Figure 1b. When the wall is adiabatic, hypersonic boundary layers have wall temperatures that are over 20 times higher than a subsonic boundary layer, and become more severe with increasing Mach numbers.

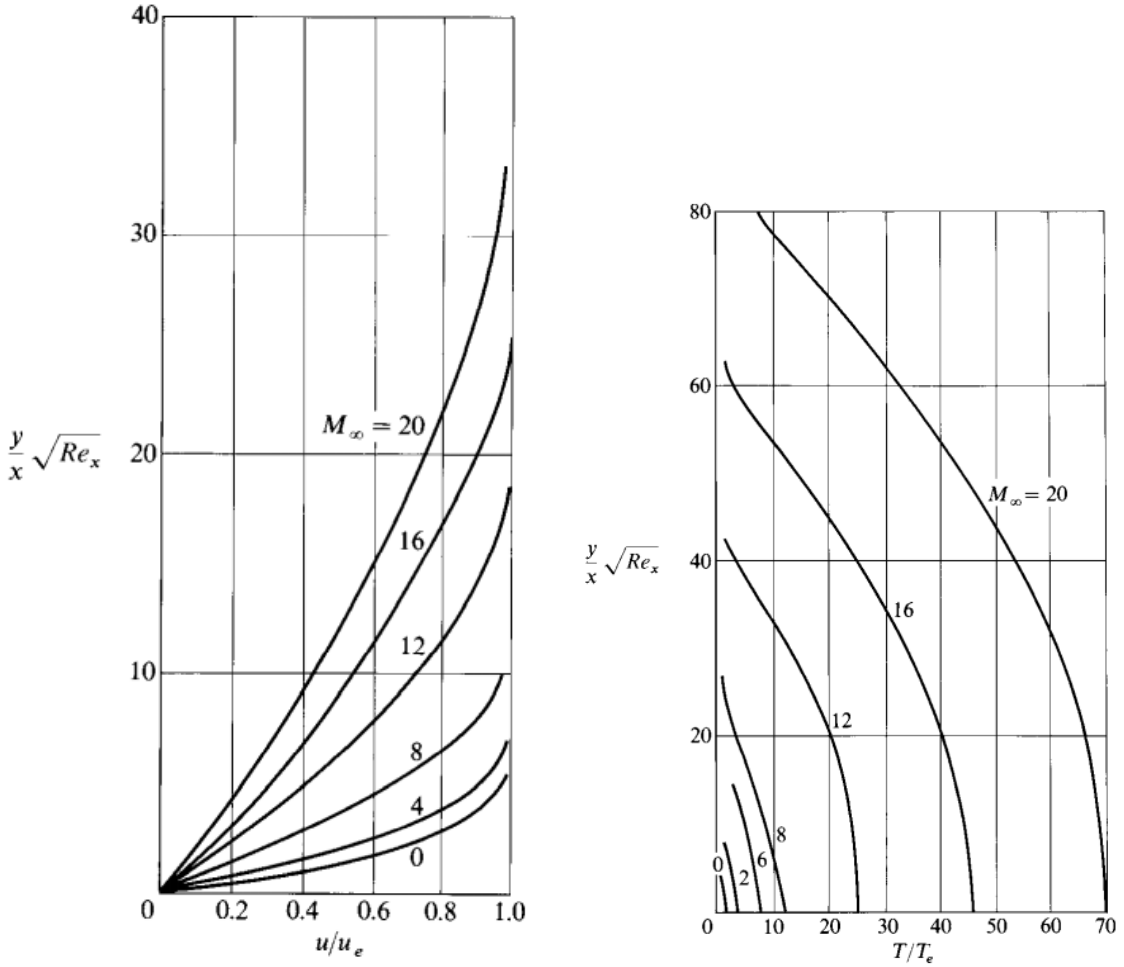

(a) Velocity Profiles **(b) Temperature Profiles**

Figure 1. Boundary Layer Profiles at Various Mach numbers for an Adiabatic Wall [33]

The characteristics of hypersonic boundary layers are dominated by the large

temperature increase. The large temperatures and Mach numbers ultimately results in significantly thicker boundary layers compared to supersonic and subsonic flows [34]. Figure 1a shows velocity profiles through boundary layers at various Mach numbers. The distance from the wall at which the local flow reaches 99% of the freestream velocity is more than double for hypersonic flows compared to supersonic or subsonic flow. The viscosity coefficient of a fluid increases with temperature, resulting in a boundary layer that will be thicker and will grow more quickly. Additionally, boundary layer theory predicts that because the pressure, p is constant in the normal direction from the body, an increase in temperature, T, results in a decrease in density, ρ, through the equation of state for a perfect gas $\rho = p/RT$ where R is the specific gas constant. The boundary layer thickness must grow in order to pass the required mass flow through at a lower density and satisfy continuity [2].

The thicker boundary layer exerts a significant displacement effect on the inviscid flow outside the boundary layer, causing an apparent thickness to the body shape [2]. The interaction between the boundary layer and inviscid flow is known as viscous interaction. Viscous interactions have notable effects on the aerodynamic properties of hypersonic vehicles. Skin friction coefficient and heat transfer rates both increase when viscous interactions are considered, further complicating vehicle designs.

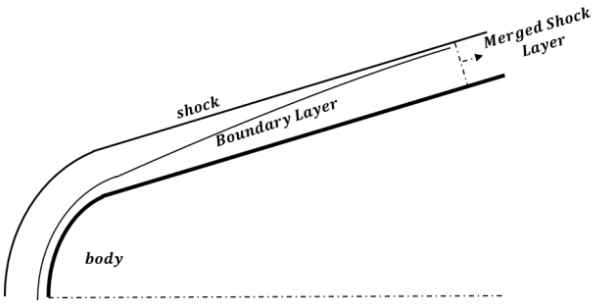

Figure 2. Merged Shock Layer [17]

At sufficiently high Mach numbers, the shock layer and boundary layers can inter-

act with each other and form a merged shock layer, as shown in Figure 2. The merged shock layer must be treated as fully viscous, and the conventional methods for analyzing boundary layers are no longer valid [2]. The boundary conditions at the edge of the merged shock layer become exceedingly difficult to define, which complicates computational models.

2.1.3 High Temperature Flows

The extreme temperatures of hypersonic flows present the greatest challenge to vehicle designers. In 1956 the fluid dynamicist E.R. Van Driest compared the "thermal barrier" of hypersonic flight to the "sonic barrier" that seemingly existed before the Bell X-1 achieved supersonic flight [34]. The constraints imparted by high temperature flows are often so severe that they become the major driving factor for vehicle design.

The first Intercontinental Ballistic Missile (ICBM) designers initially assumed that the nose shape should consist of a sharply pointed tip [23]. However, National Advisory Committee for Aeronautics (NACA) engineers made the counter-intuitive discovery that a blunt shape enjoys much lower maximum heating rates compared to sharp tip shapes. A blunt nose results in a detached shock wave in front of the body, and most of the heat is distributed throughout the flow field instead of the vehicle. Blunt shapes on hypersonic vehicles are commonplace for this reason [23]. A blunt leading edge alone does not reduce the heat transfer enough to survive hypersonic flight. Hypersonic vehicles must also incorporate thermal protection systems, such as ablative heat shields, to dissipate the heat loads imparted by the flow.

The first great challenge for computational fluid dynamics (CFD) was the "Blunt Body Problem" [23]. This problem was particularly challenging because the flow passing through the normal shock in front of the body is subsonic, but then rapidly

accelerates back to supersonic speeds. This is essentially the reverse of the transonic flow problem where some of the flow is supersonic but then decelerates to subsonic speeds. The blunt body problem was eventually solved by Moretti and Abbett using an unsteady Lax-Wendroff method [24]. With this, estimates of shock standoff distance, shock shape, and flow properties at the nose (where aerodynamic heating is highest) could be ascertained [23]. Many CFD codes, however, are somewhat limited in the ability to predict the coupled effects of high-temperature gas dynamics, fluid dynamics, ablation recession, and ablation products within the boundary layer [8].

The kinetic energy of a hypersonic flow is rapidly transferred to internal energy modes via molecular collisions. The temperature gain can be so large that the vibrational and eventually electronic modes within air molecules become excited. O_2 dissociation ($O_2 \rightarrow 2O$) begins around 2000 K, and has completely dissociated at 4000 K. N_2 dissociation ($N_2 \rightarrow 2N$) begins around 4000 K, and is complete by 9000 K [2]. These monatomic atoms will react with each other and with the surface of the vehicle. Furthermore, if an ablative heat shield is utilized, then the products of ablation will be present in the boundary layer. These processes generally result in a chemically reactive region within the shock layer. If the time required for the chemical reactions to complete or the energy distribution to equalize is on the same order as the time it takes for the fluid particle to pass over the vehicle, the flow is said to be in a nonequilibrium state, which is considerably more difficult to analyze [2]. A nonequilibrium analysis requires each chemical species to be tracked with its own continuity equation, and the chemical composition of air cannot be simply derived through temperature alone.

Tracking these chemical reactions is imperative for making accurate temperature calculations within the shock layer. In many preliminary compressible flow calculations the flow is assumed to be a calorically perfect gas which means that γ, the ratio

of specific heats, is constant. Activation of the vibrational mode of energy will cause γ to become a function of temperature. Chemical reactions within the flow will cause γ to be a function of local temperature and pressure [13]. A calorically perfect gas will have a markedly higher temperature behind a normal shock wave compared to a chemically reacting gas, as seen in Figure 3 [2].

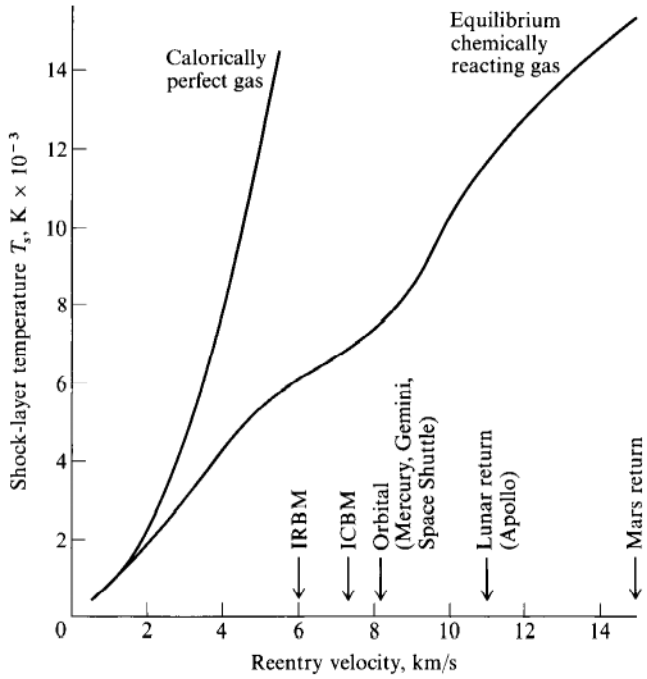

Figure 3. Temperature behind a normal shock wave as a function of freestream velocity at 52 km altitude [2]

2.1.4 Entropy Layer

Entropy of the flow increases across a shock wave, with stronger shockwaves imparting greater amounts of entropy. Blunt bodies moving at high Mach numbers will create curved bow shocks at some standoff distance from the nose.

Figure 4 depicts an arbitrary blunt body and the resulting bow shock, as well as several flow streamlines approaching the shock. Streamline a crosses a normal shock and generates the greatest amount of entropy. Streamlines b and c cross progressively

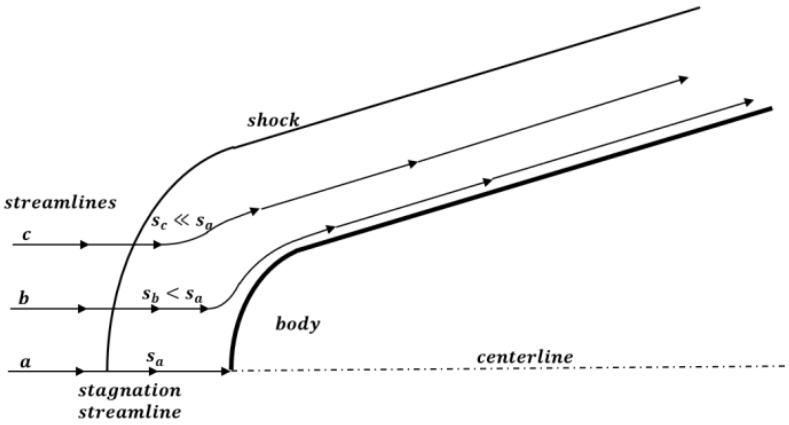

Figure 4. Entropy Layer [17]

weaker shocks and generate less entropy. The differences in entropy generated across the shock results in an entropy gradient within the flow. This region is known as the entropy layer [2]. The entropy layer is bounded by the streamline which passes through the beginning of the linear portion of the bow shock. Regions of severe entropy gradients introduce large amounts of vorticity into inviscid flows over hypersonic bodies. This vorticity can be quantified with Crocco's theorem when applied to a steady flow, $v \times w = \nabla H_0 - T\nabla S$, where v is the flow velocity vector, w is the vorticity vector, H_0 is stagnation enthalpy, T is flow temperature, and S is entropy [17]. Regions of strong vorticity will transition to turbulent and become regions of intense heat transfer.

2.1.5 Low Densities

Low density flows are not necessarily a result of any hypersonic phenomena, but are mostly a feature of the altitudes that hypersonic vehicles typically operate. At lower altitudes the amount of heat generated by viscous dissipation around a hypersonic craft would be impossible to survive with advanced materials and technologies. For various reasons, hypersonic craft generally operate at altitudes over 100,000 feet above sea level. The assumption of a fluid continuum becomes tenuous at high enough

altitudes, as the distance between individual molecules becomes substantial [2].

A variety of atypical physical effects begin to occur when the fluid ceases to operate as a continuum. Flow velocity at the surface is normally assumed to be zero in a viscous flow; this is known as the no slip condition. When the density is low enough, the flow velocity will take on a finite value. Similarly, the gas temperature at the surface is typically assumed to be the same as the surface of the body, but in a low-density flow, there will be a measurable difference. Molecular collisions lead to chemical reactions and temperature relaxation. If the density is so low that the rate of molecular collisions is significantly decreased then the flow is referred to as "frozen." In a frozen flow, chemical reaction rates tend toward zero, and relaxation times approach infinity [2].

2.2 Thermal Protection Systems

Thermal protection systems (TPS) are most simply described as the vehicle subsystem which reduces the heat exchange from the hypervelocity flow through the surface of the body to an acceptable range. TPS accomplish this by blocking, absorbing, and radiating heat away from the vehicle. The most common types of TPS are radiative, insulative, and ablative [9]. Ablative heat shields are by far the most utilzed due to their performance and cost. Ablative heat shields are generally lightweight, efficient, and decades of successful flights have proven them to be highly reliable for re-entry. The ablation process is self-initiating and self-regulating; there is no need for sensing, control, or distribution systems to manage the TPS [30]. Ablative heat shields were used on the first Gemini missions, the Apollo lunar missions, and recently on the SpaceX Dragon crew capsule [10]. Figure 5 shows the maximum operating temperatures for a variety of thermal protection materials, including materials used on the Gemini, Apollo, and space shuttle missions. The ablative systems are favored

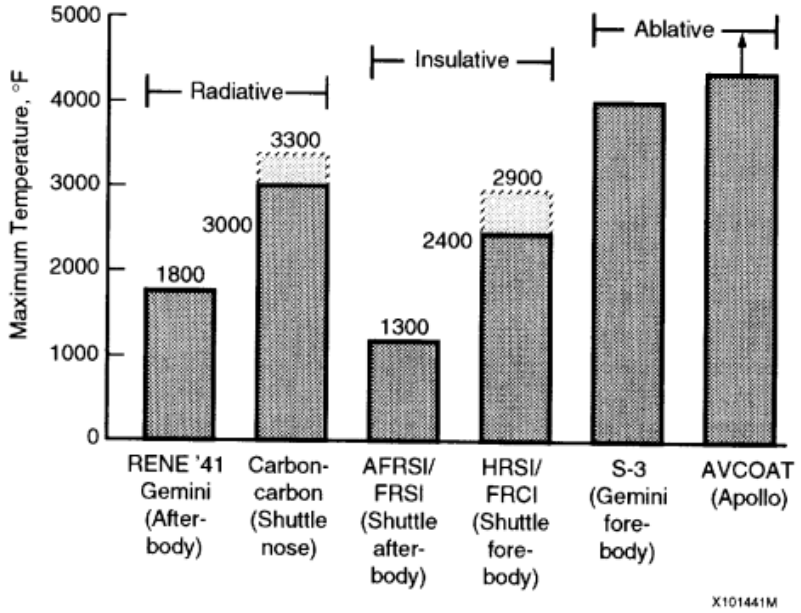

Figure 5. Thermal protection material operating temperatures [9]

due to their high maximum operating temperature compared to radiative and insulative. The AVCOAT heat shield used on the Apollo command module was capable of withstanding temperatures in excess of $5000°F$ (3000 K), whereas the Reinfoced Carbon-Carbon (RCC) material at the space shuttle nose (where the highest temperatures are encountered) could only withstand $3000°F$ (1900 K)[5]. The TPS material was determined by the local heating environment, which is influenced by both the re-entry mechanics and the location on the vehicle. The higher operating temperature of ablative materials was especially important during the early days of space flight where there was still a great amount of uncertainty in the maximum heat loads during re-entry [29]. For this reason, ablative materials have garnered many studies. Despite the number of studies, characterization of the ablative process still remains a challenge and will be the focus of this thesis.

2.2.1 Ablative Thermal Protection Systems

According to Hankey [15], ablation is a heat absorption method in which the material absorbs heat and undergoes a phase change from solid to gas. The equation for the energy balance is $Q = h_v \Delta m$, where Q is the heat transferred, h_v is the heat of vaporization, and Δm is the mass loss through ablation. Materials with a high heat of vaporization and low density are selected to minimize the weight of the TPS. Graphite and phenolics are materials currently in use; Teflon and AVCOAT were used in early ICBMs and re-entry vehicles [15]. One goal of this research is to determine if the low temeprature sublimation of dry ice in combination with the AFRL Ludwieg Tube at Mach 6 can be used for ablation testing. Subsequently, refinement of the approach might be useful for predicting ablation traits of high-temperature materials.

The two main ablators of interest for this research are sublimating and charring. Subliming ablators decompose directly from the solid to the gaseous phase. The process of sublimation consumes a significant portion of the energy entering the surface. Ablative TPS have the added benefit of inserting cooler gas into the boundary layer, which further protects the vehicle downstream via transpiration cooling. The vehicle is protected by the energy absorption during phase change and by the reduction of convective heat flux by the transpiration effect [30]. Graphite and Teflon are the most common subliming ablators. Teflon is a moderate temperature ablator and its performance is well characterized. Ablation is typically measured in units of millimeters per second. A Teflon shield will change its shape considerably during the course of operation as the surface gradually ablates [30]. Graphite is a high-temperature sublimator and has a relatively low ablation rate, roughly 10% of the value for Teflon's in similar conditions. This can be advantageous to minimize the shape change in areas of high heating rates, but it reduces the benefit of transpiration cooling [30]. A drawback of both Teflon and graphite is they are brittle and have a low resistance to

thermal stress [30].

Charring ablators undergo a more complicated process. As the surface temperature of a carbon-based ablator reaches around 800 K, the material begins to decompose, or pyrolyze, and releases gaseous products. The decomposition leaves a porous, carbonaceous residue. Pyrolysis does not require oxygen, so as the heating continues the pyrolysis zone proceeds deeper into the material. Gaseous products from within diffuse up through the porous char and carry energy away. These products enter into the boundary layer, where they act as a transpirant and may undergo additional chemical reactions within the boundary layer [30]. The char continues to absorb heat until it reaches the temperature at which it oxidizes or sublimes. The thick char will act as an insulation barrier, and will also radiate heat away from the surface. However, like the subliming ablators, char is brittle and is susceptible to rapid removal by mechanical shear and spallation [30]. Reinforcing fibers are usually added to the ablative resin to preserve the char layer, but this adds complexity to the ablation model and increases the thermal conductivity at the surface.

2.2.2 Challenges of Modelling Ablative Thermal Protection Systems

The most effective tests are performed under true flight conditions in operationally relevant environments. Flight tests are generally expensive for reentry vehicles. Instead, most preliminary research aims to recreate a realistic flight environment within a laboratory. Reentry conditions, however, are so extreme that it is difficult and expensive to recreate them in a wind tunnel.

Reentry vehicles simultaneously encounter large stagnation pressures and thermal loads, but no single tunnel facility can fully duplicate the complete flight environment [30]. Figure 6 shows the flight envelopes of several different reentry vehicles as well as the testing capabilities of several different facilities. Arc-jet facilities are commonly

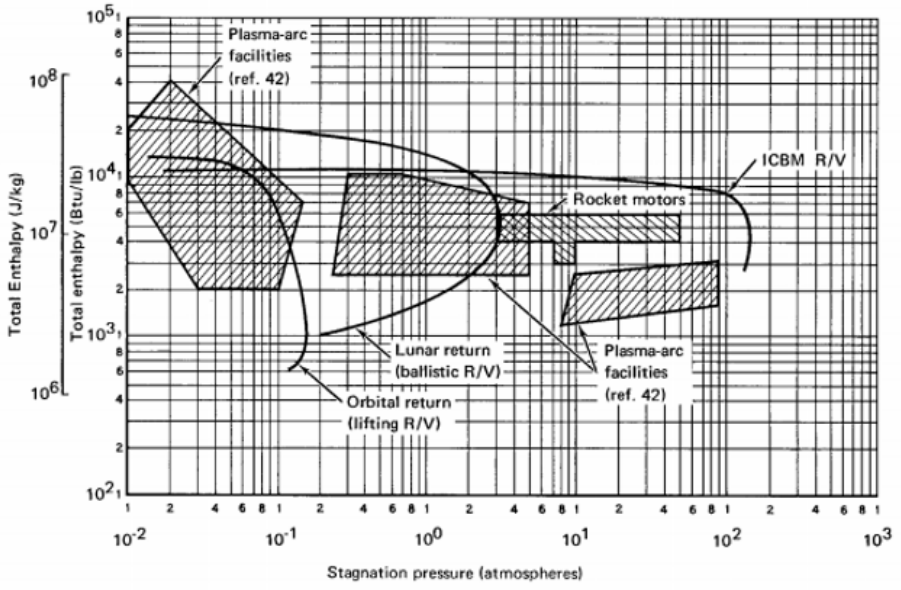

Figure 6. Comparison of Flight and Ablation Test Facility Performance Parameters [30]

used to perform ablation studies. Arc-jet facilities use an electric arc to heat the flow up to 8000 K [16]. As seen in Figure 6, these conditions can meet and even exceed the flow enthalpy encountered in flight. However, these facilities cannot create the high Mach numbers and pressure loads that are sustained during flight. Additionally, the brightness of the stagnation region makes it difficult to capture the fine details of the model edges without post-processing.

Alternatively, ablation studies have utilized rocket motors to model the flight environment. Figure 6 also shows that rocket motors can nearly simulate hypersonic flight conditions. Like the arc-jet facility, capturing images within the exhaust plume is difficult. For this reason, many rocket motor results only present qualitative data. Additionally, the exhaust of the rocket motor will consist of combustion products, instead of just air [30]. This limits the many chemical reactions that would otherwise occur in the boundary layer from being replicated.

Computational fluid dynamics (CFD) has progressed significantly since the "blunt

body problem" that was solved during the 1960s. It has become ubiquitous in both the academic and commercial environment. Computational aerothermodynamics (CA) is the sub-field of CFD which emphasizes high-temperature effects on pressure, skin friction, and heat transfer [14]. It is especially focused on conditions of hypersonic velocities where the exchange of energy between the kinetic, internal, and chemical modes precludes the use of calorically perfect gas assumptions. Despite advances in the past several decades, the ablating-model poses several difficult challenges for modeling of flow around an ablating model and the subsequent pattern of ablation. Turbulence remains one of the great challenges of aerodynamics. Regions of turbulent flow create extreme thermal loads [34]. Accurate predictions of the transition region from laminar to turbulent are essential to making accurate heating calculations. According to Gnoffo [14] and Cummings [8], CA cannot reliably predict transition to turbulent flow, either naturally occurring or resulting from trips in the boundary layer. Only preliminary attempts have been made to model ablation, and time-dependent shape change has not been fully automated [14]. As the model ablates, the surface roughness will increase and the overall shape will change. The shape change will result in a different shock angle, and the increased surface roughness will accelerate the transition to turbulence. Even state-of-the-art systems make numerous assumptions to simplify conditions or ignore transient effects [14].

More recently, Cummings [8] summarized the state of recent hypersonic CFD efforts and challenges that lay ahead. Cummings identified "significant physical modeling deficiencies" in multiple domains of high-speed codes, specifically in the use of low-speed turbulence models and the lack of effective boundary layer transition models. A blind study conducted by the American Institute of Aeronautics and Astronautics (AIAA) which compared numerous flow predictions to experimental data showed that very few codes were capable of predicting heat transfer even marginally

well [8]. While they certainly play a key role, CA and CFD alone are not sufficient to fully examine the ablation process. Other methods must be developed to better understand the transient effects of ablation.

2.3 High Temperature Ablation Studies

One common ablation patterns observed on recovered flight vehicles, ballistic range models, wind-tunnel models, and even meteorites have criss-crossed grooves. These grooves give the appearance of a crosshatched, diamond-shaped pattern to the surface [22]. Nachtsheim and Larson [25] sought to understand the mechanisms that create this phenomenon. They utilized a hydrogen-oxygen rocket motor operated at a stagnation pressure of 1,000 psia and at an oxygen-fuel ratio of 5 in order to simulate the re-entry environment. The motor had an expansion ratio of 8.5 and an exit diameter of 5 inches. The models were 7° half-angle cones approximately 1 ft long with a $\frac{1}{16}$ in initial nose radius. Figure 7 shows a Teflon model before and after 3.5 seconds of exposure to the rocket engine. Steel tips were used to prevent ablation at the nose of the model and maintain a relatively constant leading shock angle. Moving down the model, there is significant necking around the midpoint of the cone followed by a distinct crosshatched surface pattern that ecompasses the bottom half of the model. Crosshatching was observed when the average surface recession rate of the model reached 0.05 in/sec [25].

Nachtsheim and Larson [22] postulated that the underlying cause of crosshatching is the interaction between supersonic flow at the edge of the boundary layer and a turbulent boundary layer adjacent to the surface. As the flow progresses down the cone it gradually transitions from laminar to turbulent. The heat transfer coefficient rapidly increases within the transition region and then levels off when the flow is fully turbulent. The peak heat transfer rate causes the necking seen in Figure 7, and the

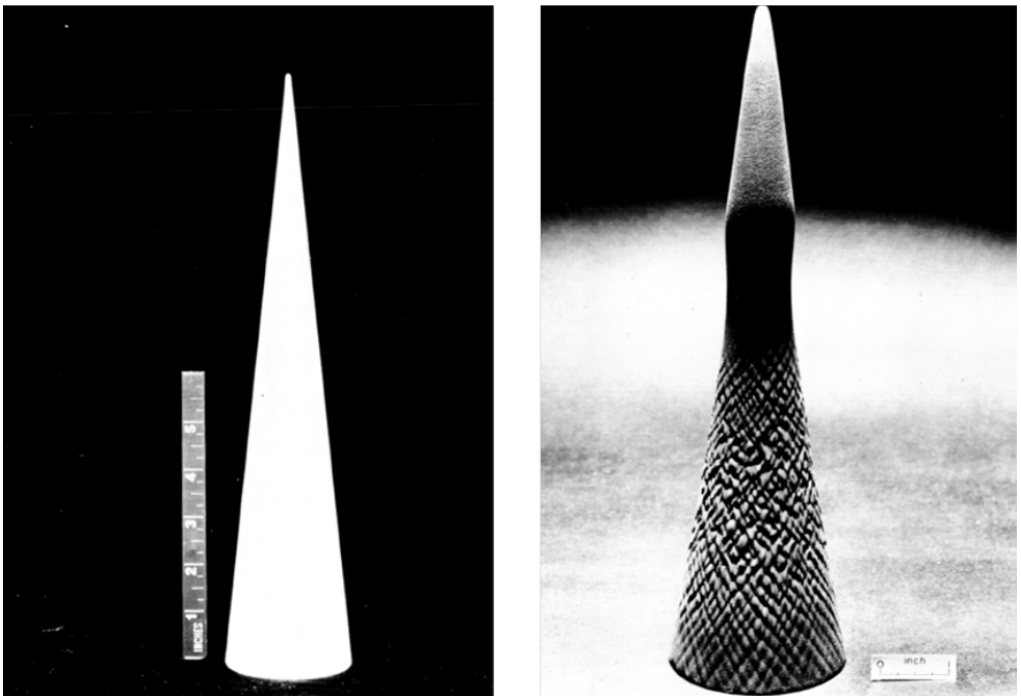

Figure 7. Teflon test article before and after exposure to rocket engine [25]

large heat transfer rate combined with the turbulent boundary layer and supersonic flow interaction creates the crosshatch pattern [25].

Laganelli and Nestler [21] also studied the phenomenology of surface ablation patterns. The authors similarly used a rocket exhaust facility consisting of two jets. The first jet had an effective 4 inch diameter flow core with a freestream Mach number of 2.36, a stagnation pressure of 258 psia, and stagnation temperature of $5,800°R$ (3200 K). The second jet had an effective 15 inch diameter flow core with a freestream Mach number of 2.87, a stagnation pressure of 565 psia, and stagnation temperature of $5,800°R$ (3200 K). The tests were monitored by 1000 frames/sec Fastex cameras and two Millikan cameras at 400 and 128 frames/sec. The authors used several conic models composed of melting, subliming, and char forming materials with half angles varying from 6° to 13° and a nose radius of $\frac{1}{8}$ to 2 inches. The models included a small machined ring to accelerate the transition from laminar to turbulent flow. The authors also concluded that supersonic, turbulent boundary layers were necessary for

the crosshatch pattern to form. Additionally, the authors found that materials with higher ablation rates required less time for the patterns to form. It was observed that a conic model composed of phenolic nylon exhibited a crosshatch pattern within 2 seconds, but a graphite model did not show the pattern with a 25 second exposure time. Finally, a wide variety of body shapes, tip bluntness, and surface disturbances did not appear to alter the pattern geometry or propagation [21].

2.4 Low Temperature Ablation Studies

While simulating the test environment is often desirable, it may not be necessary if alternate means can accomplish the same goal. While the effects of chemistry on ablation may not be captured with a low-temperature ablator (LTA), valuable shape change information can be ascertained. Both facility requirements and model design are more forgiving for LTAs, and so they are often found to be a useful complement to hypersonic research programs. High enthalpy test conditions are needed because ablative TPS materials sublimate at thousands of degrees Kelvin. There are numerous materials, however, that undergo sublimation at much lower temperatures. Camphor, Naphthalene, water ice (H_2O), and dry ice (CO_2) each sublimate at temperatures below 500 K under certain conditions, which is easily achievable in many wind tunnels. Verifying that LTAs can adequately simulate high-temperature ablation would lessen the need for expensive high enthalpy tests and simplify the collection of temporal recession and boundary layer data. This section will give an overview of previous research that was accomplished using low-temperature sublimators to model high-temperature ablation.

One of the earliest investigations in the viability of LTAs was done by David Anderson in a 1960 master's thesis at California Institute of Technology. Anderson [1] experimented with dry-ice, water ice, and camphor ice ($C_{10}H_{16}O$) in the GALCIT

hypersonic wind tunnel at Jet Propulsion Laboratory (JPL). Anderson manufactured the models by compressing crushed dry ice into 1-inch diameter hemisphere cylinder molds. Runs were performed at Mach 5.8, 422 K stagnation temperature, and 2 atm stagnation pressure, and at Mach 8, 755 K stagnation temperature, and 3.7 atm stagnation pressure. The models were pushed into the wind tunnel once the flow had come up to temperature. Anderson experienced what he called "flaking" on the surface of the dry ice models where large shard s of material were lost by fragmentation. For this reason, Anderson was not able to produce quantitative data with the dry ice models. Anderson obtained quantitative data through time-lapse photos with a 35mm single-lens reflex camera fitted with a 135mm telephoto lens in runs lasting 30 - 40 minutes. The observed recession rates of water ice and camphor were between 30% and 50% less than predicted by theory. The largest source of error identified was the lack of picture sharpness due to oil on the wind tunnel window [1].

Another early investigation into low-temperature ablation is in a paper by Kohlman and Richardson [19]. The primary focus of their work was to develop a method for fabricating dry ice wind tunnel models and to determine the feasibility of using such models to study ablation. Kohlman and Richardson [19] list six reasons for utilizing dry ice:

- Its sublimation temperature ranges between 143 and 195 K for static pressures between 1 to 10^{-3} atm give a large range of test conditions in unheated tunnels
- The vapor pressure over the low temperature range is of the same order as high temperature ablators
- Its high triple point (214 K, 79 psia) allows sublimation over a wide range of test conditions and eliminates melting during fabrication and storage
- The ablation products are simple and safe (CO_2)

- Favorable simulation parameters
- Its heat of sublimation is low (248 Btu/lb at 1 atm)

These characteristics make dry ice especially suitable for studying boundary-layer phenomena and dynamic characteristics of an ablating model. They utilized three methods for constructing 0.75 inch hemisphere cylinders: carving commercially procured dry ice blocks, freezing liquid CO_2 on a mandrel in a mold, and directly freezing gaseous CO_2 in a low-temperature mold. The authors also utilized an insulated sting to prolong the model life. Tests were run at Mach 2.38 with air drawn from the atmosphere at approximately standard atmospheric conditions into vacuum tanks. Recession rates were determined through photographs taken at one second intervals. The observed recession rates were within 10% of the rates predicted by theory, and the models were able to withstand the aerodynamic loads [19].

In 2017, Combs et al. [7]utilized a 50.8mm scaled National Aeronautical and Space Administration (NASA) Orion Multi-Purpose Crew Vehicle (MPCV) model made of aluminum with a napthalene heat shield to visualize the ablation process. The authors developed a technique to capture the ablation-product transport in a supersonic flow using planar laser-induced fluorescence (PLIF). PLIF is a non-intrusive flow diagnostic that enables imaging of the two-dimensional distribution of a chemical species in a flow. PLIF uses a laser sheet to measure a slice in the flow containing the species of interest. In this case, an ultraviolet (UV) laser was used to excite the vaporized napthalene molecules, resulting in fluorescence that is detected by a digital camera. NASA researchers have previously used PLIF to visualize NO gas inserted through ports in a model to simulate ablation [7]. An advantage of using a LTA is that the transported products are the result of mass transfer from the heat shield itself [7].

The facility used for the experiment described by Combs et. al [7] was a low-enthalpy blowdown Mach 5 wind tunnel. The stagnation temperature was 360 K

and the plenum pressure was 2.5 MPa. The freestream unit Reynolds number was $57.2 \times 10^6 m^{-1}$ and a freestream velocity of 770 m/s. The Reynolds number based on the model diameter was 2.9×10^6. Figure 8 shows a time sequence of PLIF images at 0° angle of attack over the course of 60 seconds. In the first image, the shear layer appears to be laminar with turbulent eddies begin to form further downstream. As time progresses, the turbulent structures can be seen progressing further upstream. In Figure 8f the shear layer appears to have completely transition to turbulence. The napthalene PLIF signal increases significantly over the course of the run. This is a result of the heat shield warming during the run. The sublimation rate of napthalene increases substantially as the model heats up, leading to increased concentrations of napthalene vapor in the flow. Given that the freestream Reynolds number is effectively constant during the run, the onset of turbulence is most likely due to changes in the heat-shield surface as a result of the ablation process. As the shield ablates, the surface will become rough which accelerates transition to turbulence. Additionally, the mass transfer rate (or blowing rate) of the napthalene vapor increases over the course of the run, which could also affect turbulent transition [7].

Figure 9 shows a time sequence of PLIF images on the center of the heat shield at 52° angle of attack. Again, it can be seen that the concentration of napthalene increases as the run progresses as do the sizes of the turbulent structures. The intensity of the PLIF signal alone cannot be directly converted to mole fractions. The authors used the FUN3D solver to calculate temperatures and pressures throughout the flowfield. The authors compared the shock standoff distance and the shear-layer angle with the PLIF visualizations and schlieren imagery to validate the code. The authors were able to use the temperature and pressure data to convert the PLIF signal to a mole fraction fields. They found that the uncorrected images were similar to the calculated data in a qualitative sense and gave a general representation of the

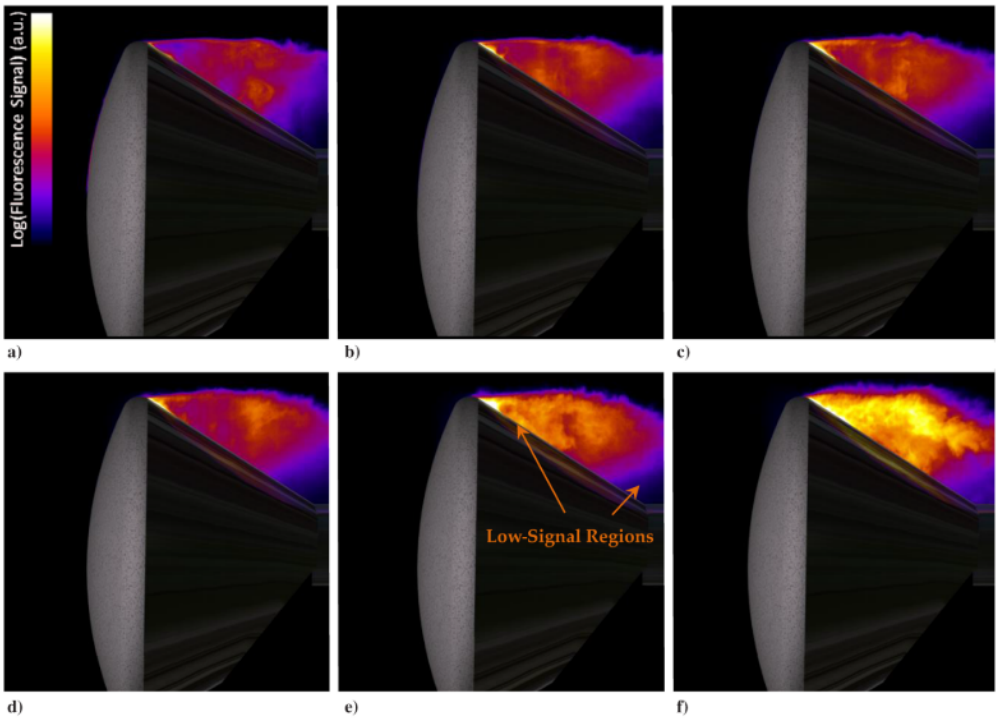

Figure 8. Napthalene PLIF at 0 deg Angle of Attack. Images are sequential in time, separated by 10 s [7]

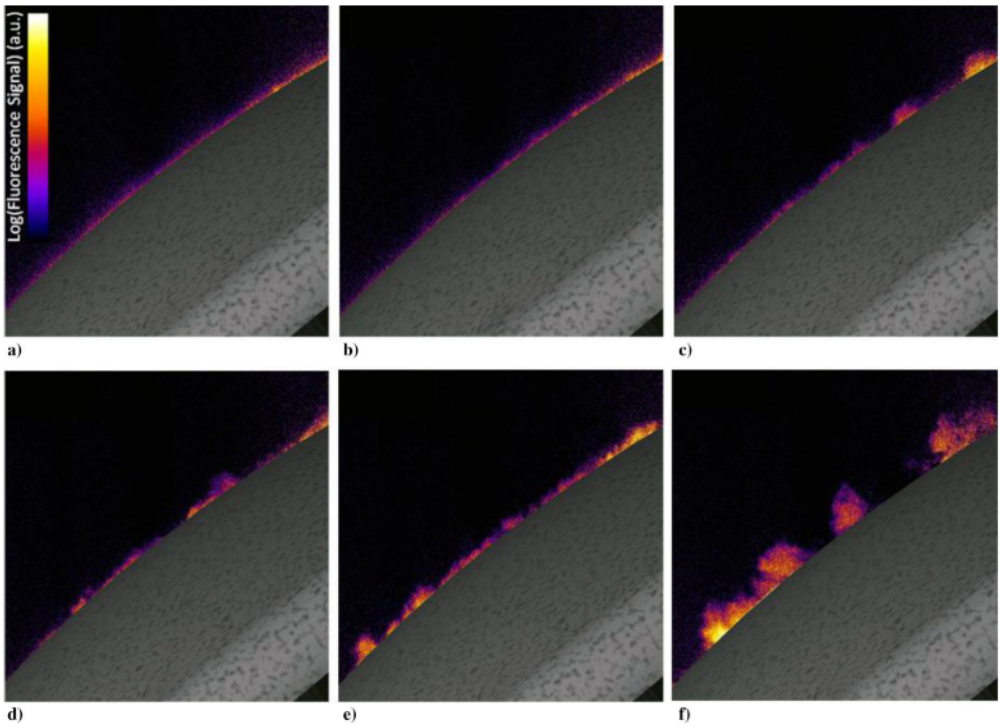

Figure 9. Napthalene PLIF at 52 deg Angle of Attack. Images are sequential in time, separated by 6 s [7]

flow field mole fraction. Finally, the authors were able to capture the effects ablation had on the transition to turbulence and heat transfer on the shield surface. However, the choice of Naphthalene combined with the limits in test run tine prevented the shape change from being quantified in this effort [7].

There have also been numerous computational studies with low-temperature ablators in addition to experimental research. One such study was performed by Zibitsker et al [35]. which sought to create a coupled fluid and material response solver that could accurately model surface ablation in a hypersonic flow. The simulation utilizes two flow solvers to efficiently compute conditions of the off-body flow-field and within the boundary layer, as well as a 1-dimensional fluid ablation interaction (FAI) solver. The fluid and material response solvers exchange a full set of boundary conditions at a shared interface [35].

Ablation of a camphor sub-scale model of the Phoebus capsule in Mach 6 flow at three different stagnation pressures of 15, 20, and 25 bar were examined. The results of the computational simulation were compared to recession rates captured on the same model at the H3 hypersonic wind tunnel at the von Karman Institute for Fluid Dynamics. Overall, the computational model was able to provide accurate predictions of stagnation point recession rates for roughly half of the 30 second long runs. It was found that high uncertainty in the estimations of transport properties caused difficulties in modeling the physical behavior of the system. The diffusivity of the ablated material, in particular, had a considerable effect on the resulting thermal response of the material. Higher diffusion rates led to a lower partial pressure at the wall which resists the sublimation process [35].

2.5 Air Force Institute of Technology Study

The primary predecessor for this research was conducted by Callaway [5] in 2011. The objectives of Callaway's research were to reliably fabricate test articles, capture ablation recession in three dimensions, and compare the result to computational modeling performed by Air Force Research Laboratory (AFRL). The wind tunnel used was the AFIT blow-down facility. The test section was 6.4 x 6.4 cm, and the Mach 2.94 convergent-divergent nozzles were used. The test chamber had a stagnation pressures ranging from 6 to 48 psia and a stagnation temperature of 293 K. The low pressure and high pressure tests had unit Reynolds numbers, Re_L, of 3.33×10^6 and 2.56×10^7 respectively. The test section was lengthened to 15 inches and a window was added for a third camera viewing angle. A custom designed sting was fabricated and can be seen with a dry ice model in Figure 10. The sting had an internal tube that served to deliver liquid carbon dioxide to the mold for model fabrication and to cool the sting to prevent heat transfer. The spherically blunted cone also seen in Figure 10 has a base diameter of 0.60 inches. This model was used for a majority of the test runs [5].

Three MotioPro X-stream XS-4 high speed cameras with a resolution of 512x512 and a frame rate of 5,000 frames/sec were used to capture images of the test. Callaway used laser dot projection photogrammetry to capture three dimensional recession data. A laser grid is projected onto the surface of the test article. As the surface ablates, the cameras can capture changes in the dot location. Using this data, Callaway was able to generate three dimensional computer models and track their recession rates over time. Figure 11 shows the laser grid projected onto the dry ice model. Schlieren imaging was also used to capture the changing shock location as the nose of the model ablated [5].

Nose recession rates of the experimental data was compared to the ablation com-

Figure 10. Spherically blunted cone model and sting [5]

putational fluid dynamics (ACFD) solver. Callaway found that higher stagnation pressures resulted in greater observed recession rates. This finding was also predicted by the ACFD solver. A comparison of the CFD and experimental results are shown in Figure 12. The greater stagnation pressures resulted in greater nose recession, but the increased dynamic pressures also tended to lead to model breakup relatively early in the runs, often before 3 seconds had elapsed. One of the main contributors to the number of model breakups was the relatively low density of Callaway's manufactured dry ice cones, which were formed on-site from liquid CO_2. Callaway's dry ice model density was measured to be around 1 g/cm, compared to 1.5 g/cm that is typically seen in commercial dry ice which is formed under higher pressures. Overall, the recession rates predicted by the ACFD solver were within about 10% of the experimental results. However, as test times increased the experimental results began to diverge from the computational predictions, with the CFD models mildly over-predicting recession rates [6].

Overall, Callaway demonstrated during the course of over 100 wind tunnel tests that repeatable experiments were possible with dry ice models. Additionally, Callaway was able provide insight into the validity of a coupled computational model, which predicted shape change under limited conditions. Ultimately, the next step will be to attempt to conduct repeatable tests and measure ablation rates for a dry ice model at high Mach numbers, and to make improvements on the dry ice model production process.

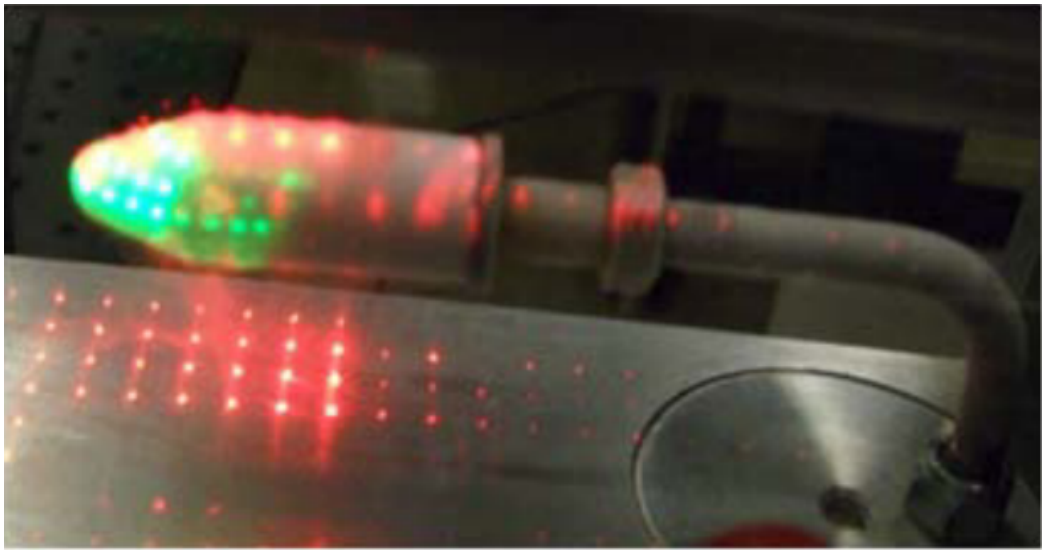

Figure 11. Laser grids projected onto a spherically blunted cone dry ice model [5]

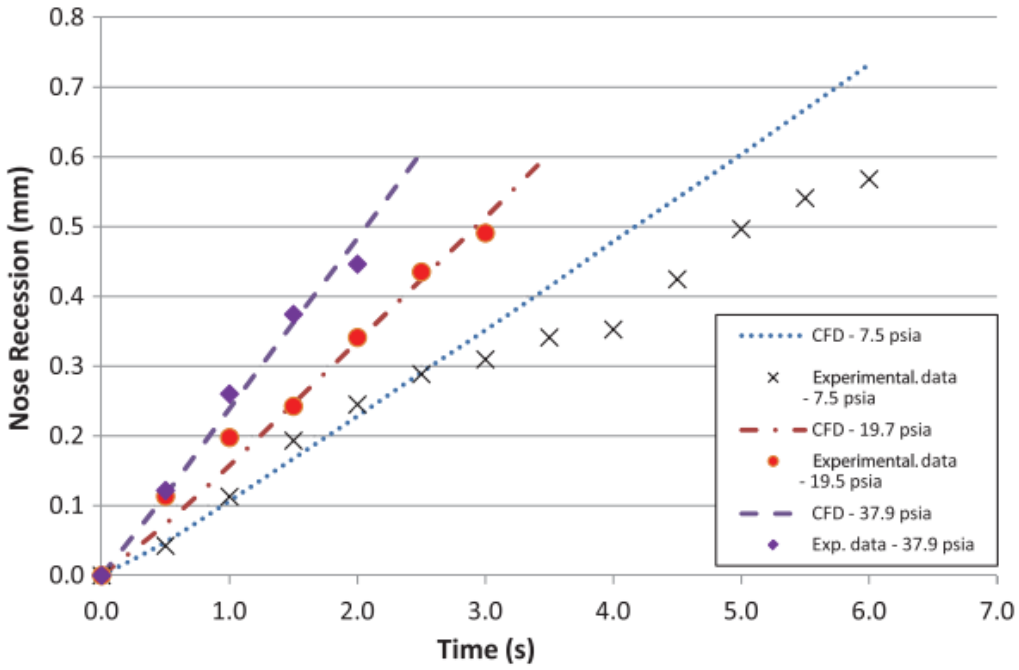

Figure 12. Comparison of measured and computed stagnation point recession of a spherically capped cylinder [6]

2.6 Material Properties of Solid Carbon Dioxide

While it is traditionally used for refrigeration, dry ice has properties that make it useful for studying ablation. A phase diagram of carbon dioxide can be seen in Figure 13. Carbon dioxide has a triple point (where all three phases of a substance may be present) at 216.6K and 5.11 atmospheres (75.1 psi). At room temperature, the solid will attain a temperature of 194.65K and will directly sublime to gas as heating continues. The low sublimation temperature is the reason for exploring the use of dry ice to simulation high temperature ablators. As seen in the highlighted portion of the phase diagram, the carbon dioxide model will not experience conditions that would cause melting instead of sublimation [5]. Though water ice has been used in some studies, melting can affect the experimental outcome.

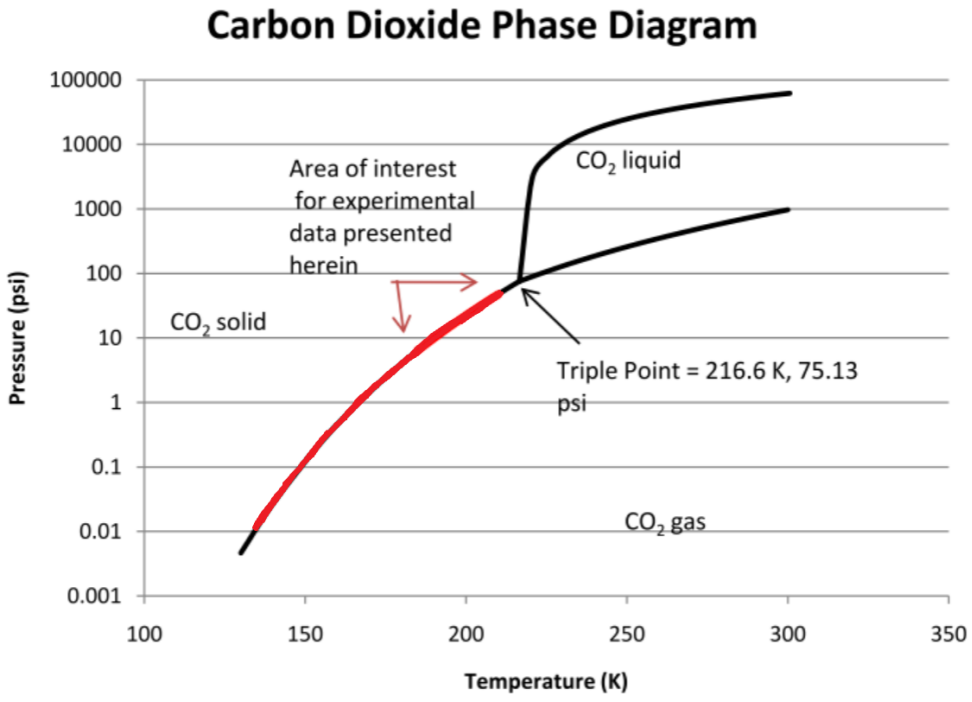

Figure 13. Carbon Dioxide Phase Diagram (from [5])

2.7 Experimental Design Differences

There are several fundamental differences between the experiments carried out by Callaway and the experiments conducted within the Ludwieg Tube. The first difference is the average run time. Callaway was able to measure recession rates over the course of 7.5 seconds, but the Ludwieg Tube can only capture, at most, 0.2 seconds of usable data. Second, this experiment uses a different model fabrication process and dry ice density. This experiment utilized commercially procured dry ice which has a significantly higher density compared to Callaway's produced ice. Third, the stagnation temperatures and pressures in this experiment are much higher than Callaway's. Callaway's experiment was conducted at a stagnation temperature of 290 K, and a maximum stagnation pressure of 46 psi. The Ludwieg Tube has a stagnation temperature of 490 K, and can produce stagnation pressures between 40 and 500 psi for this experiment. Fourth, the Mach number for this experiment was 6.1, compared to Mach 2.94 in Callaway's. Finally, the scale and shape of the models are different. Callaway utilized a variety of shapes, but the models were typically 0.6-inch base diameter and 1.2 inches long. The models in this experiment were approximately 3 inches long and had a 2-inch base diameter. While this experiment relies heavily on Callaway's research, most of the relevant parameters and testing conditions exceed what was achievable in Callaway's experiments and are predicted to yield novel results.

III. Methodology

Chapter III presents the methodology that was used to accomplish this experiment. Section 3.1 provides details of the experimental facility. Section 3.2 develops the equations to determine flow conditions. Section 3.3 describes the test article manufacturing process and holder, followed by the method by which liquid nitrogen (LN2) was integrated to cool the holder to reduce sublimation between tunnel runs in section 3.4. Section 3.5 covers the high-speed schlieren setup, Section 3.6 covers the image analysis process, and Section 3.7 offers a discussion of safety post-experiment.

3.1 Experimental Facility

The tests in this study were conducted in the Air Force Research Laboratory (AFRL) Ludwieg Tube located at Wright-Patterson Air Force Base, OH. A rendering of this facility can be seen in Figure 14. Previous work by multiple authors has demonstrated that the facility produces 200 ms of Mach 6.1 core flow spanning 25 inches of diameter. This flow is divided into two quasi-steady states of about 100 ms each, separated by an expansion-wave passage. The unit Reynolds number range of the Ludwieg tube is 2.1 x 10^6/m to 30.1 x 10^6/m at a driver pressure of 50 psi and 580 psi respectively [18].

The Ludwieg tube itself is composed of two principal parts: the high-pressure stagnation chamber and a vacuum section consisting of a nozzle and test section. The two sections are separated by an actuating fast valve. The fast valve is released once the test section has reached a vacuum and the stagnation chamber has reached the desirable pressure. Upon actuation, high-pressure fluid flows from the high-pressure to low-pressure sections through a nozzle, effectively creating a steady condition. This produces an expansion wave that propagates up and reflects down the driver tube.

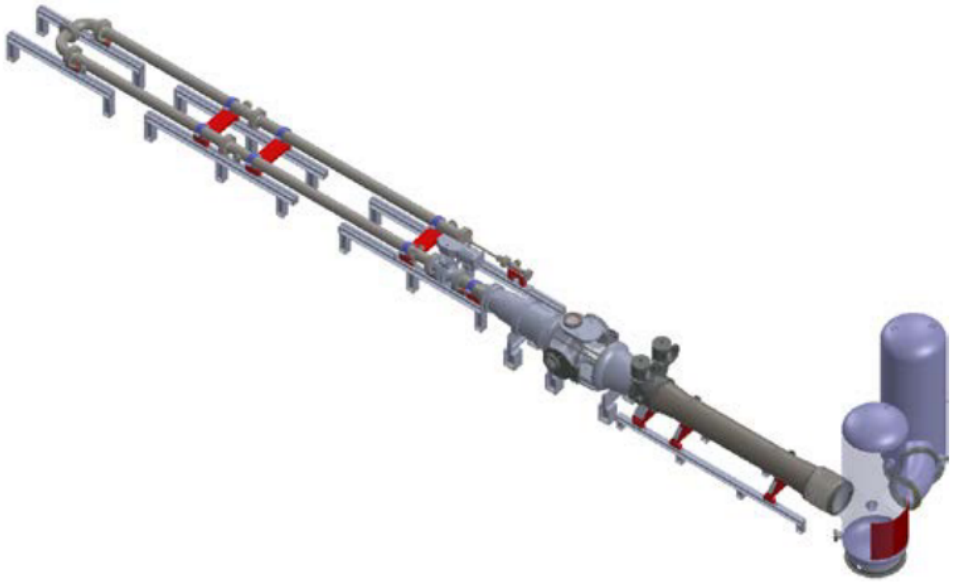

Figure 14. Rendering of the AFRL Ludwieg Tube [18]

Multiple periods of uniform flow can be formed with sufficient pressure. The AFRL Ludwieg tube produces two quasi-steady states of about 100 ms each. The second quasi-steady period has a slightly lower unit Reynolds number due to a change in stagnation properties after the pass of the expansion-wave [18].

The driver tube is brought up to pressure by two 27 HP compressors. A commercial 18 kW resistance heater raises the inlet air temperature to 500K prior to filling the driver tube. The compressors run continuously during operation. After the driver tube is brought to the desired pressure, a bypass valve opens and dumps compressed air outside. This assures that the maximum pressure in the system is no higher than the driver tube rating. This removes the need for an accumulator tank and minimized compressor starting and stopping [18].

The driver tube consists of 304 stainless steel pipe. The driver tube is comprised of two 20 ft and two 15 ft sections, joined by two 90° elbows, forming a 180° U-bend. This reflexed driver tube configuration has been previously used on several Ludwieg tubes [18]. The driver tube air used during the two quasi-steady periods originates

from the first 30 feet of the driver tube nearest the nozzle. The entire length of the driver tube is heated to 500K to minimize convection and driver tube diameter changes required for non-uniform heating [18].

The Ludwieg tube was designed to use interchangeable nozzles, but only the Mach 6 nozzle was used throughout the experiment. The nozzle terminates in the test chamber which is approximately 50 inches in diameter and constructed of carbon steel. The test chamber contains three circular hatches, one on top and one each side of the test chamber. Two 25 HP vacuum pumps reduce the pressure inside the test section to less than 0.01 psia. The test section contains a mobile sting which provides adjustable angle of attacks and distance from the nozzle [18].

The diffuser is located downstream of the test section and contains a 6° converging cone, a straight pipe, and a 4° diverging cone. The diffuser leads into two 2000 gallon vacuum tanks. The first tank immediately downstream of the diffuser contains an internal doubler to absorb any debris impacts without damaging the wall of the tank [18].

A recent upgrade to the Ludwieg tube was the installation of air dryers at the intake of the compressor. One of the key concerns during previous tests was the formation of frost on heavily cooled surfaces. Moisture in the air could freeze to the surface of the cone as it flows from the high pressure chamber to the test section. This would create a layer of frost on the test article, which would increases surface roughness and exacerbates the transition of laminar to turbulent flow. The air dryers reduce the water vapor concentrations from 50,000 parts per million (ppm) to <20 ppm, allowing for multiple tests to be performed throughout the day [11].

The Ludwieg tube is operated from a control room connected to the tunnel via an Ethernet connection. Both the vacuum and compressors can be remotely operated from the control room using this system. The tunnel is also charged, discharged, and

fired using the same system. Wind tunnel pressure transducers are placed within the tunnel to measure the stagnation pressure throughout a run. The stagnation pressure throughout a nominal 500 psi run can be seen in Figure 15. The two quasi-steady periods of relatively constant pressure can be clearly seen. The video capture for the experiments conducted herein spanned the entire run, however, most of the preserved files consisted of only the two quasi-steady periods. The stagnation pressure is measured within the the section, and is governed by the conditions behind the expansion wave. The stagnation pressure in the test section is approximately 90% that of the driver tube, and reduces by an additional 20% after the wave reflection [27].

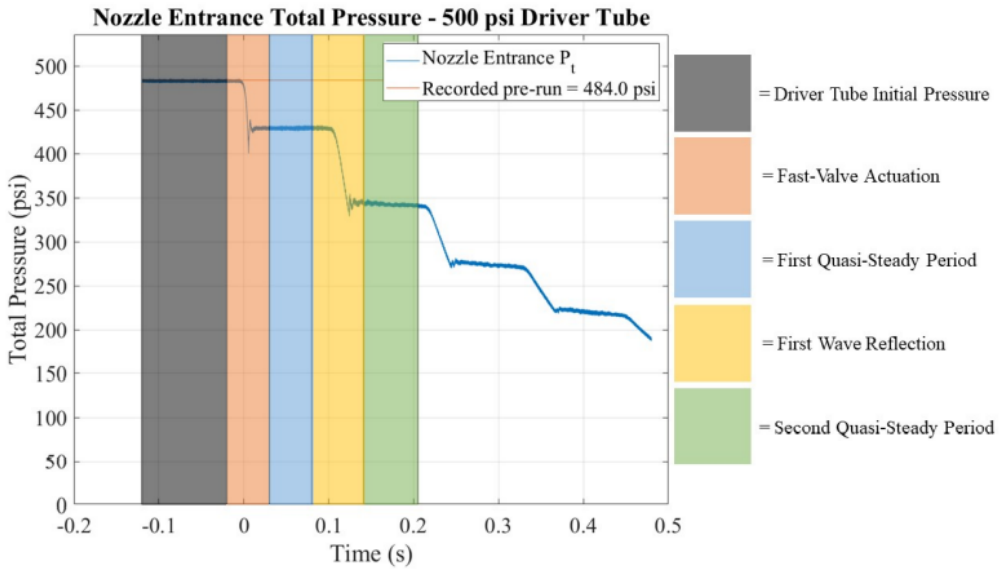

Figure 15. Stagnation pressure trace during nominal 500 psi run

3.2 Flow Conditions

Previous experiments by LaBuda and other have quantified the performance of the wind tunnel. LaBuda observed that the 200 ms quasi-steady flow is equally split between two periods of 100 ms each [20]. The properties of these states behave as a

shock tube. The freestream Reynolds number decreases due to the stagnation pressure drop after each expansion wave reflection. The periods between these reflections have relatively stable properties which allows for approximation of the Reynolds number.

The Reynolds number can be calculated through Equations 1 - 7. The freestream Mach number used for these calculations is 6.1, with a driver tube temperature of 505 K. The stagnation pressure is assumed to be at 90% and 70% for the first and second quasi-steady state respectively. Isentropic expansion and a calorically perfect gas ($\gamma = 1.4$) are also assumed throughout the flow.

The test chamber stagnation temperature is calculated by

$$T_0 = T_{DT} \left(\frac{P_0}{P_{DT}} \right)^{\frac{\gamma-1}{\gamma}} \tag{1}$$

where T_0 and P_0 are stagnation temperature and pressure and T_{DT} and P_{DT} are driver tube stagnation temperature and pressure. The stagnation density can then be calculated via the equation of state

$$\rho_0 = \frac{P_0}{R \cdot T_0} \tag{2}$$

where ρ_0 is the stagnation density and R is the specific gas constant. R = 287.06 $\frac{J}{kg \cdot K}$ for these calculations. Next, the freestream temperature is calculated by

$$T_\infty = T_0 \left(1 + \frac{\gamma - 1}{2} M_\infty^2 \right)^{-1} \tag{3}$$

where T_∞ is the freestream temperature and M_∞ is the freestream Mach number. The freestream density is calculated by

$$\rho_\infty = \rho_0 \left(1 + \frac{\gamma - 1}{2} M_\infty^2 \right)^{\frac{-1}{\gamma-1}} \tag{4}$$

where ρ_∞ is the freestream density. Freestream viscosity is calculated by

$$\mu_\infty \cdot 10^5 = 1.458 \cdot \frac{T_\infty^{3/2}}{T_\infty + 110.4} \tag{5}$$

The unit Reynolds number can be calculated with these variables by

$$Re_\infty/L = \frac{U_\infty \cdot \rho_\infty}{\mu_\infty} \tag{6}$$

Results of these equations were tabulated across driver tube pressures by Embrador [11] and can be seen in Figure 16.

P_{DT} (psia [MPa])	QS Period	P_0 (psia [MPa])	T_0 (K)	U_∞ (m/s)	T_∞ (K)	μ_∞ (kg/m*s)	Re_∞/L (1/m)
50 [0.34]	1	45 [0.31]	490.0	931.7	58.05	3.83×10^{-6}	2.59×10^6
50 [0.34]	2	35 [0.24]	456.1	898.8	54.02	3.52×10^{-6}	2.27×10^6
100 [0.69]	1	90 [0.62]	490.0	931.7	58.05	3.83×10^{-6}	5.19×10^6
100 [0.69]	2	70 [0.48]	456.1	898.8	54.02	3.52×10^{-6}	4.54×10^6
150 [1.03]	1	135 [0.93]	490.0	931.7	58.05	3.83×10^{-6}	7.78×10^6
150 [1.03]	2	105 [0.72]	456.1	898.8	54.02	3.52×10^{-6}	6.82×10^6
200 [1.38]	1	180 [1.24]	490.0	931.7	58.05	3.83×10^{-6}	10.4×10^6
200 [1.38]	2	140 [0.97]	456.1	898.8	54.02	3.52×10^{-6}	9.09×10^6
300 [2.07]	1	270 [1.86]	490.0	931.7	58.05	3.83×10^{-6}	15.6×10^6
300 [2.07]	2	210 [1.45]	456.1	898.8	54.02	3.52×10^{-6}	13.6×10^6
400 [2.76]	1	360 [2.48]	490.0	931.7	58.05	3.83×10^{-6}	20.7×10^6
400 [2.76]	2	280 [1.93]	456.1	898.8	54.02	3.52×10^{-6}	18.2×10^6
500 [3.45]	1	450 [3.10]	490.0	931.7	58.05	3.83×10^{-6}	25.9×10^6
500 [3.45]	2	350 [2.41]	456.1	898.8	54.02	3.52×10^{-6}	22.7×10^6

Figure 16. Nominal flow conditions for Mach 6.1 flow in AFRL Ludwieg Tube [11]

3.3 Test Article

The tunnel test article was composed of two principal parts, the dry ice model and the stainless steel holder. The choice of dry ice as the model material was made after reviewing the relevant literature and its availability compared to other low-temperature sublimators. Any solid material released into the wind tunnel would

eventually sublimate, which removed the requirement to clean it out from the vacuum chamber.

3.3.1 Fabrication of Dry Ice Model

The fabrication method developed for this research was based on the lessons learned from previous research, particularly Callaway's [5]. Callaway initially attempted to use a commercially available dry ice maker, the Frigimat Cub Dry-ice Maker, to produce workable models. The Cub was designed to connect to a carbon dioxide tank with a liquid tap, which would form a brick of dry ice within the reservoir. It was operated at less than psig with a pressure relief valve and a pressure gauge for safety. This, however, was not usable because the dry ice produced had the consistency of snow and was not dense enough for model usage.

Callaway next developed a method of pumping liquid carbon dioxide in resin molds of a predetermined shape. Callaway still encountered difficulties with producing models of sufficiently high density that would survive being removed from the mold and wind tunnel operation. Callaway was eventually able to generate a process that could successfully create an model appropriate for wind-tunnel testing roughly one-third of the time. Furthermore, only about one-third of the models that survived the manufacturing process were able to yield usable wind tunnel results, mostly due to failure during wind tunnel operation.

With this in mind, solid dry ice blocks were purchased from a local supplier to cut out a step in the manufacturing process that had a high failure rate. The models in this experiment were also significantly larger. The commercially procured dry ice had a density of approximately 1.4 g/cm^3, which was 40% higher than the measured value for the dry ice produced in Callaway's experiments. This is likely a factor that contributed to the higher success rate within the Ludwieg Tube, despite the

significantly higher stagnation pressures and longer waiting periods prior to the run. The dry ice was stored in a cooler when not in use.

The commercially produced dry ice was formed into blocks that measured 10" x 10" x $2\frac{3}{8}$". It was quickly found that the dry ice was easily cut with a band saw. The band saw was then used to cut the dry ice blocks into cuboids that approximately measured 8" x 2" x 2". After initial testing it was determined that pre-shaping the top of the cuboids into an obelisk would allow the faster formation of the dry ice cones. After this, all the ice blocks were formed into obelisks that were approximately 6" x 2" x 2" that was topped by a four-sided pyramid that was 2" tall. The procedure for storing commercial blocks in coolers overnight meant that one hundred pounds of dry ice could be reliably used for two days of testing.

An aluminum mold was produced by the AFIT machine shop to form the dry ice into cones. The mold had a base diameter of 3 inches, and an axial length of 4 inches, and included a hole through the tip to allow outgassing. A rendering of the mold can be seen in Figure 17. The mold ideally formed 21° half-angle cones with a nominally sharp leading edge, assuming the dry ice model conformed precisely to the aluminum mold.

The different temperatures between the room temperature aluminum mold and the surface of the dry ice block caused sublimation. As the dry ice sublimated, it could be gradually pressed further into the mold until a complete cone was formed. Initial attempts to form the mold were performed in the Ludwieg Tube, with the dry ice cuboid already pinned into the holder. The machine shop created a plastic piece that fits over the stainless steel holder that would help guide the mold in a straight line. The plastic guide can be seen on the left side of Figure 18, and the final aluminum mold can be seen on the right. This method worked proved to be impractical in the tunnel. It took approximately 10 - 15 minutes to fully form a

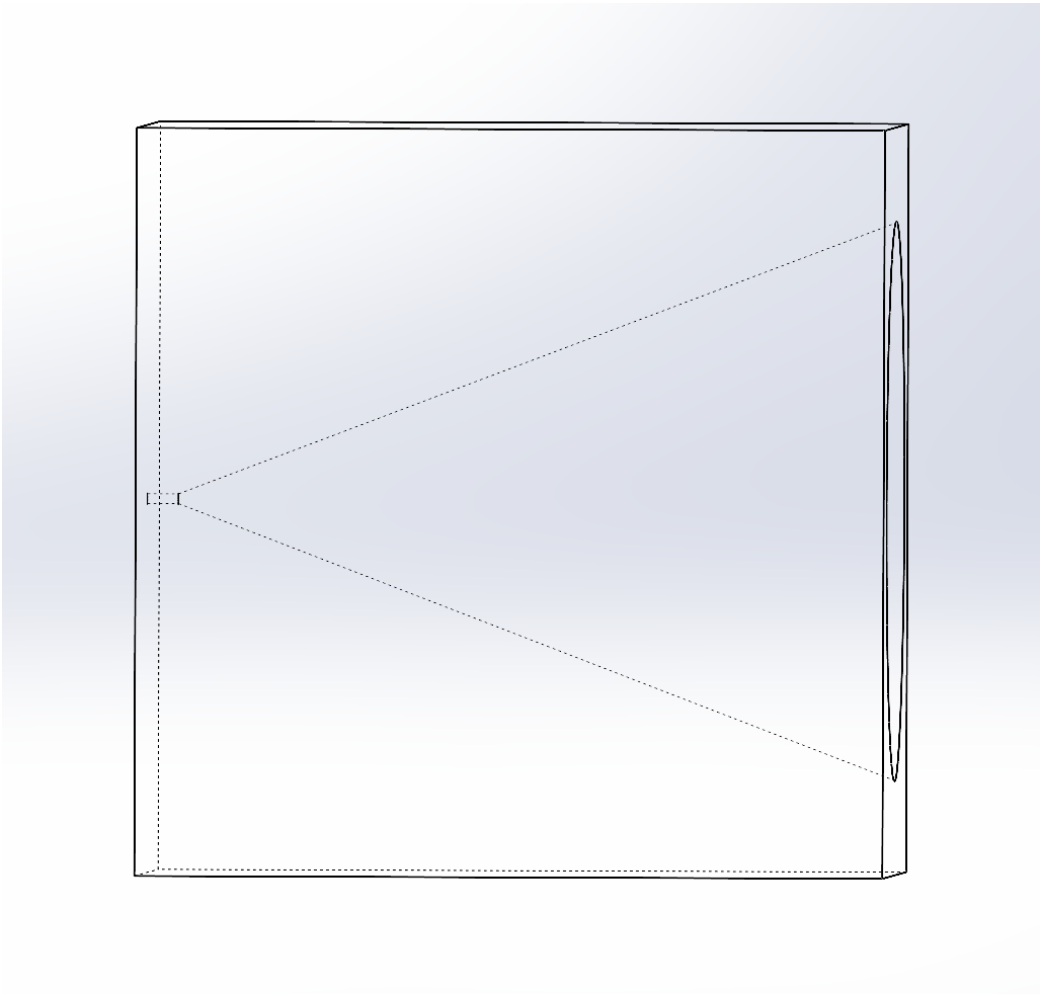

Figure 17. Rendering of Aluminum Cone Mold

dry ice cone with a sharp leading edge. Additionally, the plastic guide would slide down the holder, so one hand was needed to hold the guide in place, and another was needed to firmly press the mold onto the holder. Furthermore, the bubbling of the surface of the dry ice combined with a constant force pressing the mold onto the dry ice caused vibrations. These vibrations could be quite intense depending on how much force was applied. These vibrations caused a loud, jackhammer-like noise which was amplified within the Ludwieg Tube. These factors made forming the cone while it was within the holder impractical, and the cones were instead formed in the lab area and placed within the holder after they were formed.

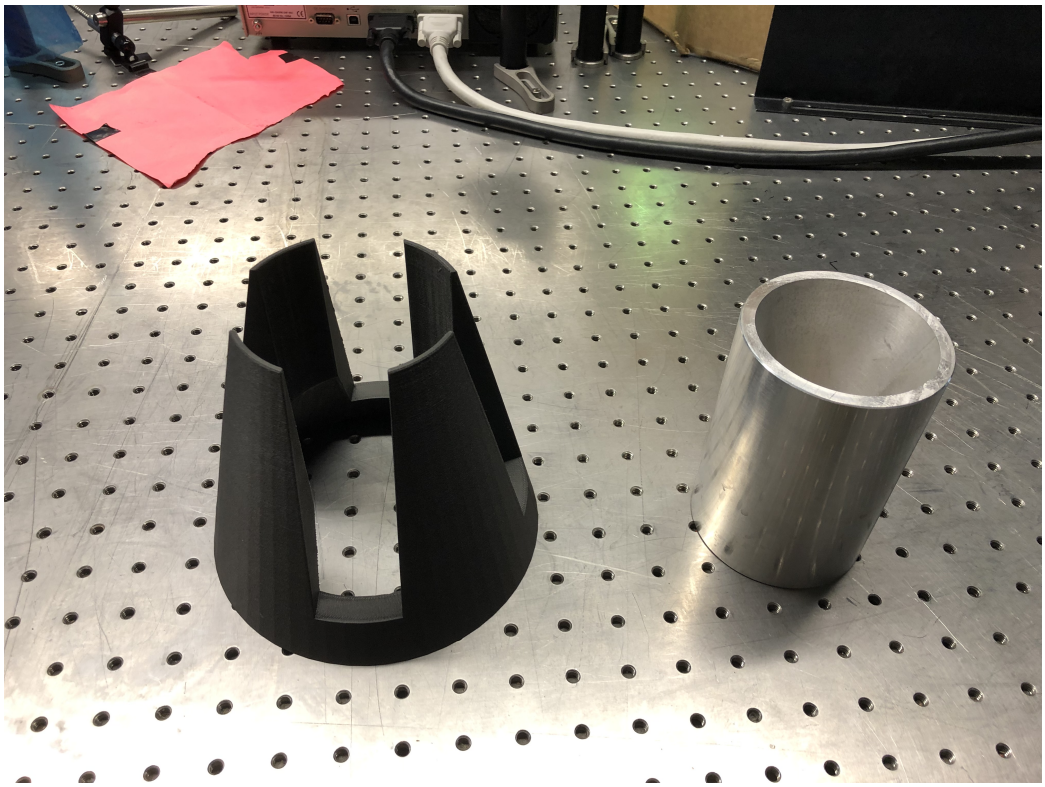

Figure 18. Plastic Guide (L) and Aluminum Mold (R)

When the molds were too warm, sublimation occurred so rapidly that the mold would vibrate and make considerable noise. Overcoming the strong vibrations proved to be one of the major obstacles of the model manufacturing process. Longitudinal

hairline cracks would form around the square portion of the ice models the vibrations were either too strong or lasted too long. These cracks would usually form around a few inches from the leading edge of the cone. These cracks proved to be destructive to most of the dry ice models when vibration occurred. The models would either fail at the crack during manufacture or would fail during tunnel operation. An image of these cracks can be seen in Figure 19. Once a crack had formed, a model would generally fail under a small amount of side force, which often occurred while placing the ice model into the holder. Figure 20 depicts the same model as Figure 19 shortly after the first photo was taken. It can be seen that the model caused a clean break along the hairline crack. Cracked models used within the Ludwieg Tube would typically fail within the first quasi-steady period, resulting in little or no usable data.

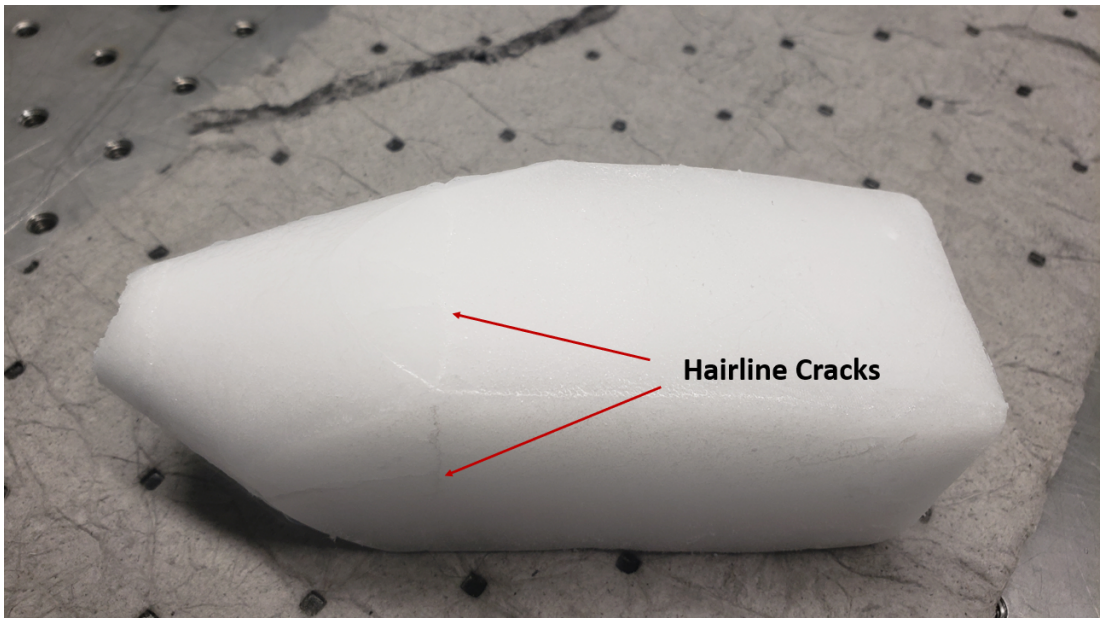

Figure 19. Ice Model with Hairline Cracks

This problem was mitigated by cooling the aluminum mold to reduce its temperature. The lower sublimation rate eliminated vibrations and produced models without cracks. Spare pieces of dry ice were placed into the molds to rapidly cool them down. The dry ice blocks were then forced into the mold once it had been cooled to the

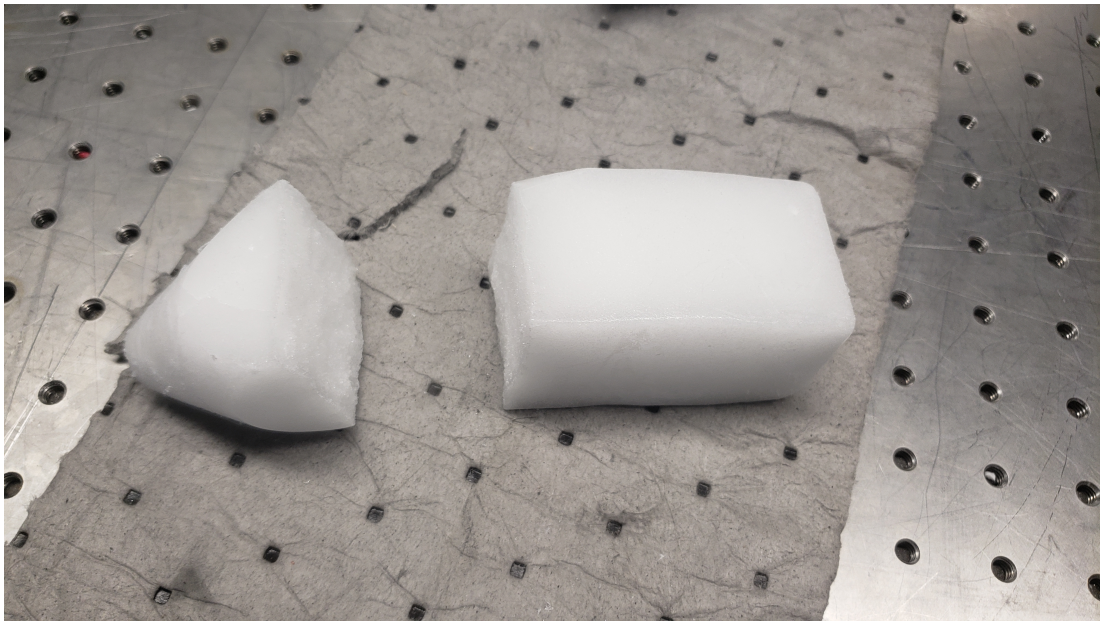

Figure 20. Failed Model

point that only minimal vibrations were observed. The mold and dry ice block would eventually reach a near-equilibrium state, usually over about a 15-minute period, wherein the mold was so cold that the sublimation rate was slowed. Frost would also begin to form on the mold as it became so cool that it froze the moisture within the laboratory air, but this did not affect model quality. A heat gun was then used to gently bring the mold back up to a temperature at which sublimation could progress at a reasonable rate. The best means of heating the mold was to lay a heat gun on its lowest setting to the side and slowly rotate the mold to ensure even heating. The dry ice model could also be briefly lifted out of the mold so that the heat gun could be used to directly heat the area of the mold near the tip. The heating process can be seen in Figure 21. The melting frost occasionally impacted the dry ice models, and care had to be taken to minimize the moisture on the mold. With practice, this process yielded a successful model over 90% of the time. Although using a cooled mold extended the time it took to form a cone, a completed model could be fabricated in around 15 minutes. Given that the Ludwieg Tube needed around 15 minutes to

charge between runs, near-continuous testing could be accomplished once the process had been adequately practiced, though occasionally a model cracked, which extended the time between runs. Additionally, once the dry ice model had sunk far enough into the mold gravity alone was enough to force it in, meaning other tasks could be accomplished while the model was passively molded. A completed dry ice model can be seen in Figure 22, and a close-up view of the sharpness attainable with dry ice molds can be seen in Figure 23.

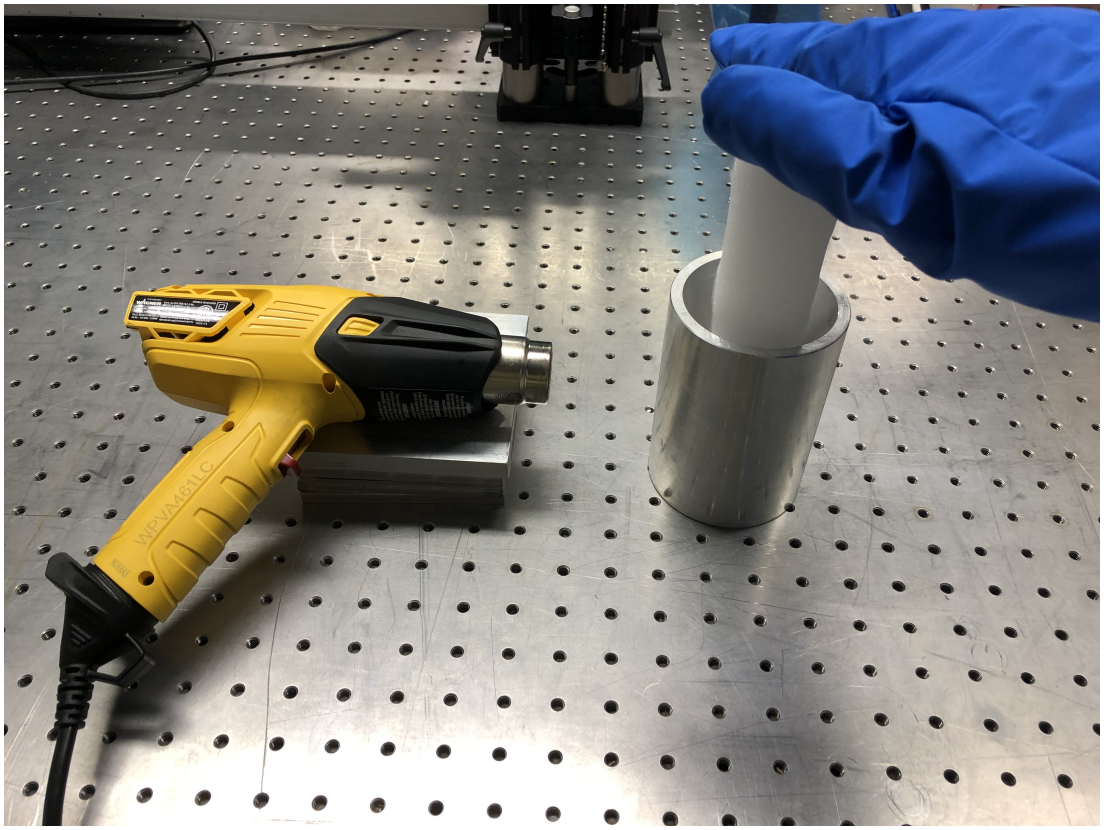

Figure 21. Heating the Aluminum Mold

A second bi-conic mold was machined to create a sharper leading edge compared to the simple cone. This mold was fabricated after observing several runs of the simple cone model. Initial tests revealed that the simple cone model appeared to ablate slowly relative to the tunnel test time, and it was thought that an increaed ablation rate might improve the fidelity of the data. A second consideration was that it would

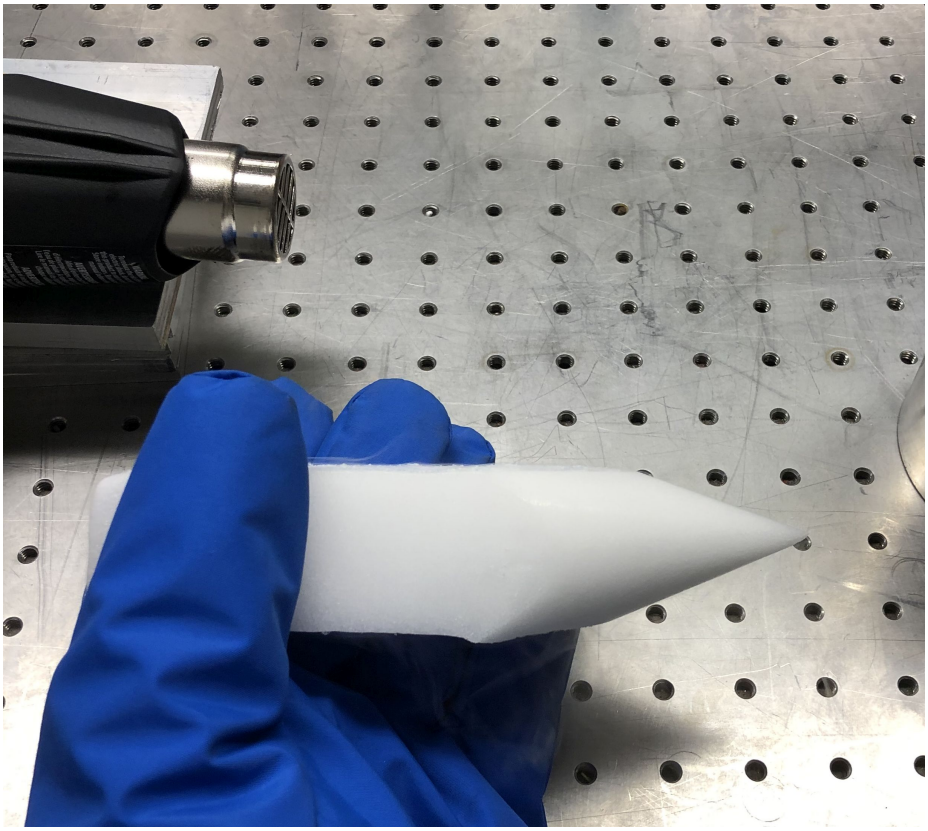

Figure 22. Dry Ice Cone

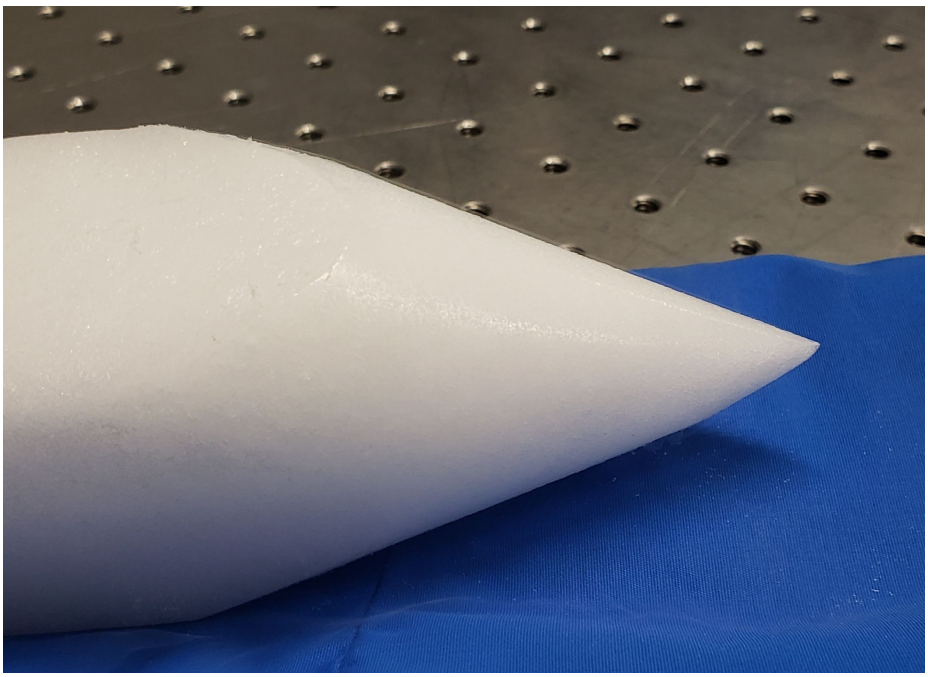

Figure 23. Dry Ice Cone Leading Edge

be appropriate to explore the possibility of both generating more complex shapes and generating a re-circulation region where ablation might be more pronounced. The bi-conic mold consisted of a 7° half-angle leading edge that was 3 inches in axial length, followed by a 26° half-angle base. An engineering drawing of the design can be seen in Figure 24. Forming dry ice models with this mold proved to be more difficult compared to the simple cone mold.

One of the main challenges of forming the bi-conic models is it essentially required the sequential formation of two separate cones on a single dry ice block. Forming a single bi-conic model took about 30 minutes, or roughly double the simple cone models. To expedite the fabrication process, an ice block could be formed into a rough cone using the first mold, and could then be transferred to the bi-conic mold for completion. This enabled two dry ice models to be built simultaneously.

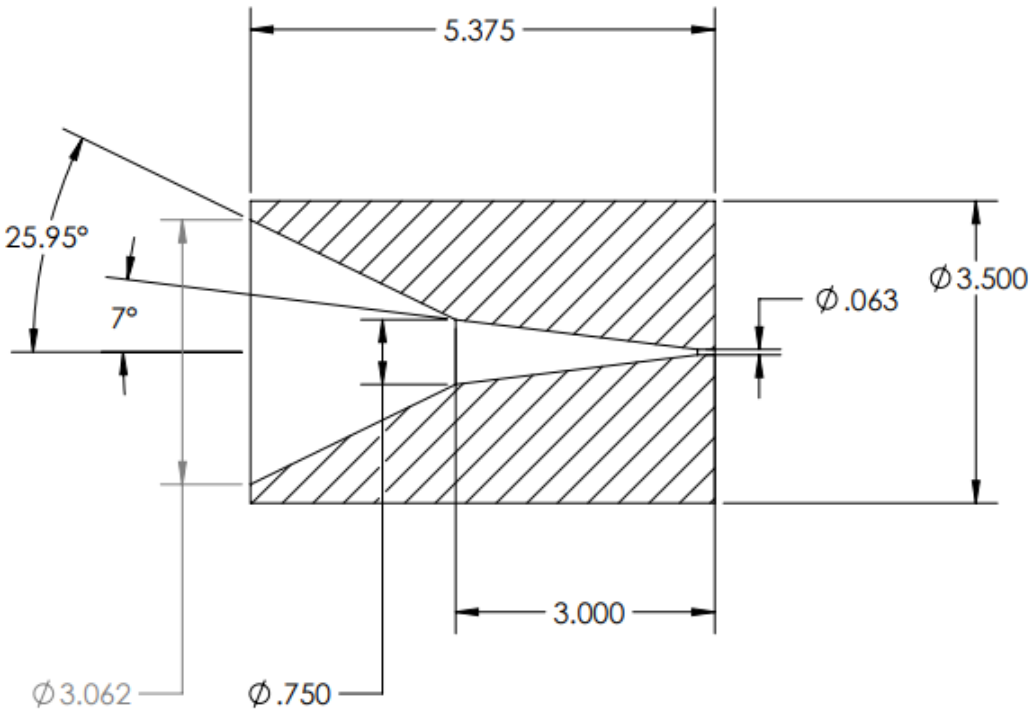

Figure 24. Engineering Drawing of Bi-conic Mold

In addition to taking more time, the bi-conic model also suffered a higher failure rate during production. This increased failure rate was expected. Cracks formed around the base of the narrow nose, which was prone to failure because of vibrations within the mold. When the nose of the simple model broke it, was relatively easy to resharpen in a matter of minutes, but when the nose of the bi-conic model failed it required a new ice block. Overall, fewer than half of the attempted bi-conic models survived the fabrication process, although less time was spent creating these models compared to the simple cone model. Like the simple cone model, some practice with the fabrication technique improved the likelihood of survival.

3.3.2 Dry Ice Holder

The dry ice models were the highest mass "free fliers" used within the Ludwieg Tube by several orders of magnitude. Careful consideration was made to create a design that could safely secure the dry ice models without altering flow characteristics. The holder required active cooling to prevent model sublimation during tunnel evacuation. The holder was secured to the sting utilizing a mount portion that had already been tested and proven. 303 stainless steel was used for all portions of the model because of its strength at cryogenic temperatures. The holder was also built with as few parts as possible to lower the risk to the tunnel.

The employed design was composed of three pieces machined from 303 stainless steel, including the mounting base, an LN2 cavity, and the dry ice holder. The mounting piece that connects the holder to the sting is the same design that was used in previous research by Oddo [27], Embrador [11], and others. The base piece contains three 1/4 inch threaded NPT holes, two for LN2 transfer and one for a cryogenic relief valve (CRV). The base attaches to the cone section using eight 18-8 5/16 inch extreme strength steel screws with a compressed high-pressure cryogenic

O-ring to ensure a leak-free seal. The second piece forms a hollow cavity for the LN2. The top of the holder is based on a 37° half-angle cone with a 2" x 2" x 4" box sunk through the tip. The holder is connected to the mid-piece by eight .25-20 x 1.5-inch socket head cap screws. The dry ice is secured in the box by four .25-20 button head cap screws. Views from various angles of the holder can be seen in Figures, 72a, 72b, and 72c. An engineering drawing can be seen in Figure 26. The disassembled pieces can be seen in Figure 27, and the fully constructed holder can be seen in Figure 28.

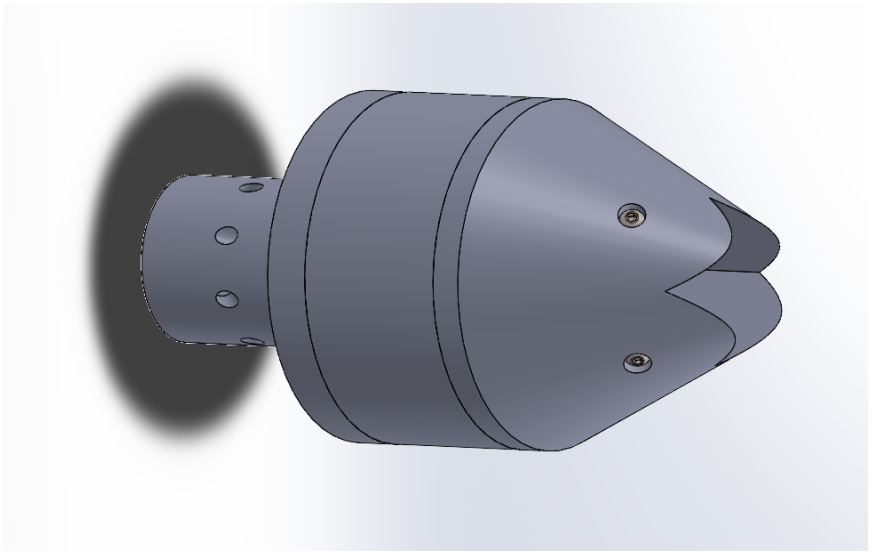

(a) Dry Ice Holder, Isometric view

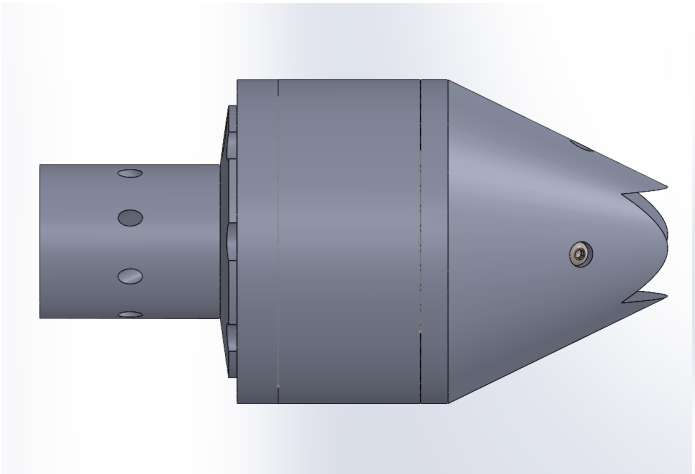

(b) Dry Ice Holder, Side view

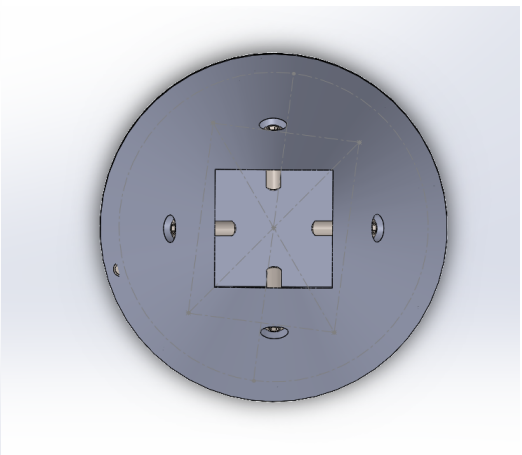

(c) Dry Ice Holder, Front view

Figure 25. Dry Ice Holder

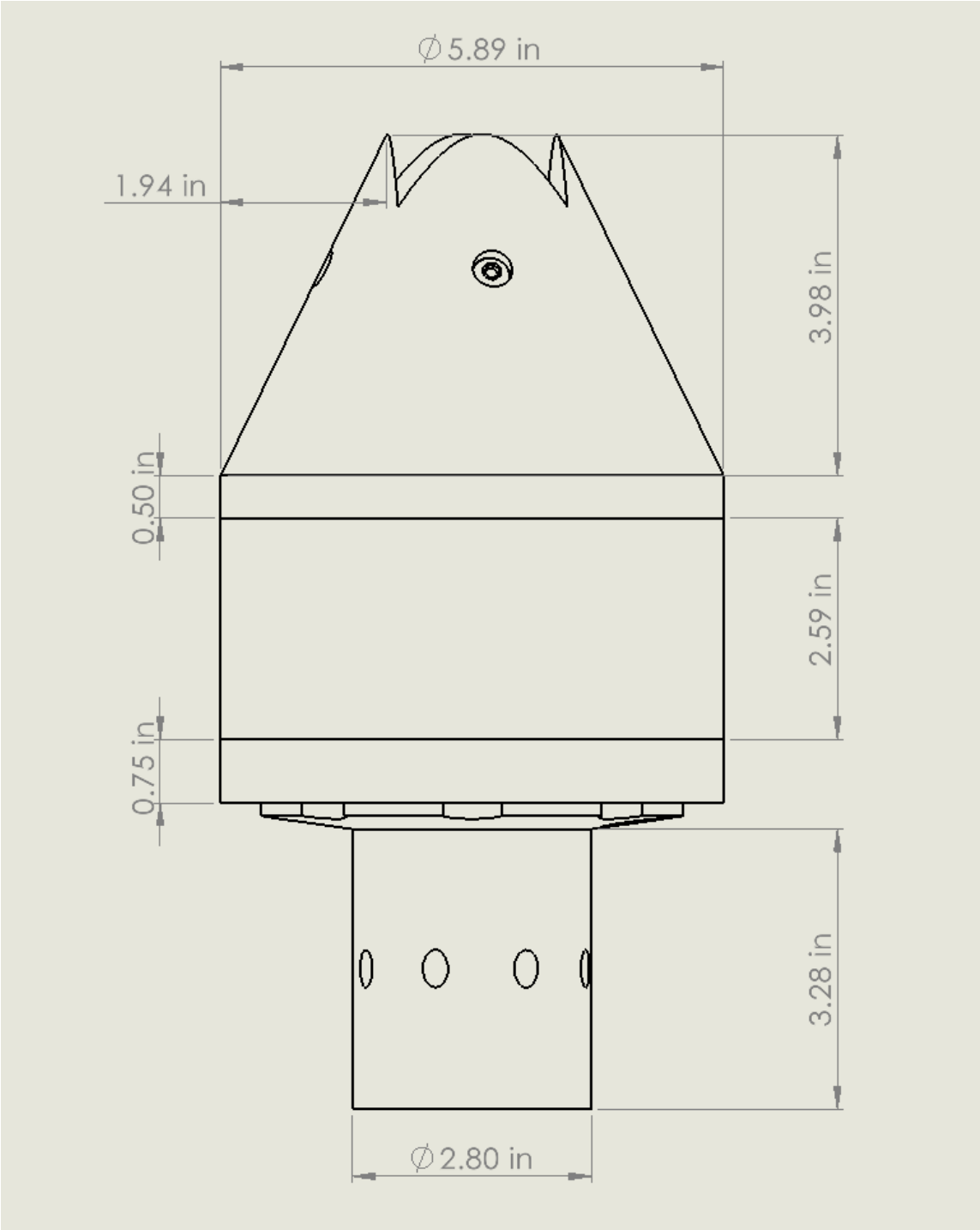

Figure 26. Engineering Drawing of Dry Ice Holder

Figure 27. Base (L), Cryogenic Cavity (C), Dry Ice Holder (R)

Figure 28. Fully Constructed Dry Ice Holder

When the dry ice cone had finished construction it was carefully slid into the compartment at the front of the holder. Care was taken to avoid damaging the tip, but the dry ice block could sustain some pressure if it needed to be pressed into place. During the initial tests, four 0.25-20 inch screws were used to secure the dry ice block inside the holder. The screws could penetrate the dry ice block and would cause some sublimation in the immediate region, but otherwise caused no damage. The small gap between the screws and the dry ice block did give the block a few millimeters of movement. After some experimentation, it was determined that two screws at 90° separation could provide sufficient clamping force to keep the ice in place. The base of the dry ice cone remained within the holder throughout the duration of every run.

A spring mechanism that could apply a constant force to the dry ice was considered, but was opted against to rule out the possibility of the spring coming loose or breaking. The spring mechanism would have pinned the dry ice against the holder and prevent movements during tunnel operation. This was determined to be an acceptable trade-off for initial testing, though an improved design for holding the block would be helpful for future testing.

3.4 Cooling System and Cryogenic Design

A cryogenic cooling system utilized in prior work cooled the dry ice holder, which reduced the amount of sublimation that occurred on the dry ice cone while the tunnel was brought to the desired test conditions. Only small adaptations were applied to the system used in previous research by Oddo [27], Embrador [11], and others.

The cooling system is comprised of a storage tank, both insulated and un-insulated hoses, and a system of connectors made specifically for low-temperature applications. The inflow for cryogenic fluid originates from a 160L cryogenic container, shown in Figure 29a, filled with LN2 at a pressure of 15 psi. When opened, the LN2 flows

through a series of insulated hoses into a specialty-made connector, shown in Figure 29b.

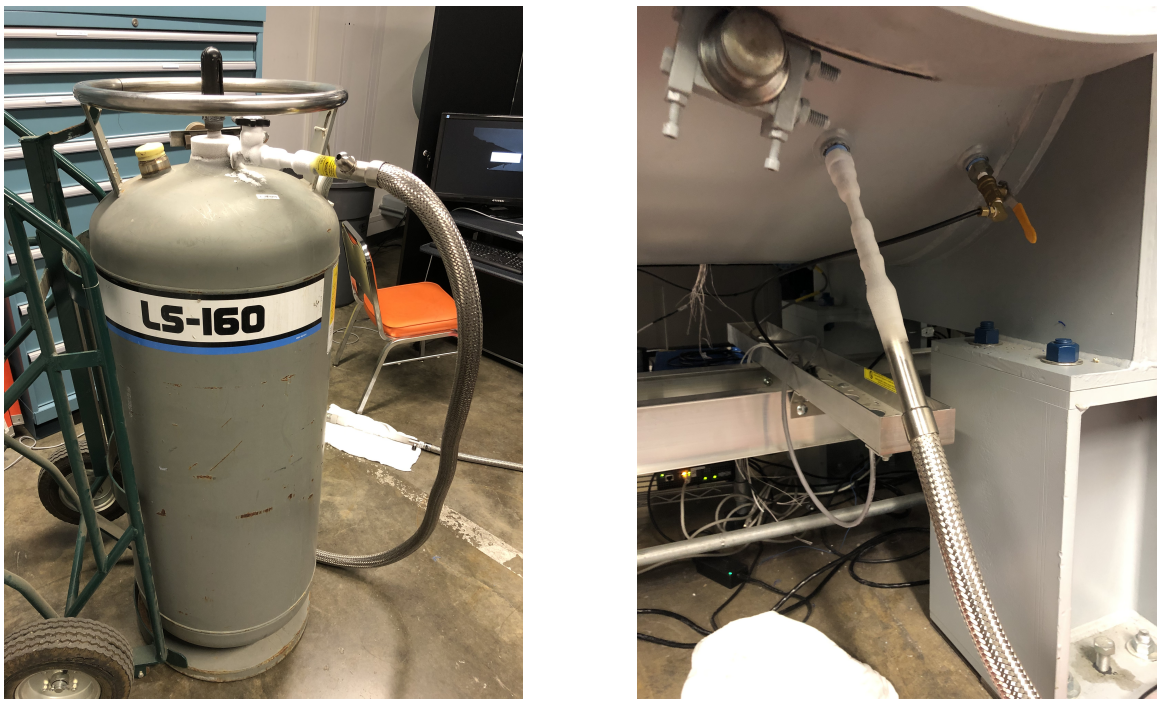

(a) 160L Cryogenic Container **(b) Tunnel Entrance Connection**

Figure 29. Cryogenic Cooling System

An insulated line brings the in-flowing LN2 into the holder cavity to cool the surface of the holder. After circulating inside the cone, the LN2 flows out through another insulated line to a second cryogenic-specific connector. The LN2 then flows through a 75-foot un-insulated hose through an exhaust port leading to the outside of the lab. A schematic of the cooling system is shown in Figure 30. The cryogenic lines were secured to the sting mount using a stainless steel structure with multiple hose brackets clamped to the mount. The insulated cryogenic lines were further secured using plastic-lined pressure clamps to reduce vibration and movement. The hoses were attached using an aluminum support bracket at the walls of the test section. This setup allowed runs with stagnation pressures over 500 psi to be accomplished [11].

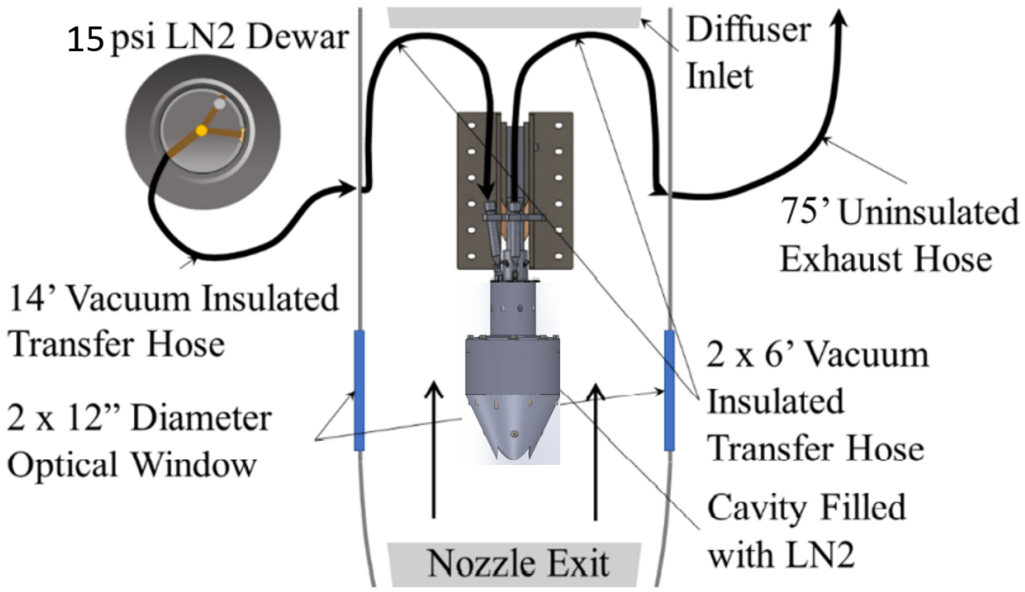

Figure 30. Schematic of Cryogenic Setup [27]

3.4.1 Cooling Process

If the surface temperature of the dry ice holder is above the sublimation temperature then the dry ice will continually sublimate throughout the time it takes to bring the Ludwieg Tube driver and test sections to their desired conditions. The dry ice can even vibrate and sink into the holder as it continued to sublimate if the holder temperature is excessive. As the dry ice block sublimated, a gap would form between the upper wall and the block. This gap allowed stagnation air into the holder which led to the dry ice moving forward into the freestream. To counteract this, the dry ice holder was cooled to minimize the shape change during tunnel charging. The LN2 was not allowed to flow while the tunnel door was open due to safety concerns. Cloth material was wrapped around the holder to insulate it and minimize the warming of the surface between runs. Once the dry ice cone had been paced within the holder, the tunnel door was closed and the LN2 valve was opened. The valve was then shut before tunnel operation to prevent an LN2 leak if the lines were damaged.

Contrary to previous experiments using a cooled test setup, the dry ice holder spent a significant amount of time at atmospheric conditions while cooled. This was possible because frost on the holder did not affect measurements upstream at the model nose. A cooling test was performed to identify the schedule and total time required to reach an equilibrium surface temperature condition for the model. Two silicon diodes were attached to the holder with PTFE thread tape to monitor the surface temperature; one at the base of the holder and one on the lower lip, where most of the sublimation was observed. The Ludwieg Tube was left at atmospheric conditions and allowed to cool for two hours. The results of the cooling test can be seen in Figure 31. The dry ice holder reached 150K after two hours of cooling, which was still above the triple point of carbon dioxide at low pressures. Previous work by Oddo showed that LN2 cooling was significantly more effective at vacuum conditions [27]. Oddo's testing showed that an equilibrium temperature of around 100K could be reached within 90 minutes of cooling at vacuum, despite having a larger surface area to cool. This test was not repeated at vacuum, but experimental results showed that 90 minutes of cooling for the dry ice holder was sufficiently long to prevent notable sublimation during the tunnel charging process.

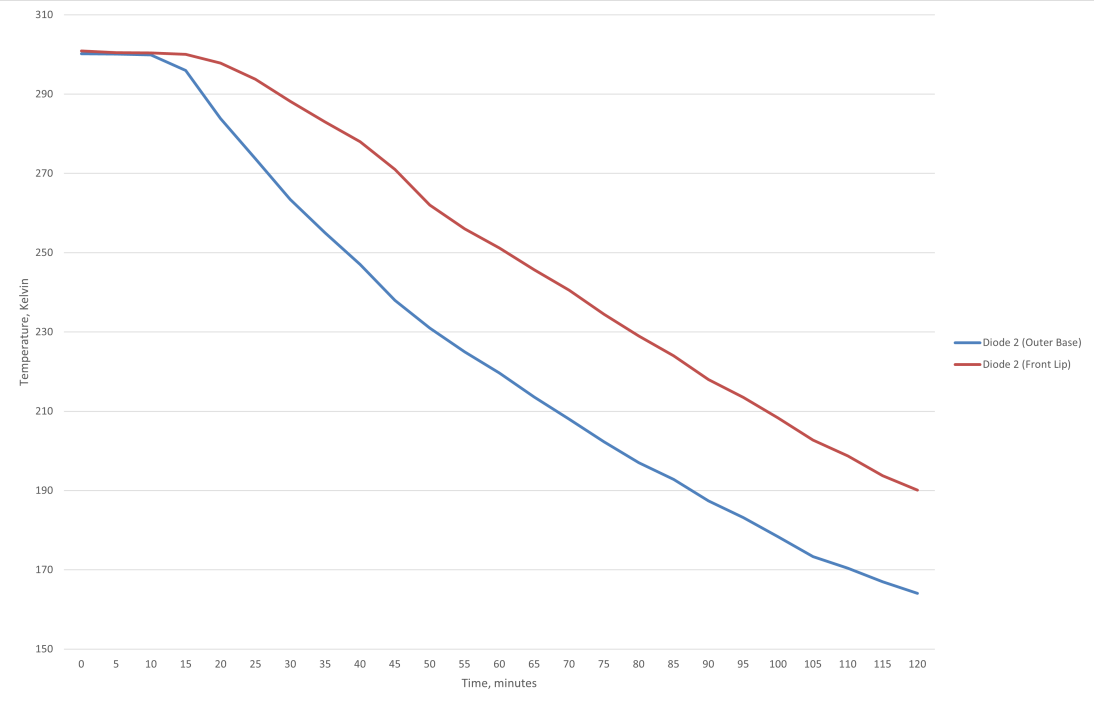

Figure 31. Cooling Test

3.5 High-Speed Schlieren

Schlieren visualization was used for capturing data for all experiments. The schlieren technique takes advantage of the refraction of light beams as they pass through mediums of varying refractive indices. Some light is reflected or refracted as it passes through areas of in-homogeneity in the flow caused by density gradients. The remaining light beams are then refocused using a parabolic mirror or lens shone over a razor's edge into a camera. This produces highly contrasted images which can capture characteristics of the flow.

A mirror-based schlieren visualization and high-speed camera were used to visually capture the flow. The setup schematic differed from that used by Oddo [27] and Embrador [11], but utilized the same equipment. A Newport 66921 Arc Lamp was powered by an OPS-A100 Arc Lamp supply. The lamp was powered at an output of 600 W. A schematic of the setup is shown in Figure 32 and described in Table 1.

Table 1. Schlieren Setup

Component	Description
A	Oriel OPS-A1000 Arc Lamp Supply
B	Newport 66921 Arc Lamp, 1000 W
C	BK7 A Coated Plano-Convex Lens, 2.0" Diameter, F = 150.0 mm
D	Circular Aperture, 2.5" Diameter
E	Concave Mirror, 12" Diameter, Parabolic, F = 75"
F	Concave Mirror, 12" Diameter, Parabolic, F = 75"
G	Planar Mirror, 8.0" Diameter
H	Planar Mirror, 3.0" Diameter
I	Razor Blade and holder
J	Camera Lens, Nikon Nikkor 80-200mm 1:2.8D
K	2k Zoom Teleconverter, Nikon
L	Photron Fastcam SA-Z-2100K-M

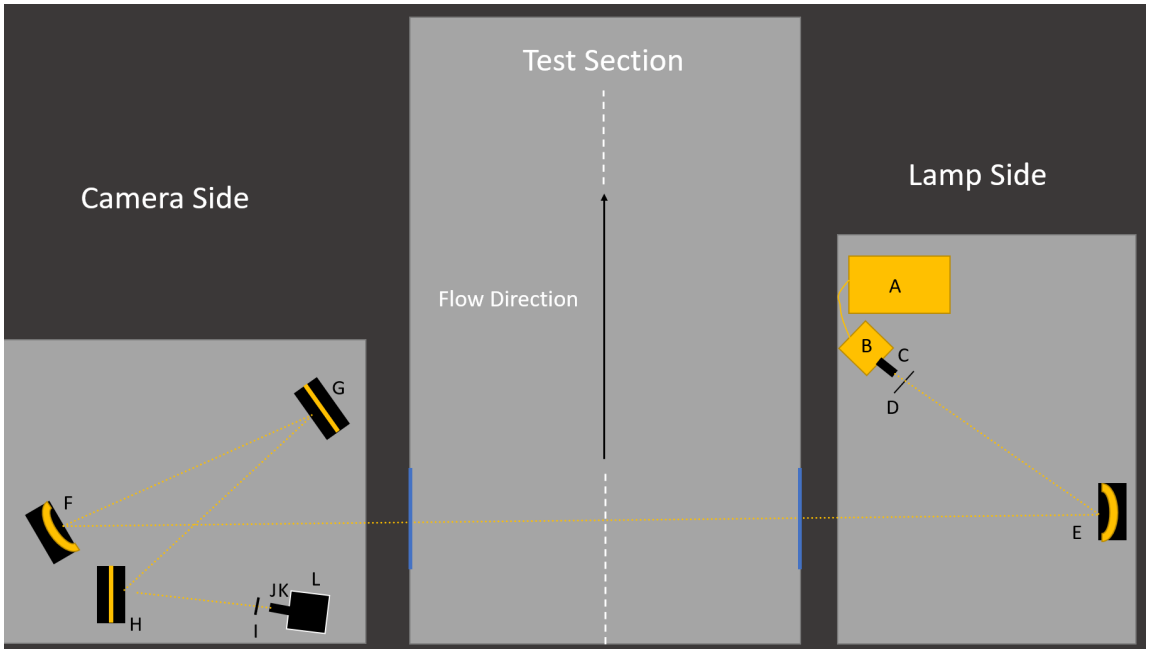

Figure 32. Schlieren Schematic

The originating light was focused through a Plano-convex (PCX) lens onto a circular aperture allowing only a small diameter of light to pass through. From this, the light was reflected through the first concave mirror through the test section onto the second concave mirror. Two planar mirrors were then used to project the light

back towards the camera. A horizontal knife-edge was used to block half of the light at the horizontal focal point. The camera used was a Photron Fastcam SA-Z-2100K with a max capture of over two million frames per second (FPS) and a minimum exposure time of 159 nanoseconds. Pictures of the schlieren setup can be seen in Figure 33a and Figure 33b.

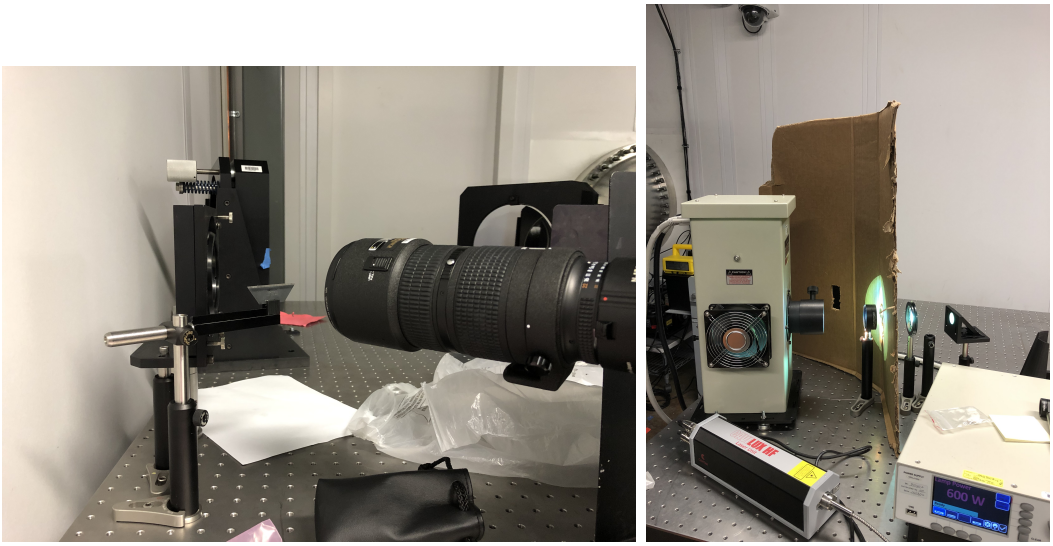

(a) Schlieren Setup - Camera Side **(b) Schlieren Setup - Lamp Side**

Figure 33. Schlieren Setup

The Photron camera software was used to check the light quality and uniformity throughout the viewing window. Light quality could be measured across the window using the probe tool. Fine adjustments to the lamp or knife-edge could be made to ensure better image quality. The camera was also calibrated to trigger with the tunnel actuator, ensuring that the full run was captured. The video could then be reviewed so that unnecessary frames could be eliminated. A balance between shutter speed and camera frame rate was required. Increases in shutter speed allowed sharper images to be captured at the cost of darker images with less light. Due to the relatively slow propagation of dry ice pieces throughout the flow compared to wave propagation speed, the minimum shutter speed of 249 nanoseconds was used with a frame rate of 20,000 FPS.

The viewing window comprised the tip of the dry ice holder just in front of the dry ice cone. For length and height calibration, a single image was taken to determine the dimension of the schlieren images. A screw and nut measured with calipers were placed on the test article and an image was taken to provide the length to pixel conversion. An example of the calibration photo is shown in Figure 34.

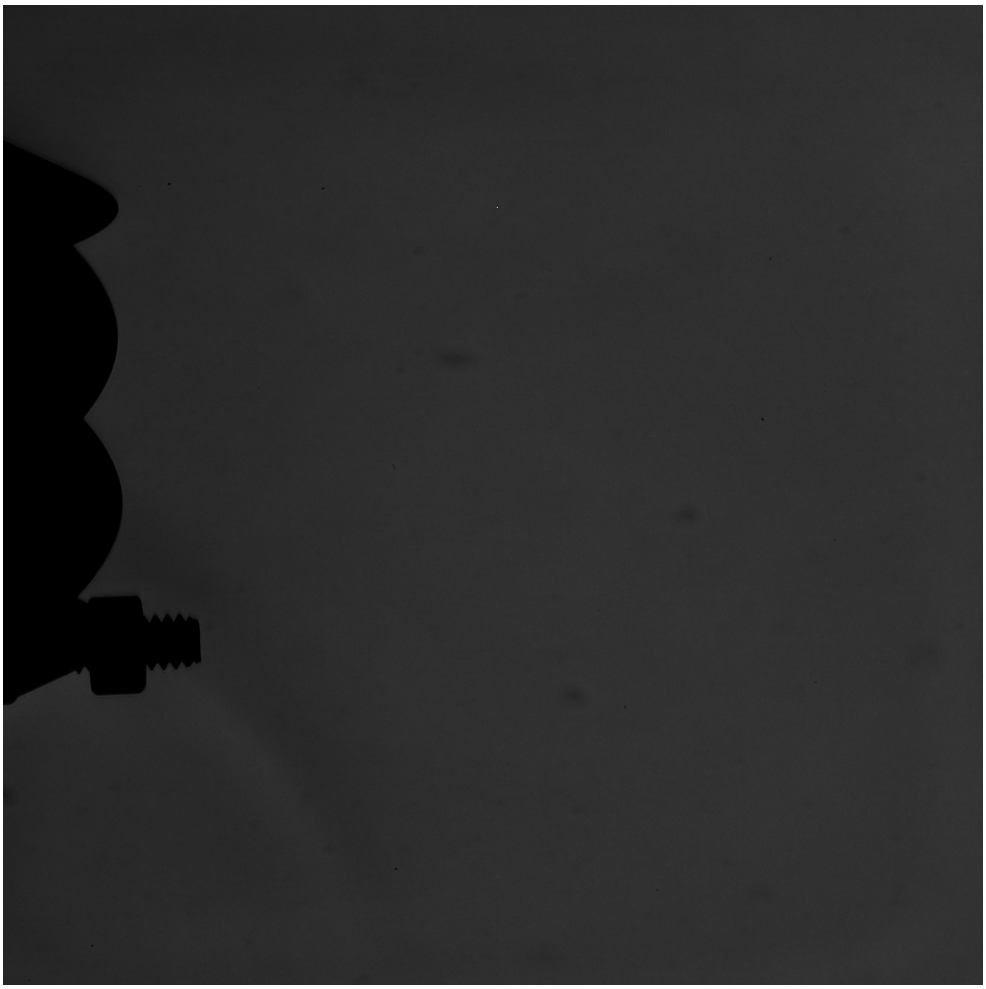

Figure 34. Schlieren Calibration Image

3.6 Image Analysis

Analysis was accomplished utilizing the image processing program called ImageJ. ImageJ is a public domain tool developed by the National Institutes of Health and the

Laboratory for Optical and Computational Instrumentation. ImageJ was selected due to its ability to accommodate spatial calibration to provide real-world dimensional measurements. Once the image in Figure 34 was used to calibrate the program, pixel lengths could easily be converted to millimeters.

Schlieren recordings from the Photron Fastcam were trimmed to include only the tunnel operation to minimize data consumption and storage. Images from the beginning of the first quasi-steady period and the end of the second quasi-steady period were captured and imported to ImageJ. If chipping or damage occurred to the model, then an image was captured at the latest frame preceding the damage. The before and after pictures were then imported to and aligned within ImageJ. It was observed that shape change mainly occurred at the nose of the body, and ablation further down the cone was negligible. Additionally, work by Callaway and Onay and Eyi also indicated that most ablation occurs near the stagnation point of the cone [28]. This allowed the before and after images to be aligned by the body shape so that the nose recession could be determined. ImageJ includes an edge-finding tool that facilitates aligning the before and after images. Once the images were aligned, the number of pixels that had eroded was converted to millimeters to determine recession rates.

3.7 Safety Analysis

The safety analysis performed prior to this research relied on conservative estimates to ensure safety. The assumed mass of the dry ice block was 2.4 kg, but the actual nose cones had a mass of less than 0.5 kg after formation. Additionally, while the nose cone portion of the dry ice blocks occasionally failed during testing, the cuboid portion was always secured by the mounting screws, meaning only half of the model mass could come loose. Furthermore, failures mostly occurred during the end

of the tunnel run, where and flow velocity approaches subsonic speeds. Most failed models simply slid out of the holder and were not blown down the Ludwieg Tube. A full safety analysis is presented in Appendix A.

IV. Results and Analysis

Chapter IV presents and discusses the experimental results of the research effort. It will discuss the test instances, the qualitative observations of the dry ice models, as well as quantitative recession rate measurements of the simple and bi-conic dry ice models, and a stagnation point heating analysis. The initial focus of this effort was exploratory since neither ablation measurements nor the use of dry ice models for any other purposes had previously been attempted in the AFRL Mach 6 Ludwieg Tube facility. Qualitative findings from the experiment are primarily presented chronologically in order to provide context to what was learned through the study, especially with respect to model-forming and test procedures. Quantitative findings for ablation rate are provided in Section 4.3. At the outset of the study, it was unknown whether models would even survive the tunnel start-up or whether the ablation rate would be high enough to yield any useful information. Gathering qualitative images was an important step in the process. After only a few tests, it was recognized that improvement in testing might be accomplished by developing a more advanced method for holding the model precisely in place during wind tunnel runs. Since there was no assurance that an improved holding method could be achieved in a timely fashion and because the collected results were encouraging, it was decided to proceed with testing.

4.1 Test Instances

A total of 42 tests were performed. A single run was conducted with the empty dry ice holder to ensure stability, 35 runs were conducted with the simple dry ice cone model, and 6 were conducted using the bi-conic model. A full test matrix can be seen in Appendix B.

The goal of the initial runs was to test the survivability of the dry ice model across the spectrum of stagnation pressures and Reynolds numbers capable of being produced by the Ludwieg Tube. The Ludwieg Tube was first operated at its lowest stagnation pressure of 40 psi. Tests were next performed at stagnation pressures of 100, 150, 200, and 300 psi. The earliest models featured blunt noses due to a concern that a sharp tip may break off mid-run. An example of a blunt-nosed cone can be seen in Figure 35.

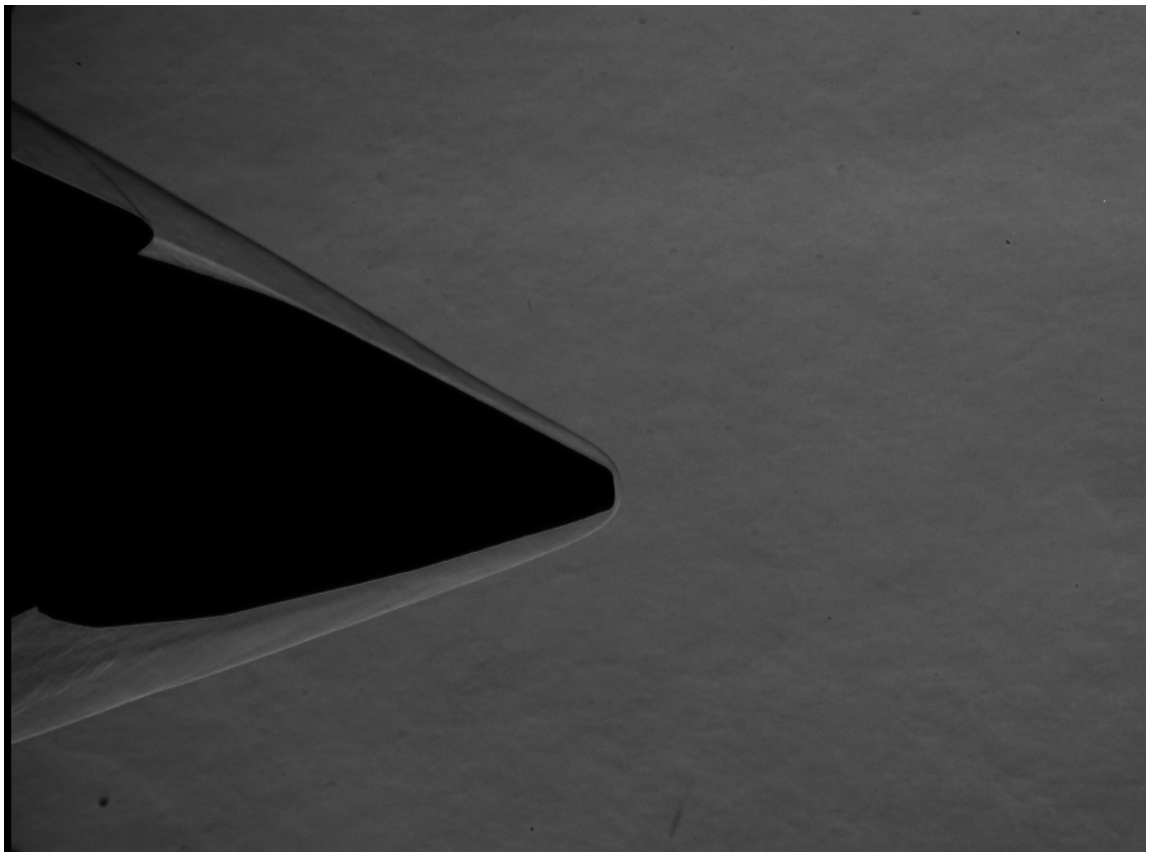

Figure 35. An Example of a Blunt Dry Ice Cone

Once it was observed that the models could survive up to moderate stagnation pressures, the nose of the models were made to be as sharp as possible, as sharper leading edges were expected to experience greater ablation rates. The early tests also allowed an opportunity to improve the model manufacturing process, and to

determine likely causes of failure within the tunnel. It was observed that models with sharp leading edges, such as in Figure 36, could survive moderate stagnation pressures as long as cracks had not formed during the manufacturing process. Several tests were also performed to determine if a dry ice model could be resharpened and survive multiple test runs. It was found that some of the models could survive multiple tests, even at high stagnation pressures. The reused models did have a higher failure rate and could only be resharpened a single time before they were too short for the mold.

Next, runs with the dry ice model were performed near the maximum operating stagnation pressures of the Ludwieg Tube. It was observed that the models used reliably survived stagnation pressures of 400 psi, with three of the five runs providing useful data. One of the two models that broke up mid-run was used repeatedly at progressively higher pressures and was not expected to survive. However, at 500 psi the model failed by cracking in two of the three runs. After demonstrating that the dry ice models with sharp leading edges could reliably survive a wide range of stagnation pressures the next goal was to obtain at least three successful runs in 100 psi increments for use in quantitative analysis to measure recession rates. Finally, a method for constructing and testing the bi-conic models was developed to observe a model with greater recession rates. An example of a bi-conic model can be seen in Figure 37. The bi-conic model was tested at stagnation pressures of 100, 200, and 300 psi, and was found to have s imilar survivability to the simple cone models.

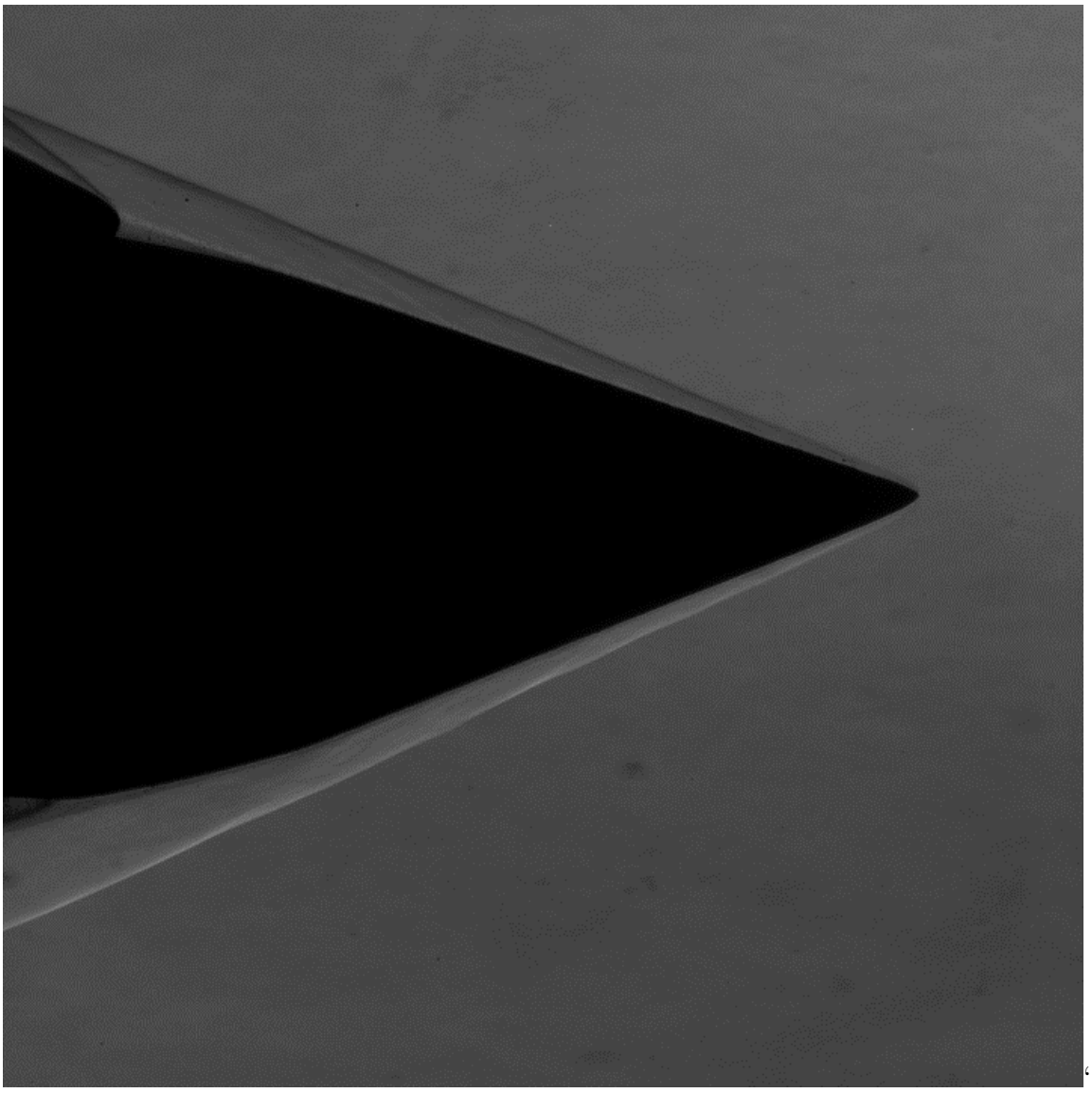

Figure 36. An Example of a Dry Ice Cone Model with a Relatively Sharp Tip

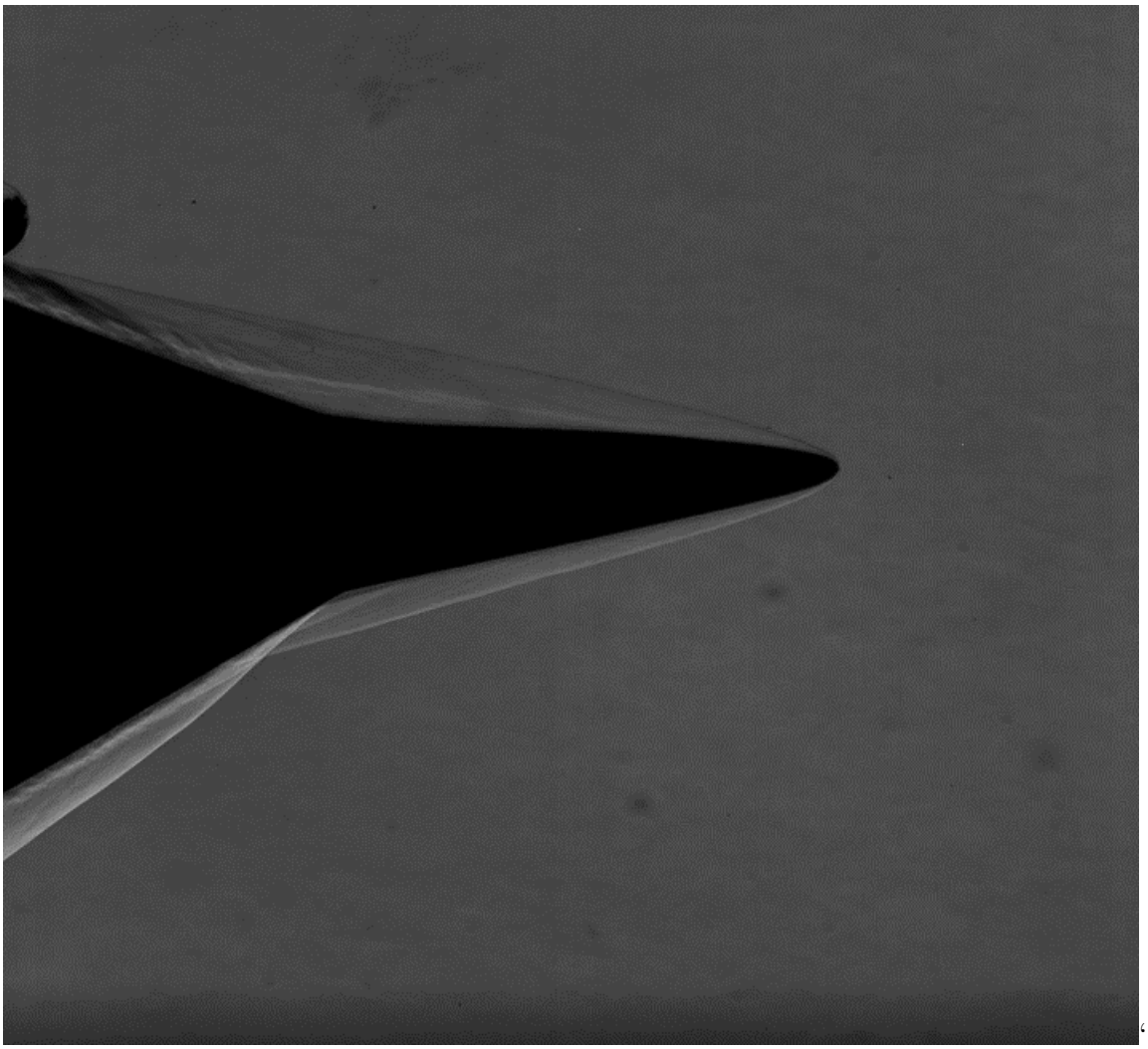

Figure 37. An Example of a Bi-Conic Model

4.2 Qualitative Observations of Dry Ice Models

There was a multitude of notable observations made throughout the course of testing. Many of these observations were predicted by previous research, but several were unique to this test setup. One of the concerns of previous cryogenic tests performed in the Ludwieg Tube was controlling the formation of frost. Frost formed on the cooled test articles due to freezing moisture within the laboratory atmosphere. Frost alters the surface roughness of the test article, which will accelerate the transition of laminar to turbulent flow. Previous research averted this issue by keeping the test article in a vacuum throughout the duration of tests. This was not possible, as the test chamber was exposed to the laboratory atmosphere each time a new dry ice model was installed. A modest amount of frost formation was observed on both the test stand and on the dry ice models. A model with frost can be seen in Figure 38.

Air rushing past the model immediately after the fast-valve actuation appeared to quickly remove any frost that had built up on the surface, as seen in Figure 39. The absence of a shock indicates that the frost is being removed before the test section enters the first quasi-steady period. The surface frost was removed by the time the tunnel has reached the first quasi-steady period, and the models appeared as they did in Figure 36. Additionally, frost formed on the dry ice holder as well but did not impact the flow as it is located downstream of the dry ice model. Ultimately, the frost was present but did not appear to affect the results of the experiment.

The dry ice blocks were designed to have a 2" x 2" base, but during the course of fabrication, installation, and tunnel charging time, sublimation would cause one of the dimensions to be less than 2". Having a slightly smaller base was practical, as the dry ice block was difficult to force into the holder when it was below the carbon dioxide triple point. These gaps, however, allowed stagnation air inside of the holder.

A gap that formed due to insufficient cooling can be seen in Figure 40. In this

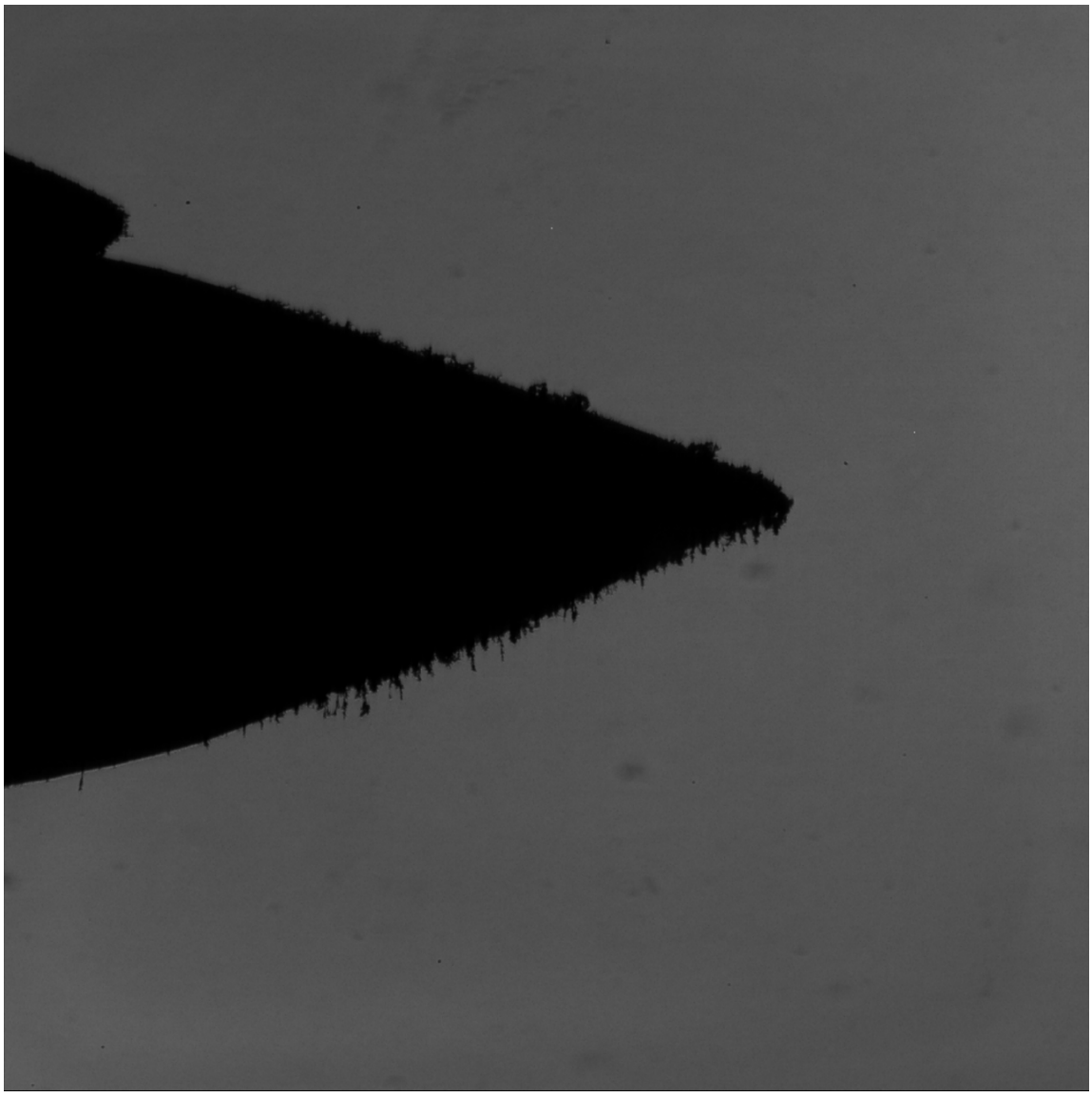

Figure 38. Dry Ice Model with Frost

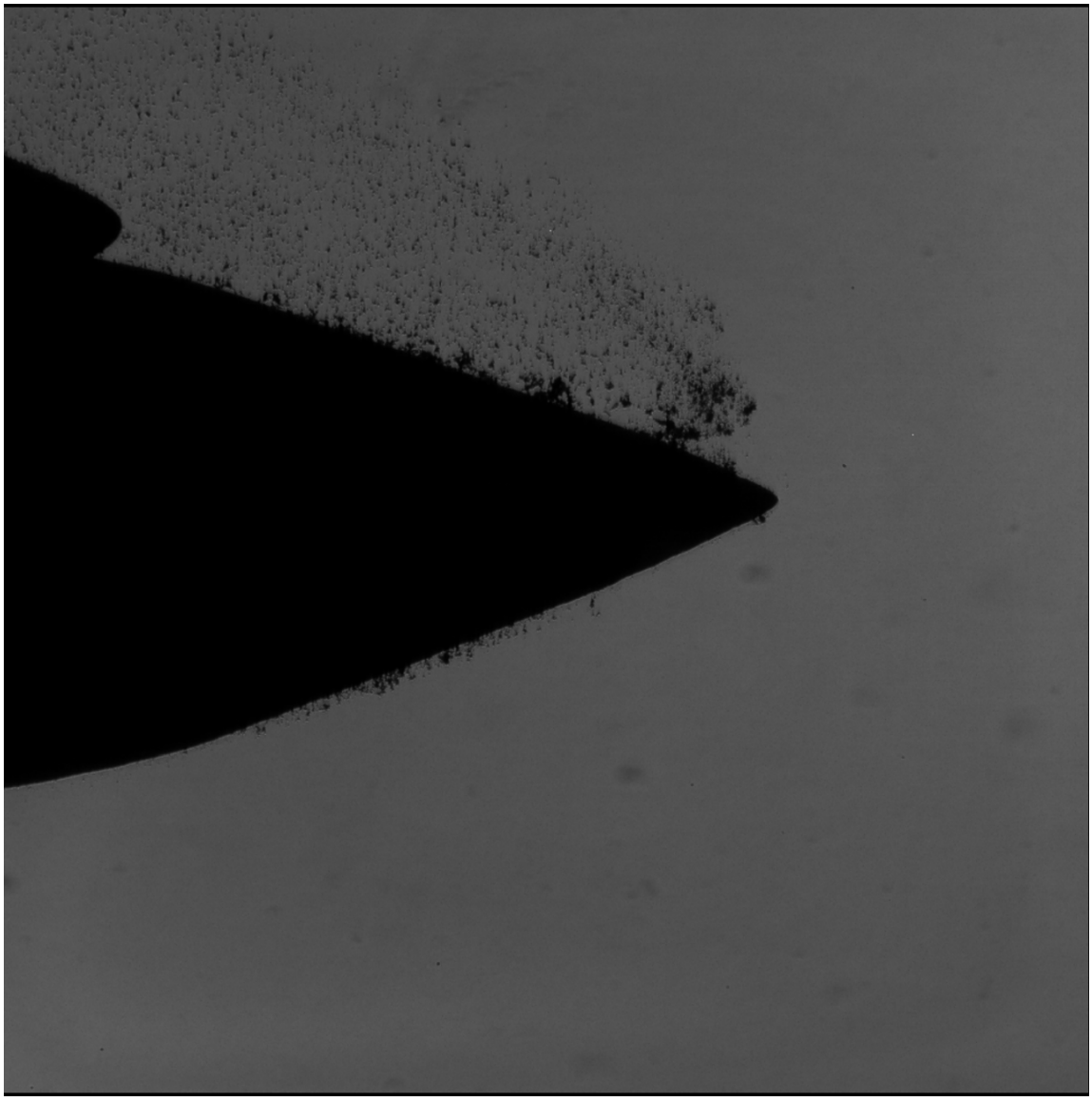

Figure 39. Model During Tunnel Start-up

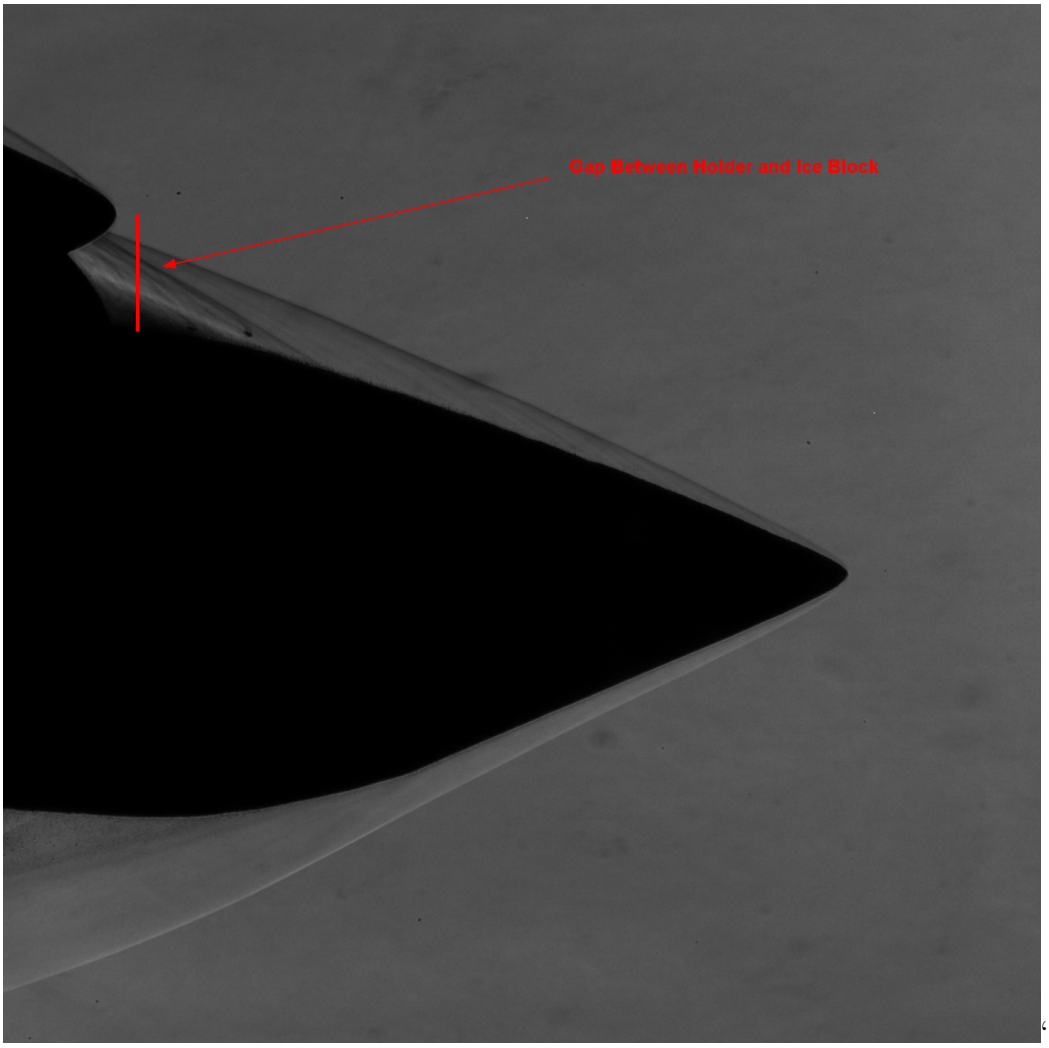

Figure 40. Gap Between Dry Ice Holder and Model

case, the gap is large enough that the shockwave appears to pass below the petal on the holder. The air within the holder applied pressure to the model and could force the model to shift upstream, even with the holder screws. This was an unexpected result. The results of stagnation pressure near the rear of the model ranged from forcing the model upstream a few millimeters, to completely ejecting the model from the holder, as seen in Figure 41.

Figure 41. Ejected Model During 500 psi run

At lower stagnation pressures, this effect was not significant. Models could survive runs at 100 or 200 psi even with large gaps present. At higher pressures, a large gap

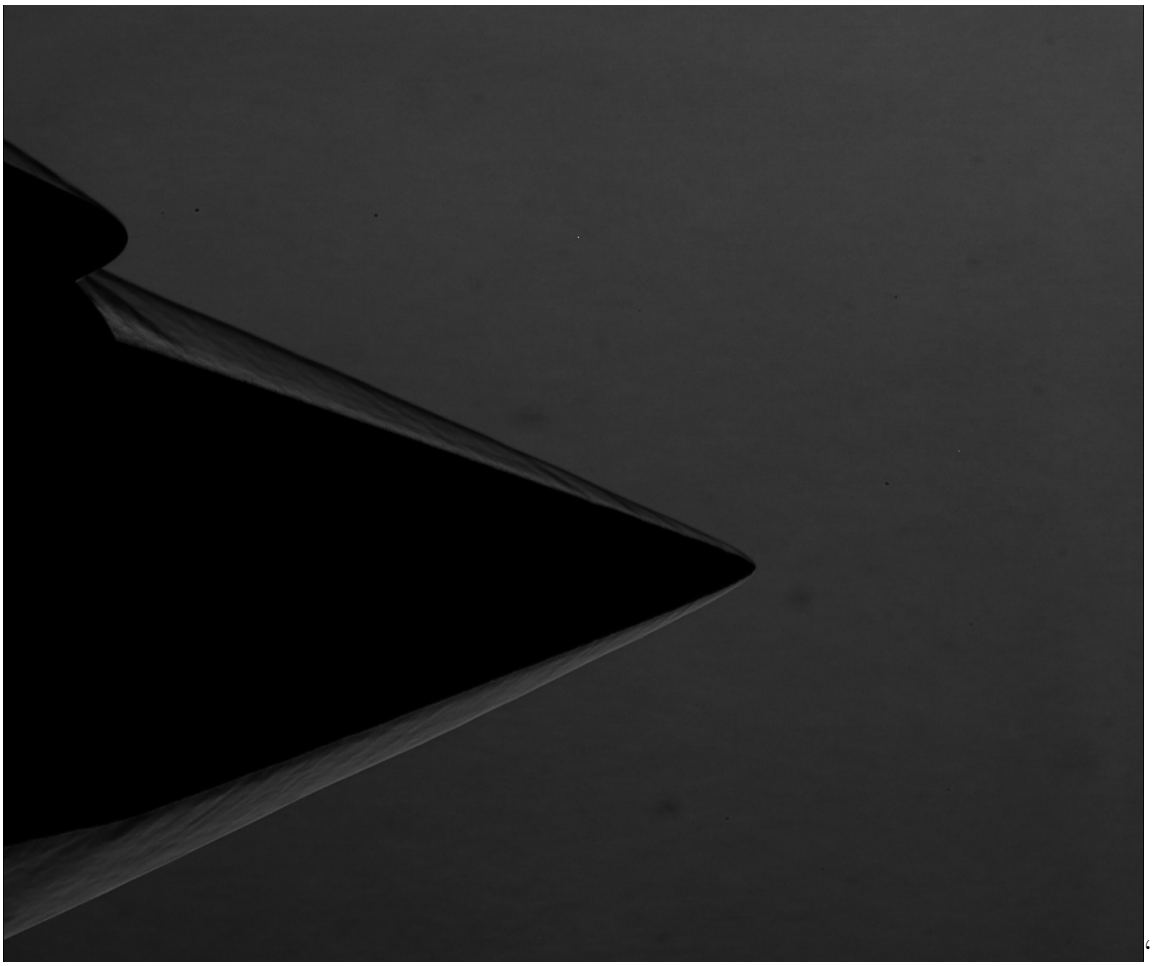

Figure 42. Beginning of 500 psi run

between the model and holder could result in the model being forced out of the schlieren frame or holder. There were, however, cases where even high-pressure tests survived with relatively large gaps. Figure 42 shows a model which contains a visible gap that was used in the 500 psi run. The model was simultaneously forced upstream and increased its angle of attack. The increased angle of attack formed a seal between the holder and model, which can be seen in Figure 43. Once a seal had formed, the model remained firmly in place for the duration of the run. This model was the only one of the three tests to survive a run with a stagnation pressure of 500 psi. Figure 41 shows a model that has completely ejected from the holder.

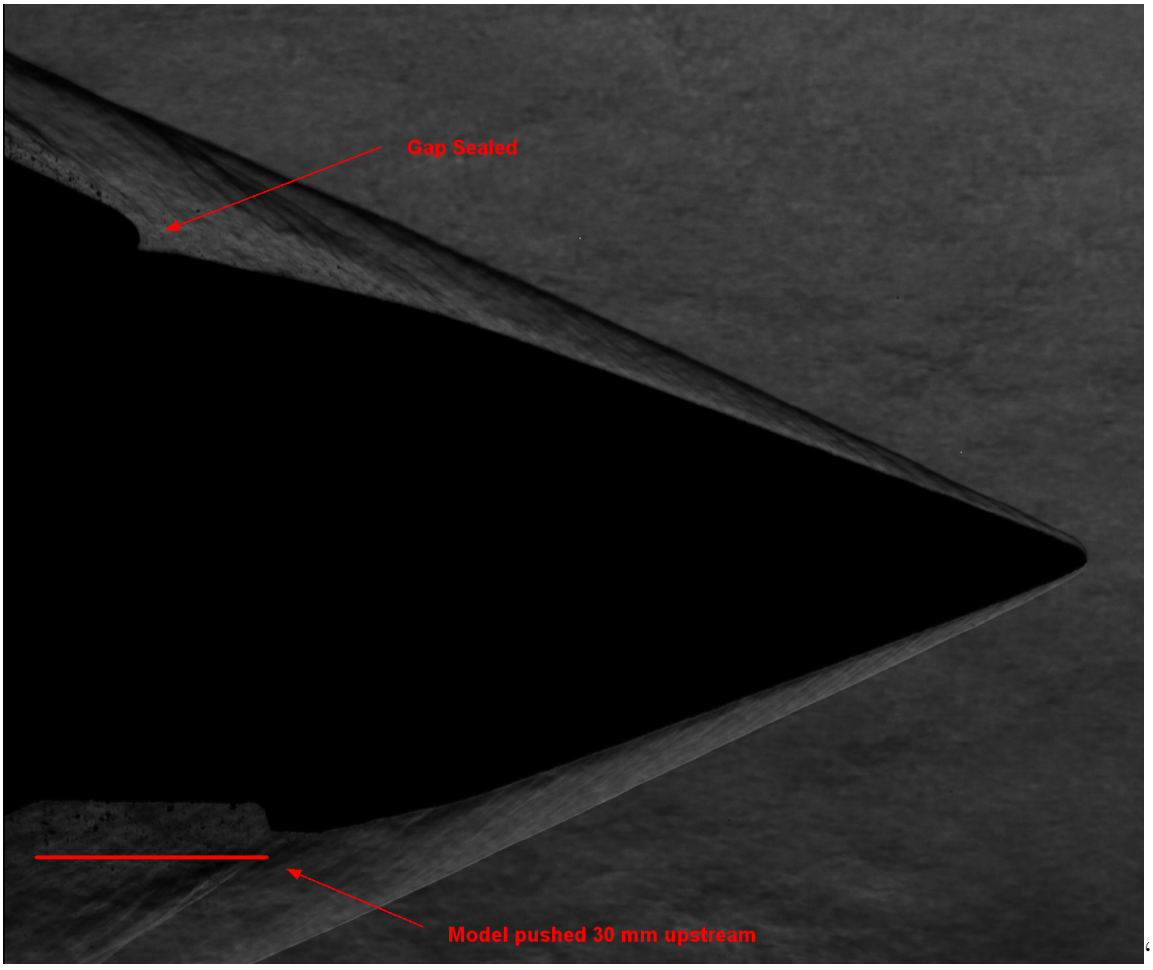

Figure 43. End of 500 psi run

The dynamic pressure of the flow, combined with the pressure within the dry ice

holder, also caused slight variations in the model's angle of attack throughout the run. This was present during runs across the spectrum of stagnation pressures but appeared to be more pronounced at higher stagnation pressures. This did not appear to affect the dry ice model structure but made image analysis more challenging. An overlay of a dry ice model at two different periods can be seen in Figure 44, illustrating the extent of the angle of attack variation. This run was performed at 300 psi, and the images were captured at t = 0.05 s and t = 0.1 s. The angle of attack varied by approximately 3° between the two images.

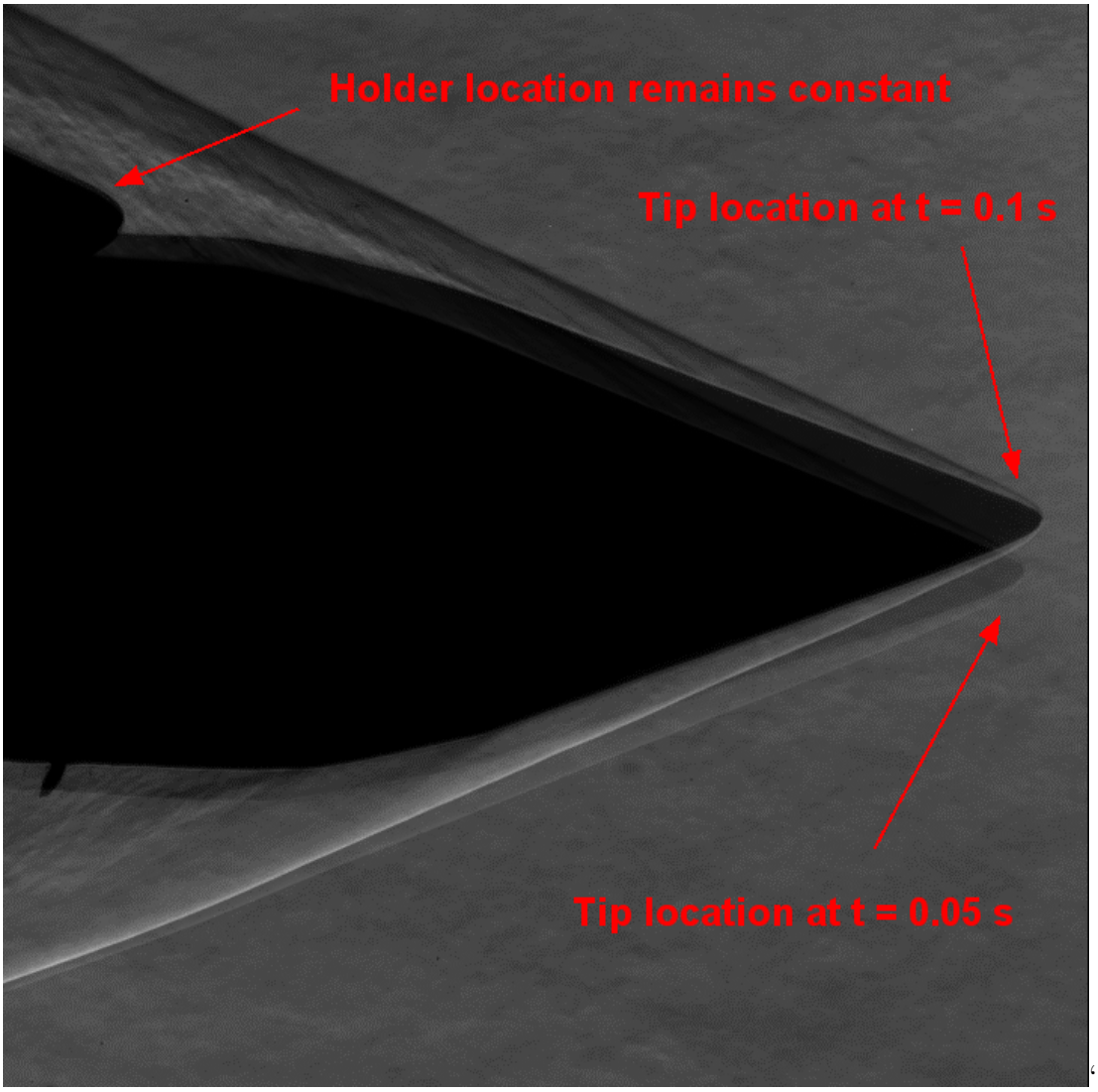

Figure 44. Angle of Attack Variation in 300 psi Run

The combined forces of air within the holder and dynamic pressure from the freestream caused led to stress on the dry ice models. This stress either exacerbated existing cracks or caused new ones to form, ultimately resulting in model breakage in several runs. The conic portion of the model proved to be resilient to the tunnel forces. Developing a means to prevent the model from moving during tunnel operation would likely increase the model survivability, and would also make post-processing less complicated.

Small particles could be observed breaking off from the dry ice model and flowing downstream in some of the runs. For the most part, these particles could be seen detaching from the rear portion of the cone, and did not have an impact on test data. Occasionally, large particles blown off the nose portion caused an obvious shape deformation if it was within the plane of view. Figure 45 shows visible chipping that was particularly severe from the nose of a dry ice cone during a 300 psi run. This image was taken from the first 0.05 s of quasi-steady period 1. The red arrows in Figure 45 indicate particles that detached from the nose and can be seen flowing downstream.

Figure 46 was taken midway through quasi-steady period 2, around 0.15 s into the run. Here, the result of the accumulated chipping is visible. The nose of the cone has an irregular shape. Instead of a gradual rounding, the nose has recessed pockets across the curve where chunks of ice have broken loose. In this case, it is difficult to differentiate between nose recession due to ablation versus chipping. To avoid conflating ablation and chipping, data was recorded until the chipping phenomenon was visibly altering the nose shape in the cases where the particles were significant. Chipping did not directly contribute to nose recession rates in this experiment. In general, the runs that were analyzed either did not experience chipping or the chipping phenomenon was confined to later parts of quasi-steady period 2.

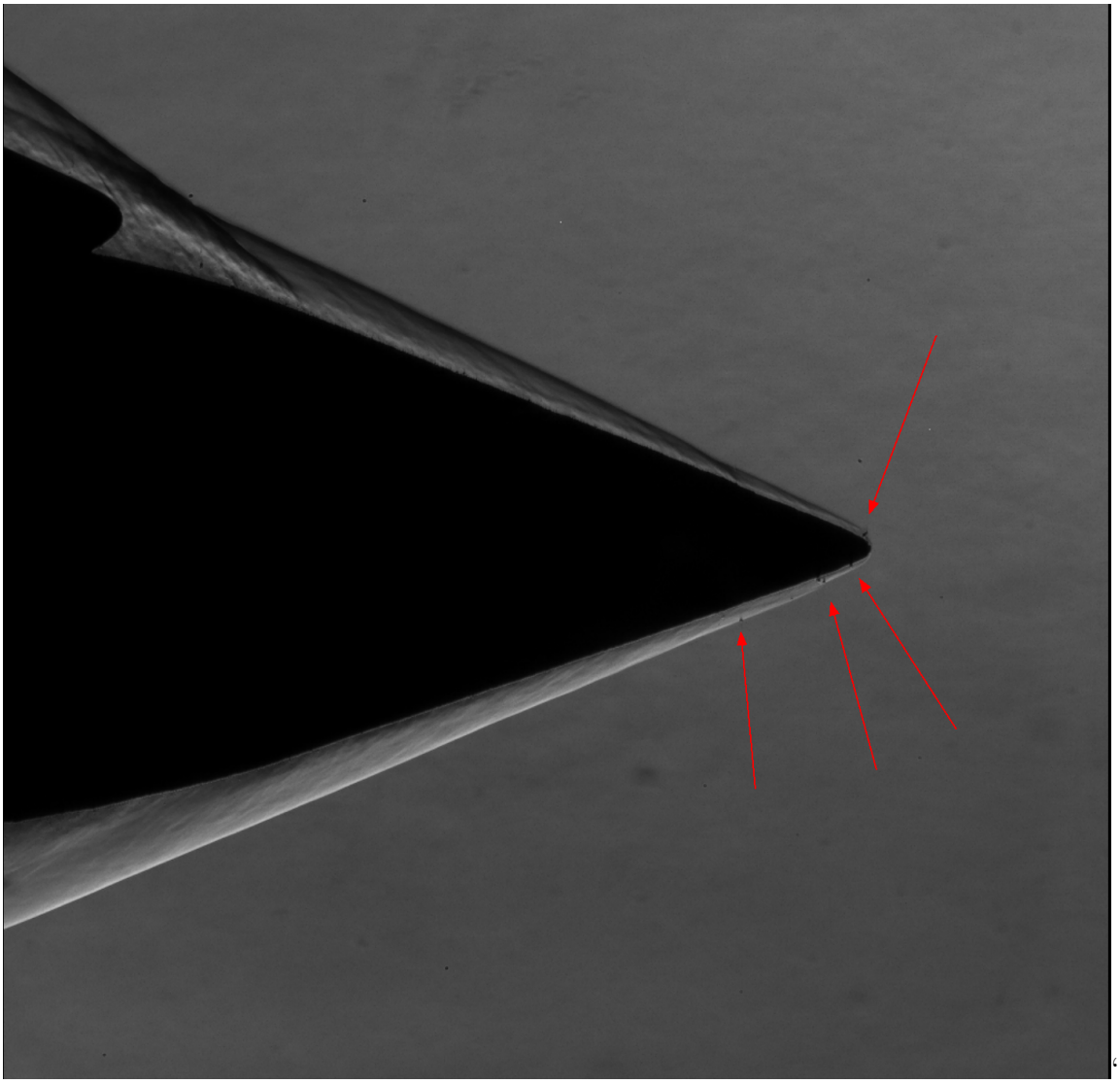

Figure 45. Visible Ice Chips Breaking From Nose during 300 psi run

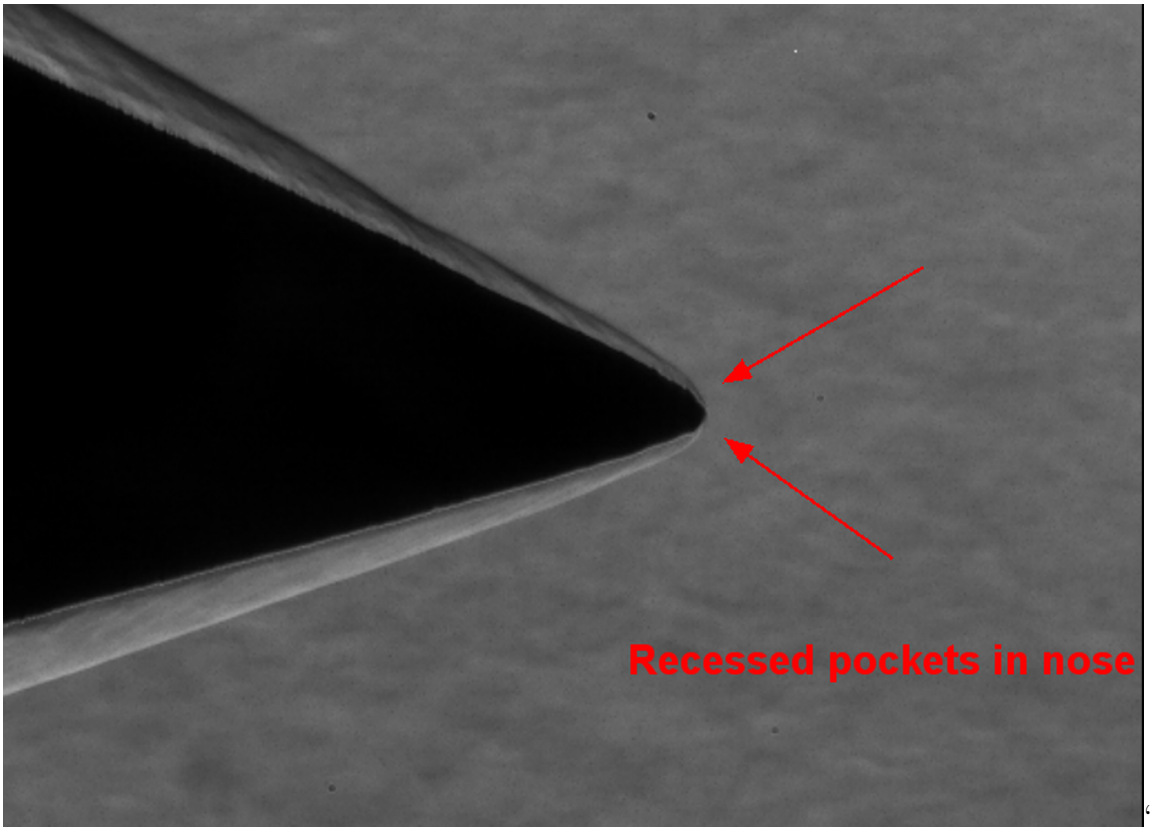

Figure 46. Nose Recession due to Chipping during 300 psi run

Like many of the other phenomena previously mentioned, the frequency of observable chipping tended to increase with tunnel stagnation pressure. Additionally, the onset of chipping was generally accelerated by higher stagnation pressures. During the 100 psi runs chipping was generally not observed. Chipping was observed in only one of the three 200 psi runs which were analyzed but did not occur until the end of quasi-steady period 1. Chipping was especially pronounced in the 300 psi runs, even more so than the 400 psi runs. Chipping in the 500 psi runs was the most severe, and occurred almost immediately into the runs.

Chipping was observed in previous experiments, particularly in Anderson's. In Anderson's experiments, the flaking was so significant that no usable data could be garnered from the dry ice experiments. In this experiment, the particles usually were not substantial enough to impact the results. The decreases in ice flaking were likely due to the higher density of commercially procured dry ice and improved manufacturing process. This phenomenon appears to be analogous to spallation, which has been observed in ablative heat shields during re-entry [12].

4.2.1 Qualitative Assessment of Cone Models

Overall, the cone models proved to be resilient within the Ludwieg Tube once the manufacturing process had been sufficiently developed. Ten of the eleven models used over the course of the final two days within the Ludwieg Tube survived their runs ranging from 100 - 400 psi.

On many runs, a recirculation region could be seen forming at the back end of the cone. These regions are observable due to visible pieces of dry ice floating or even flowing upstream. Particle Image Velocimetry (PIV) could be utilized in future research to gain insight into flow characteristics within this region. A large particle tracking can be accomplished by tracking ice particles flowing upstream.

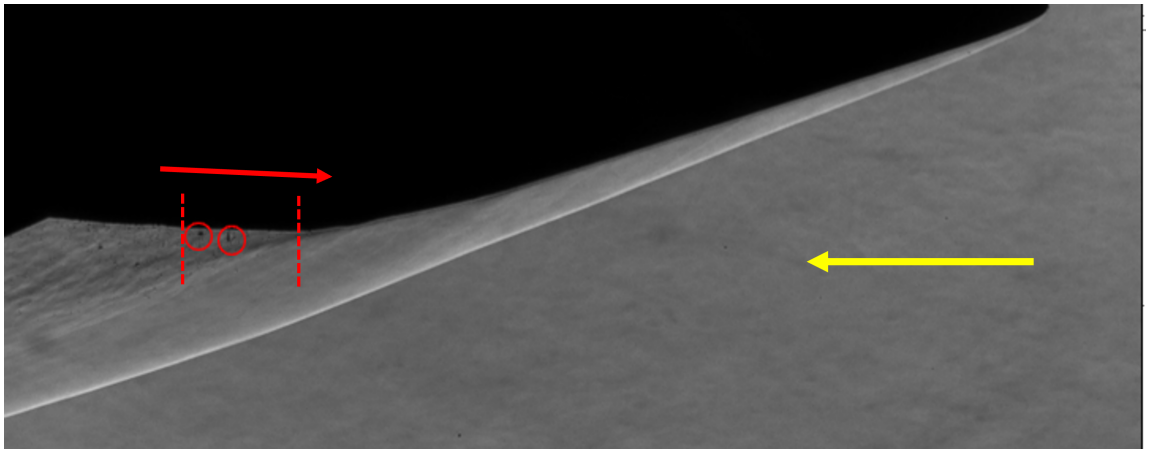

(a) t= 0.0000 sec

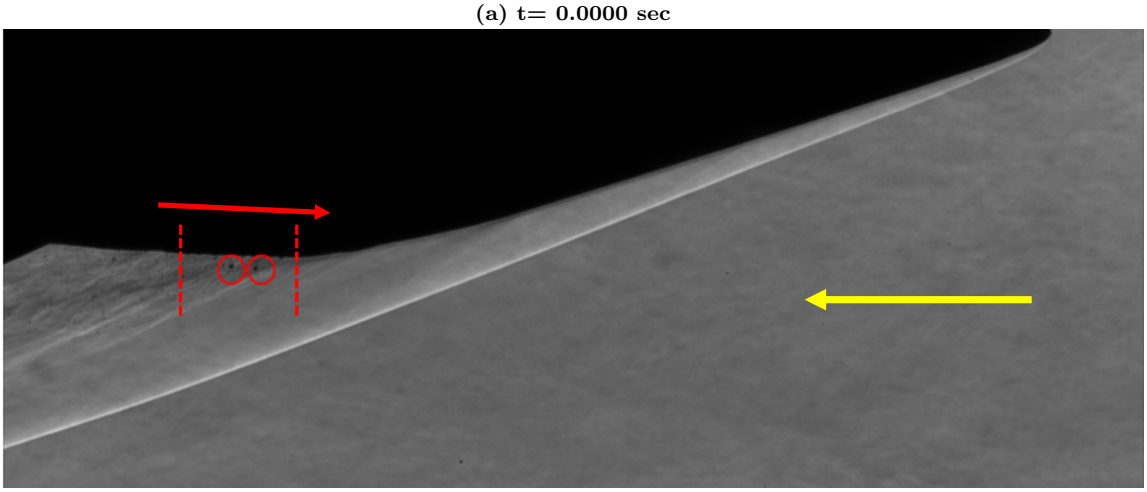

(b) t= 0.0015 sec

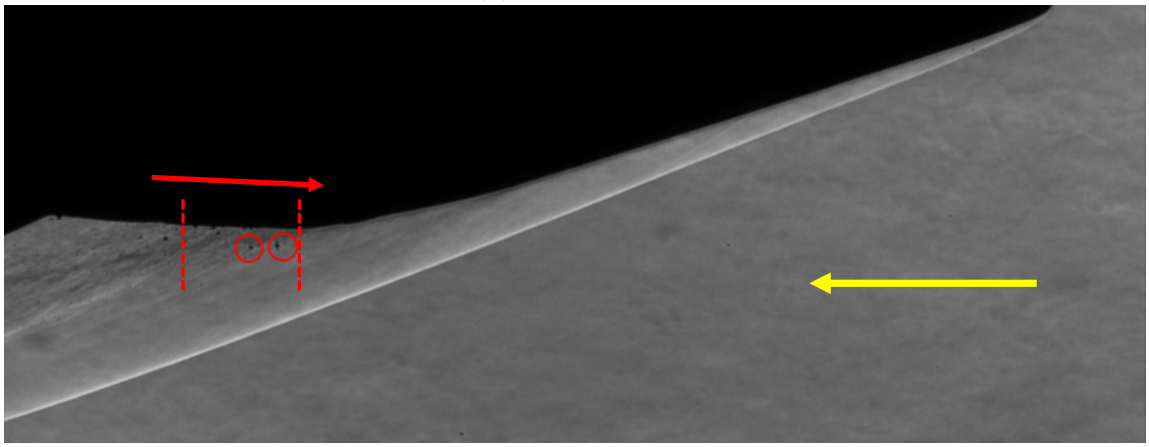

(c) t= 0.0030 sec

Figure 47. Large Particle Tracking within Re-circulation Region, Red Arrow Indicates Direction of Particle Motion, White Arrow Indicates Direction of Flow

In Figures 47a, 47b, and 47c show three sequential images at a time increment of 0.0015 seconds. The red arrows indicate the direction of motion of the dry ice particles, and the white arrows indicate the direction of the flow. Figures 47a, with a reference time of t = 0 sec, shows two highlighted particles that are easily identified without requiring image magnification. In Figures 47b and 47c the particles can be seen progressively moving upstream. the flow passing down the body of the cone and are quickly whisked off the screen.

Among the three images, the particles move approximately 3.5 mm during the course of 0.003 seconds. This results in a velocity of 1.2 m/s which is far below the freestream velocity of 931.7 m/s.

4.2.2 Qualitative Assessment of Bi-conic Models

A notable feature of the bi-conic model is the shock-shock interaction just after the point where the nose meets the base section, which can be seen in Figure 48. Anderson classifies this as a type-VI shock interaction. In a type-VI interaction, two left running shocks intersect far downstream of the sonic point behind the bow shock. The two shocks then coalesce into one shock with a slip line trailing downstream from the intersection point [2]. While in most tests the model angle of attack varied around $\pm 3^{\circ}$, the test in Figure 48 reached an angle of attack of approximately 10°. Regions behind shock-shock interactions have been observed to exhibit extreme heat rates. During the last flight of the X-15, a dummy scramjet attached to the vehicle by a pylon was melted off due to type IV and V shock interfaces [23].

Like the simple cone models, the bi-conic models were also resilient to the forces created by the Ludwieg Tube even with the narrow leading edge. However, they tended to be harder to form and were only tested to 300 psi. Models for four of the five tests with the bi-conic remained intact throughout the run. The one failure was

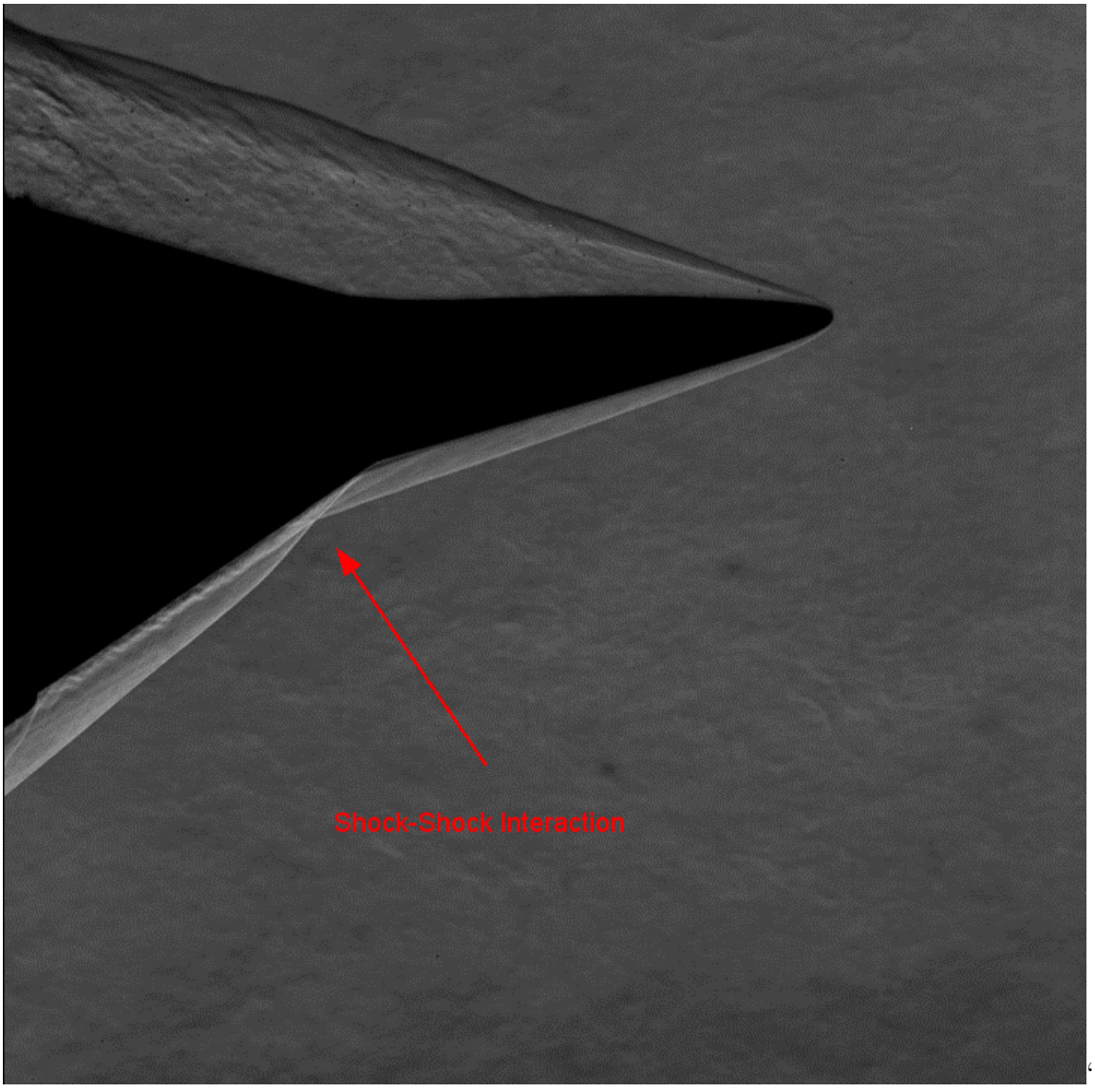

Figure 48. Bi-conic Model Shock-Shock Interaction

due to back-pressure forcing the model out, rather than the nose breaking. A bi-conic model did fail due to the nose breaking, however, the crack in the nose was noticed during construction. In previously cracked models, the crack was located within the dry ice holder and therefore was not visible to the schlieren imagery.

The bi-conic test with model breakage can be seen in Figures 49a, 50a, and 50b. This test was performed at a stagnation pressure of 200 psi. In Figure 49a the model can be seen surviving through startup into quasi-steady period 1. In Figure 50a, the nose can be seen breaking at the crack location. The forward nose section was the most likely to break during model construction. Figure 50b shows the model after the crack, where the leading edge is so blunt that a visibly detached bow shock has formed. The remainder of the model survived the test. Observing this test indicated that the dry ice was fairly survivable as long as no cracks had formed.

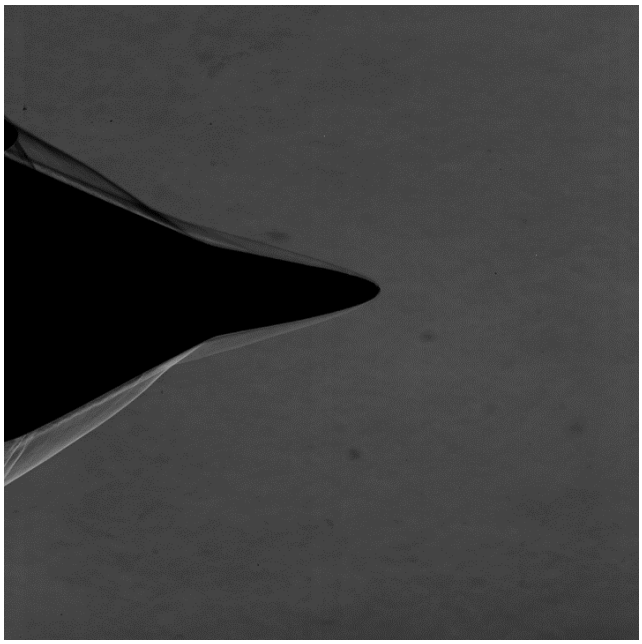

(a) Start of Cracked Bi-Conic Model Test

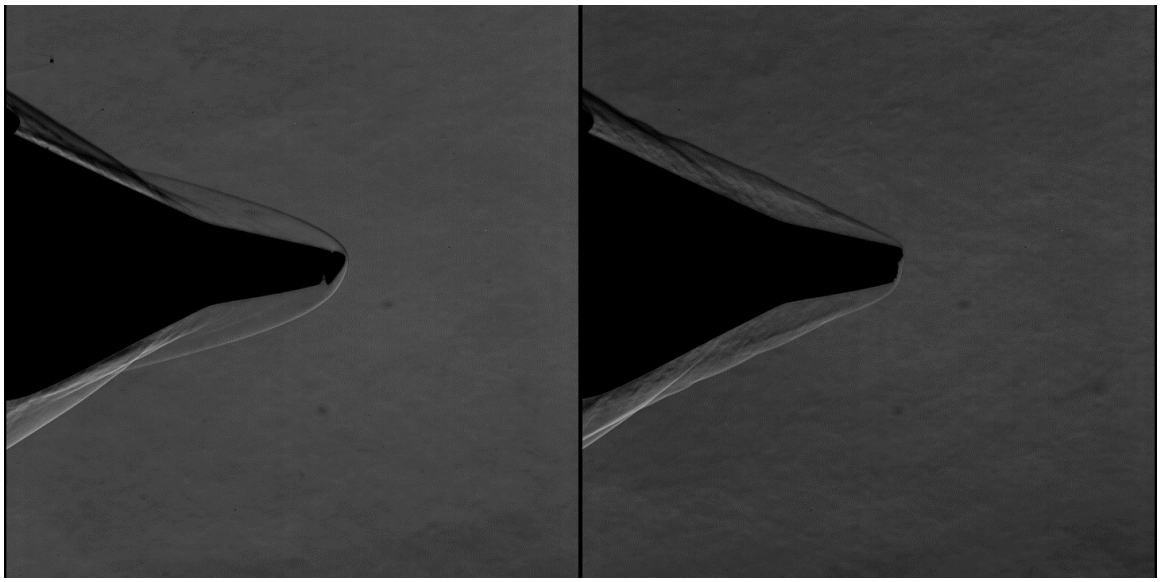

(a) Nose Breaking from Bi-Conic Model **(b) Model After Nose Detached**

Figure 50. Bi-conic Model Breakup

4.3 Quantitative Analysis

The nose recession rate was calculated by dividing the measured nose gap by the time between the two images. The time was calculated by dividing the number of frames between the images by the FPS of the camera, which was 20 kHz. The equation used was:

$$\text{Recession Rate (mm/s)} = \frac{\text{\# Pixels} \times \frac{0.25in}{40\text{pixels}} \times \frac{25.4mm}{1in}}{\text{\# Frames} \times \frac{1sec}{20{,}000 \text{ frames}}} \tag{7}$$

which returned the recession rate in units of mm/s. It should be noted that recession rates presented herein are average rates during the course of the run. The images were analyzed using ImageJ. ImageJ not only includes a built-in measuring tool, but also possesses the capability to detect edges in an image as well as an angle measurement tool. The edge detection was an invaluable tool, and it greatly facilitated the process of overlaying images. The before and after images were first overlaid so that an approximate difference in angle of attack could be determined. The after image was

then rotated to align with the before image, and the result was checked using the edge finding tool.

The opacity of the before image was reduced by 50% to prevent obscuring the edge of the after image. The edge of the cone was distinguishable from the background of the schlieren images, even with reduced opacity. A misaligned image of a simple cone model be seen in Figure 51. The multiple edges detected by the software indicate that the body of the cone is not properly aligned. An image of a bi-conic model that have been properly aligned can be seen in Figure 52. A single edge can be seen extending from the holder throughout the body of the cone, and two edges can be seen at the nose of the cone. This image indicates that the images have been properly aligned, and the difference between the nose edges can be measured. ImageJ's built-in measuring tool creates an adjustable line with the width of a single pixel on the viewing window. The line is measured once it has been adjusted to the desirable location and length. While this measuring tool is clearly visible to the researcher, it is difficult to capture in images for presentation. A thicker red line can be seen throughout the images presented herein to convey the approximate lengths and locations of measurements made. The process of determining ablation rates for several runs is shown in the following sections.

4.3.1 Run 31: $P_0 = 100$ psi, Simple Cone Model

The image captured at the beginning of quasi-steady period 1 can be seen in Figure 53a, and the image captured at the end of quasi-steady period 2 can be seen in Figure 53b. These images were determined to be separated by 0.2 seconds by dividing the number of frames between the images by the frame rate. As seen in Figures 53a and 53b, the model did not appear to shift during the run. This allowed the images to easily be overlaid, as seen in Figure 54a. Once the images were overlaid,

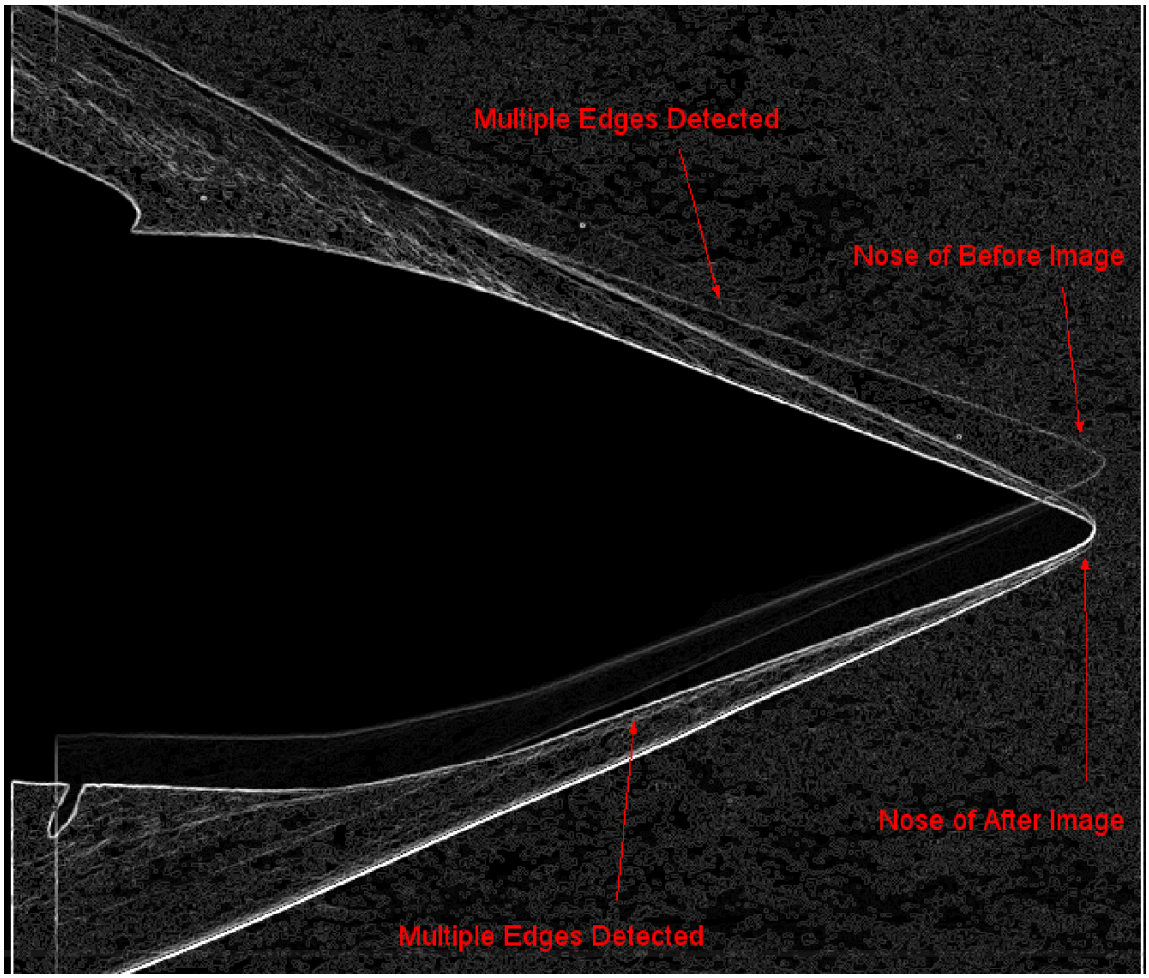

Figure 51. Overlaid Cone Images Showing Multiple Detected Edges

Figure 52. Overlaid Bi-conic Images Showing a Single Body Edge and Multiple Nose Edges

the difference between the nose lengths could be measured, as illustrated in Figure 54b. The average of three measurements was 2.9 pixels of nose recession. The number of pixels of nose recession and time between images was input into Equation 7 which returned an average recession rate of 2.4 mm/s.

4.3.2 Run 33: P_0 = 300 psi, Simple Cone Model

The image captured at the beginning of quasi-steady period 1 can be seen in Figure 55a, and the image captured at the beginning of quasi-steady period 2 can be seen in Figure 55b. Chipping was observed at the nose of the cone so the around t = 0.11 seconds, so data was only captured up to t = 0.105 seconds. As seen in Figures 55a and 55b, the model angle of attack slightly decreased, and the model shifted forward within the holder. This images were aligned and overlaid, which can be seen in Figure 56a. Once the images were overlaid, the difference between the nose lengths could be measured, as illustrated in Figure 56b. The average of three measurements was 4.3 pixels of nose recession. The number of pixels of nose recession and time between images was input into Equation 7 which returned an average recession rate of 6.2 mm/s.

4.3.3 Run 13: P_0 = 400 psi, Simple Cone Model

The image captured at the beginning of quasi-steady period 1 can be seen in Figure 57a, and the image captured at the end of quasi-steady period 2 can be seen in Figure 57b. The time between these images was 0.19 seconds. As seen in Figures 57a and 57b, the model shifted forward within the holder, but appears to maintain a constant angle of attack. This images were aligned and overlaid, which can be seen in Figure 58a. Once the images were overlaid, the difference between the nose lengths could be measured, as illustrated in Figure 58b. The average of three measurements

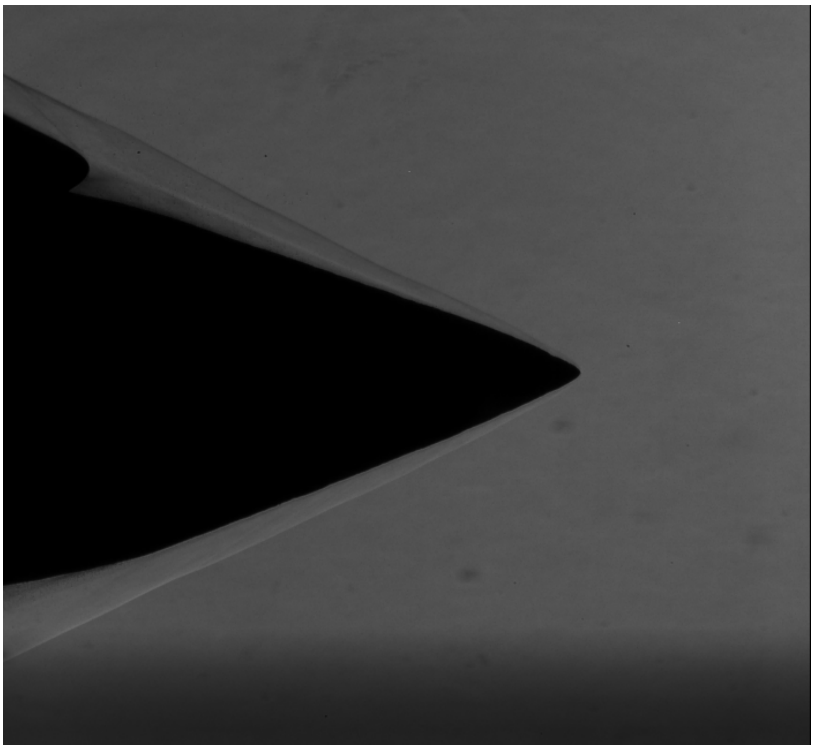

(a) Start of 100 psi Run, Simple Cone Model

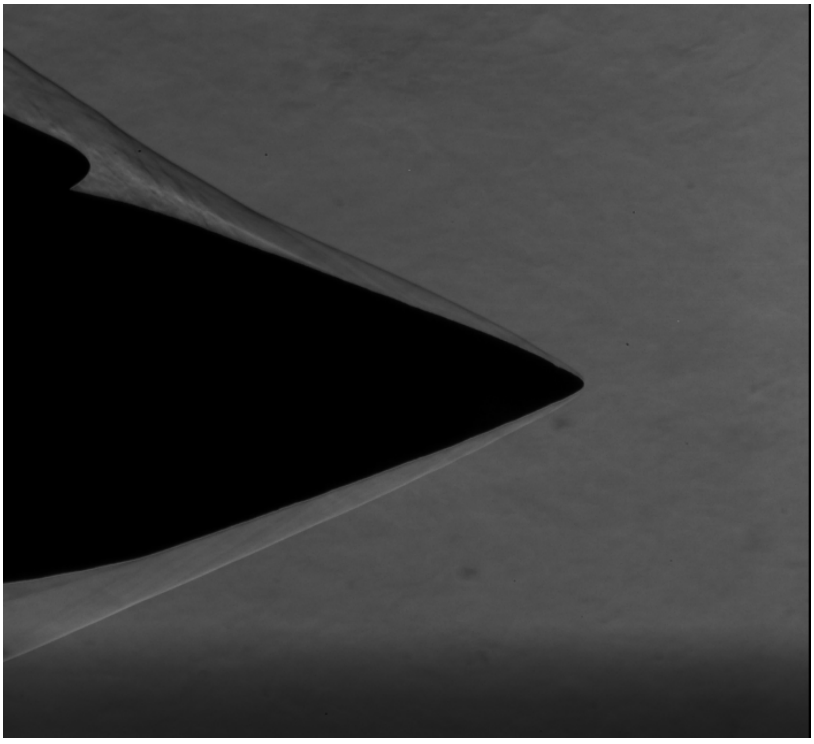

(b) End of 100 psi Run, Simple Cone Model

Figure 53. 100 psi, Simple Cone Images

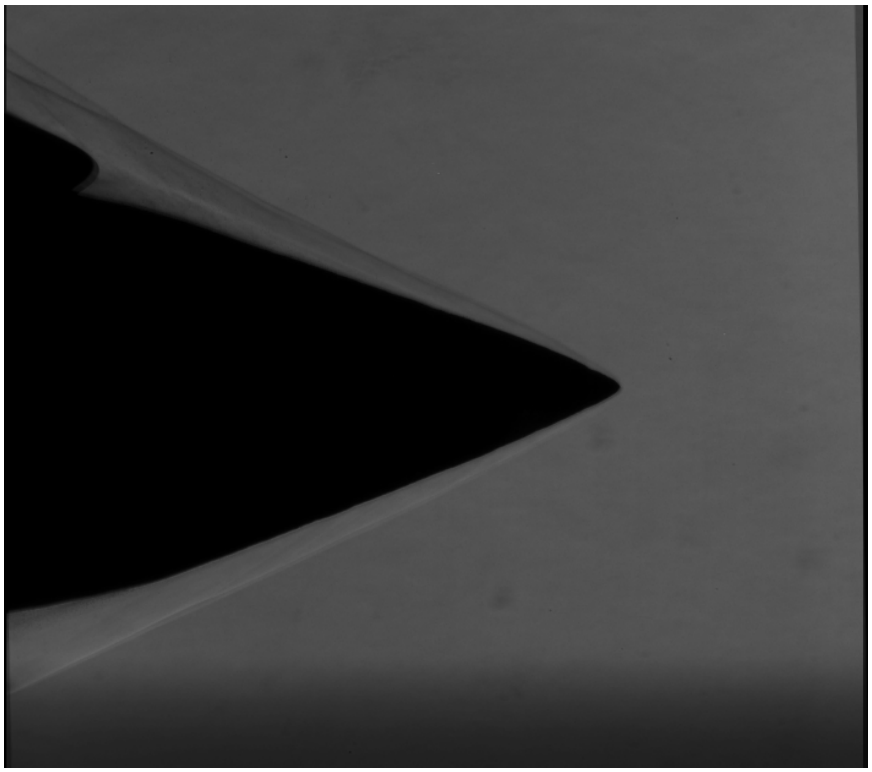

(a) Overlaid Simple Cone Model, 100 psi run

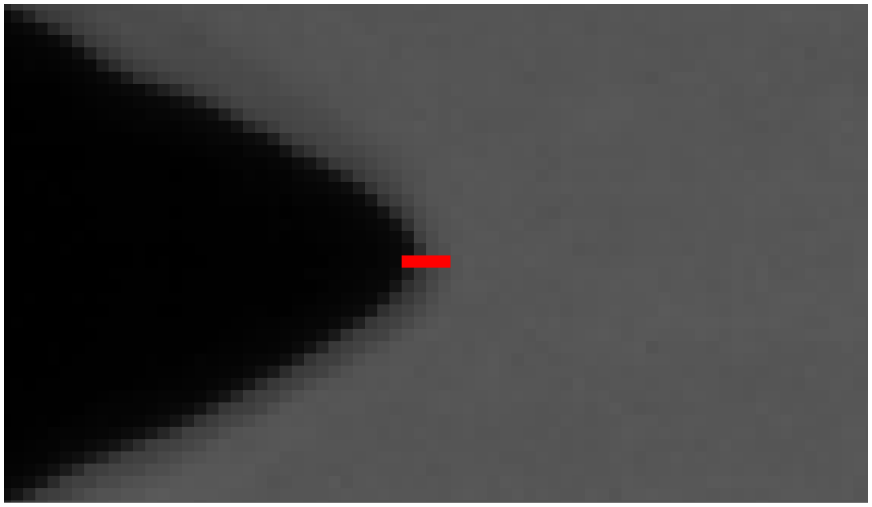

(b) Ablation Measurement of Simple Cone Model, 100 psi Run

Figure 54. 100 psi, Simple Cone Measurement

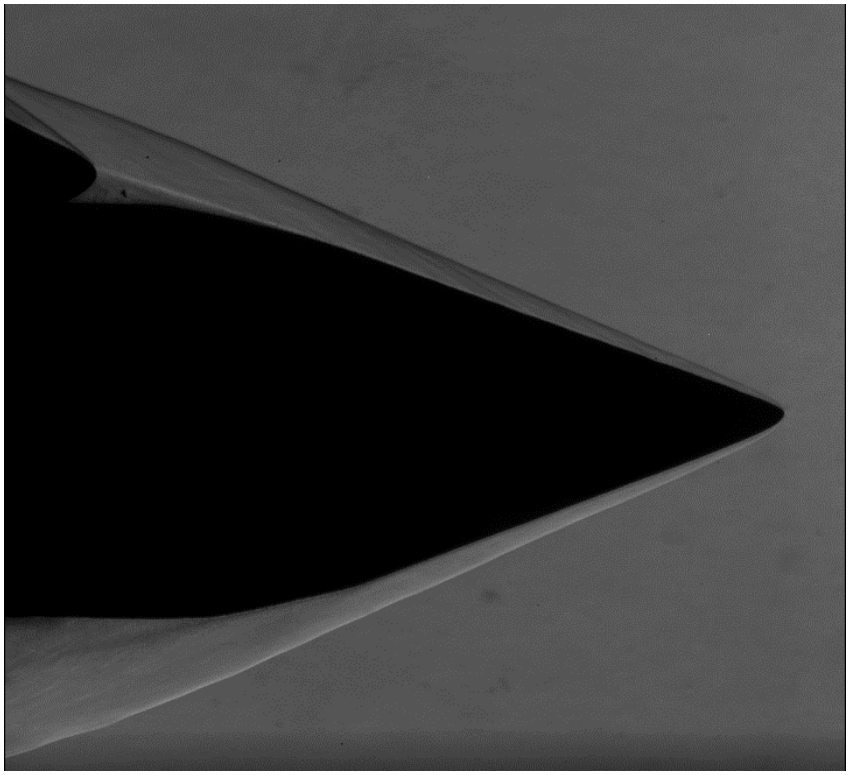

(a) Start of 300 psi Run, Simple Cone Model

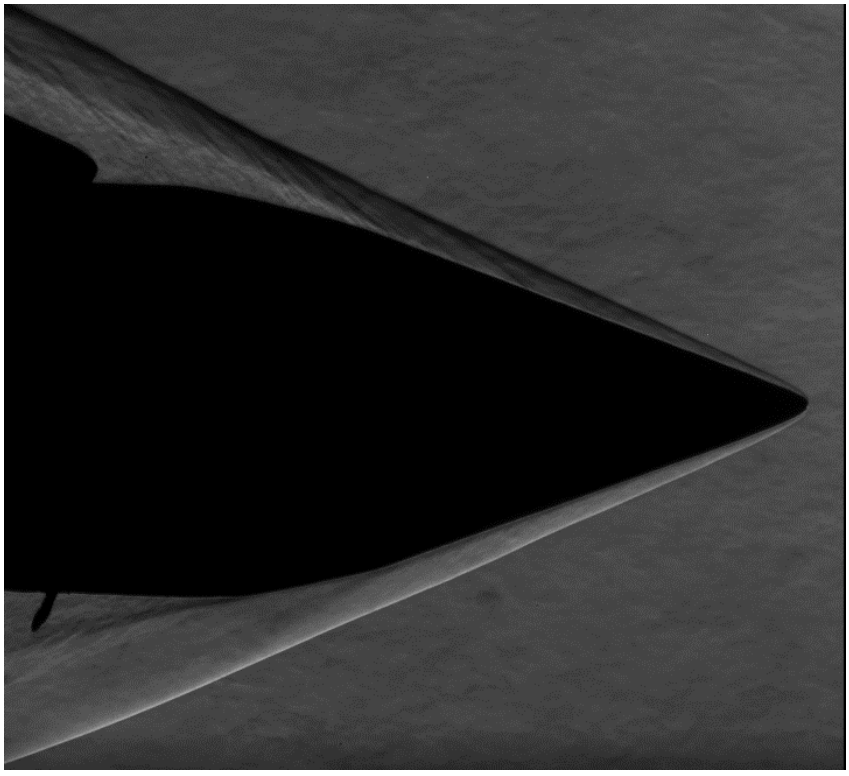

(b) End of 300 psi Run, Simple Cone Model

Figure 55. 300 psi, Simple Cone Images

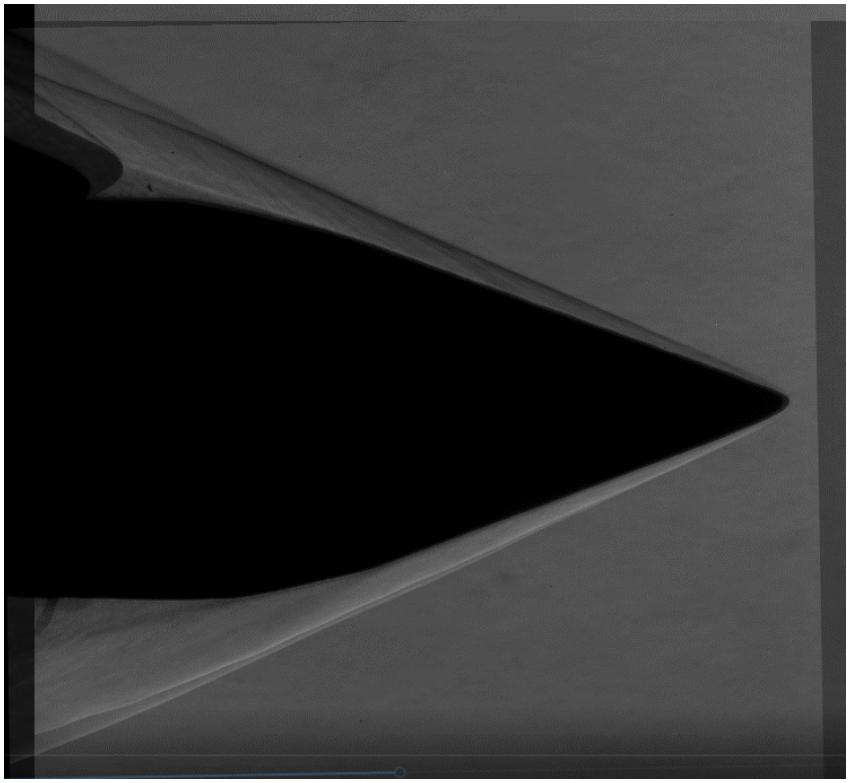

(a) Overlaid Simple Cone Model, 300 psi run

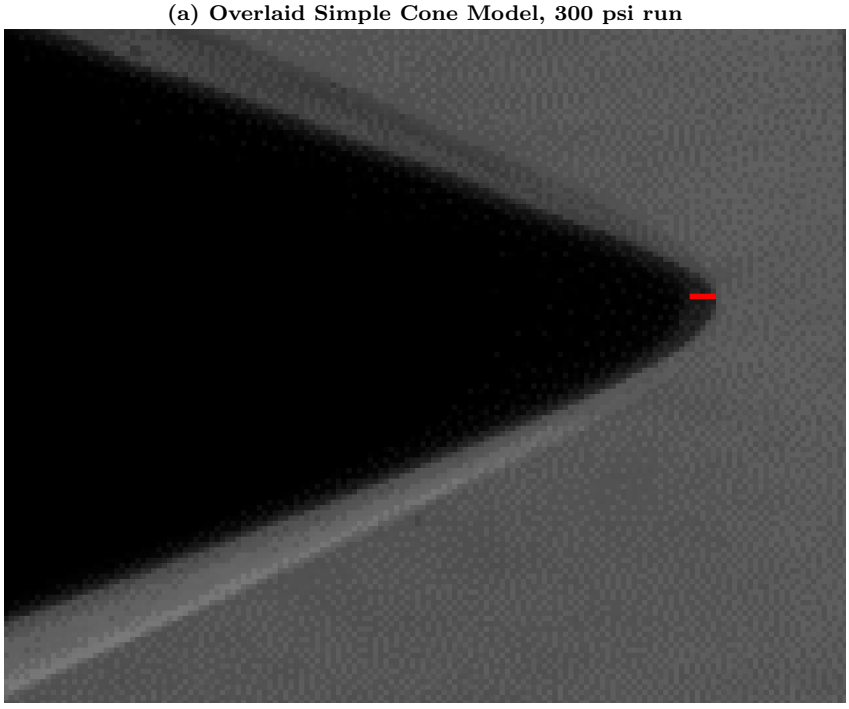

(b) Ablation Measurement of Simple Cone Model, 300 psi run

Figure 56. 300 psi, Simple Cone Measurement

was 4.1 pixels of nose recession, which resulted in an average recession rate of 6.2 mm/s.

4.3.4 Run 39: P_0 = 200 psi, Bi-conic Model

The method for measuring recession rates of the bi-conic models was identical to the simple cone models. Overall, the bi-conic models experienced greater variations of angle of attack compared to the simple cone model. The variation in angle of attack generally ranged from $\pm 5^\circ$, but was approximately 10° in the 300 psi run seen in Figure 48. The bi-conic images could be aligned by both the nose and base portions, which made post-processing less challenging. The image captured at the beginning of quasi-steady period 1 can be seen in Figure 59a, and the image captured at the mid-way through quasi-steady period 2 can be seen in Figure 59b. The time between these images was 0.16 seconds. The images were aligned and overlaid, which can be seen in Figure 60a. Once the images were overlaid, the difference between the nose lengths could be measured, as illustrated in Figure 60b. The average of three measurements was 5.5 pixels of nose recession, which resulted in an average recession rate of 5.6 mm/s.

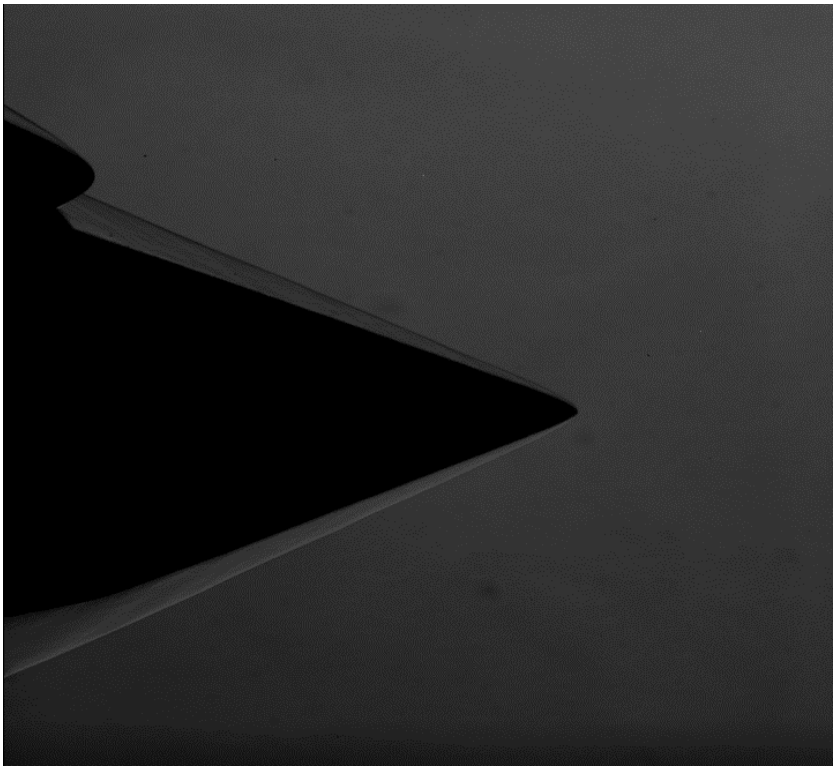

(a) Start of 400 psi Run, Simple Cone Model

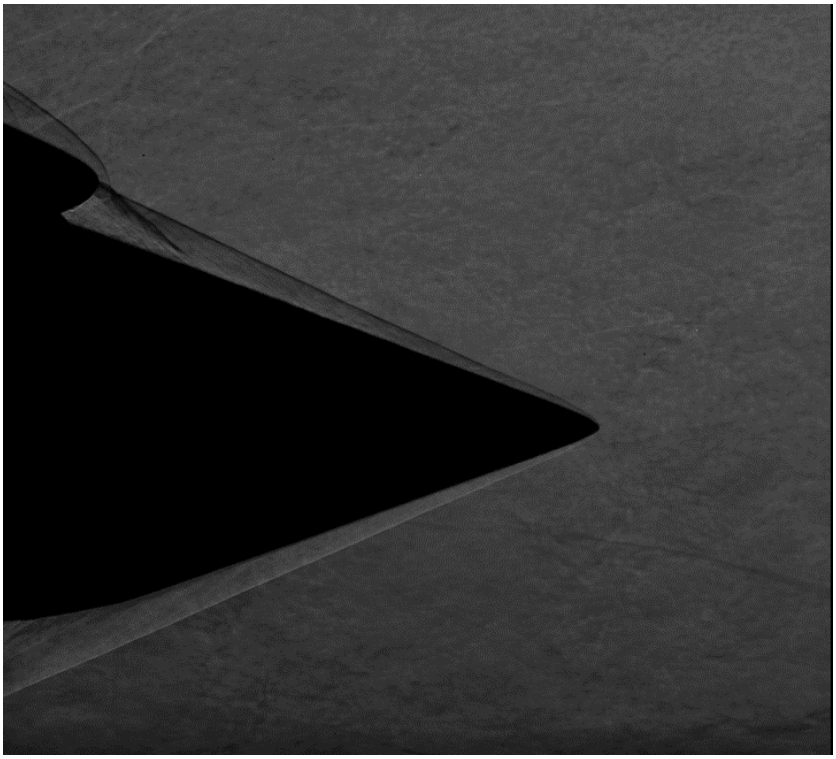

(b) End of 400 psi Run, Simple Cone Model

Figure 57. 400 psi, Simple Cone Images

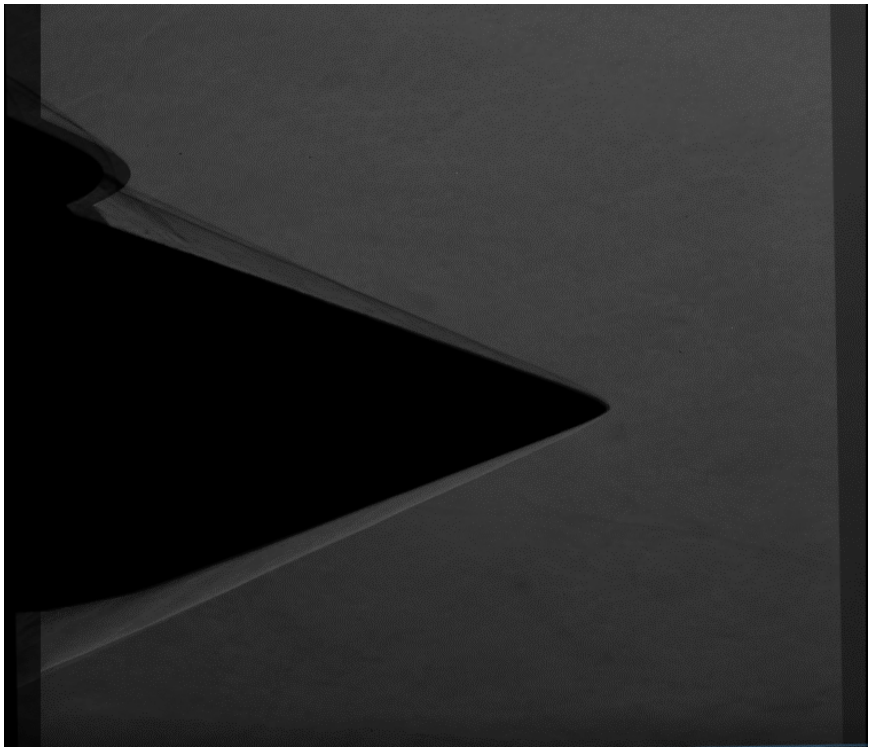

(a) Overlaid Simple Cone Model, 400 psi run

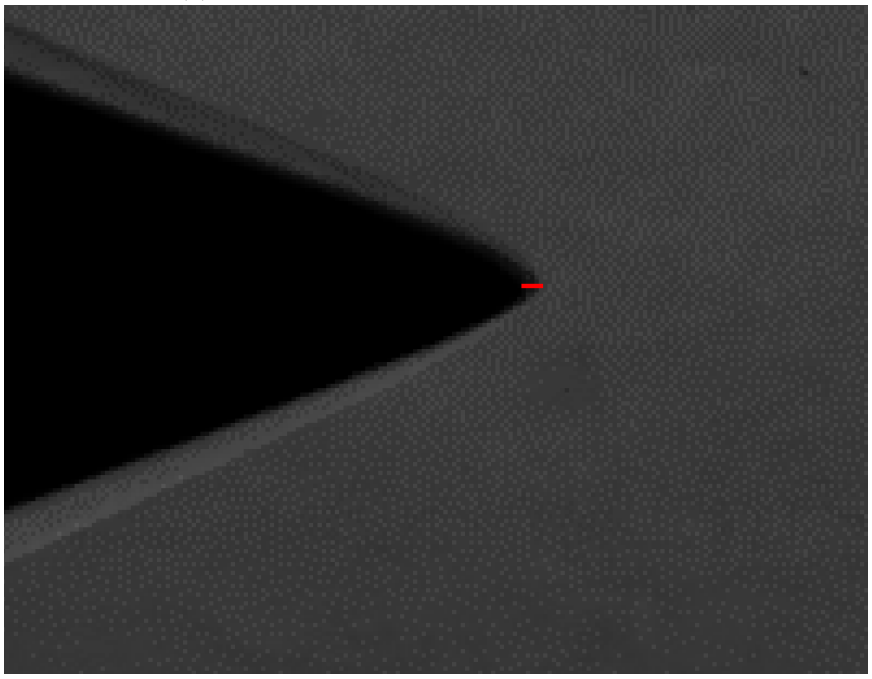

(b) Ablation Measurement of Simple Cone Model, 400 psi run

Figure 58. 400 psi, Simple Cone Measurement

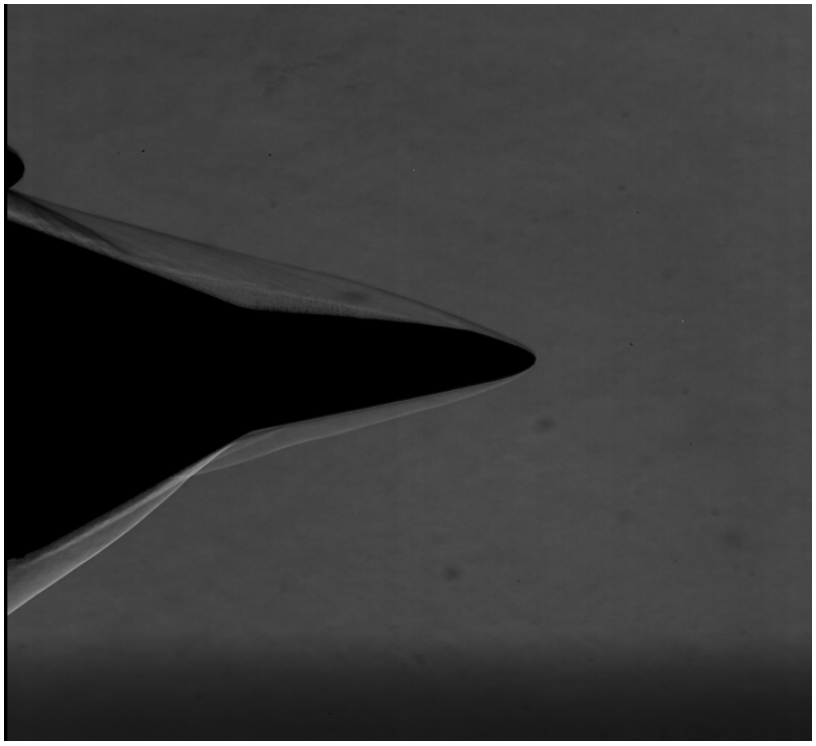

(a) Start of 200 psi Run, Bi-conic Model

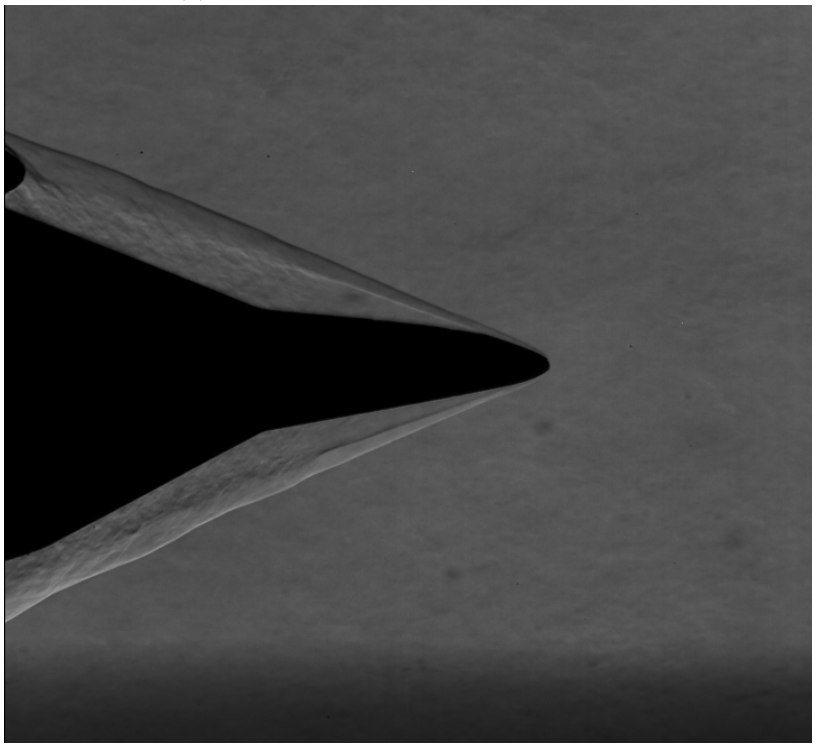

(b) End of 200 psi Run, Bi-conic Model

Figure 59. 200 psi, Bi-conic Images

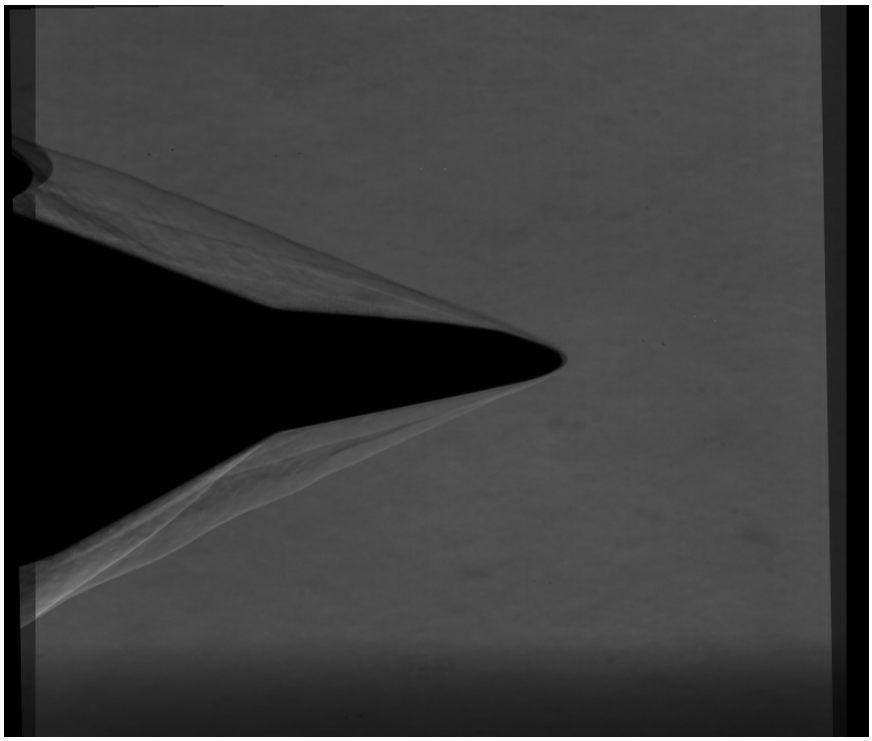

(a) Overlaid Bi-conic Model, 200 psi run

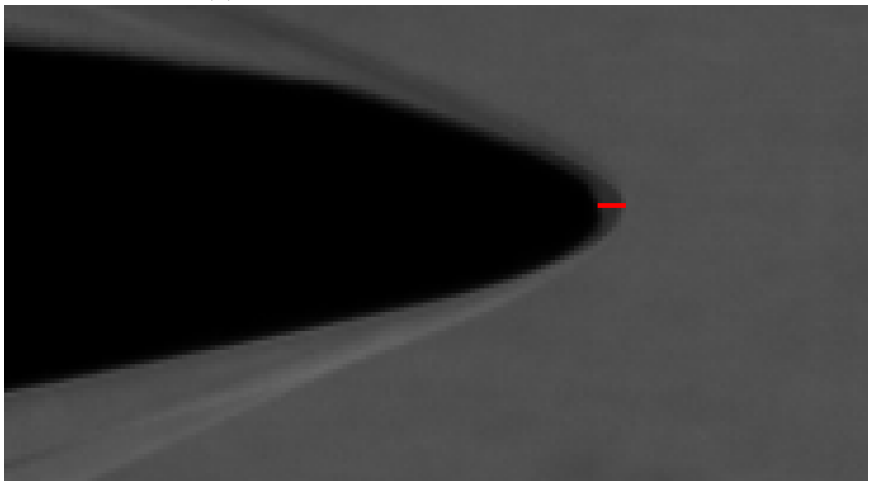

(b) Ablation Measurement of Bi-conic Model, 200 psi run

Figure 60. 200 psi, Bi-conic Model Measurement

4.3.5 Quantitative Results

The methodology outlined in Subsections 4.3.1 - 4.3.4 was repeated for the other 11 test cases that were analyzed. The results of the simple cone model runs are presented in Table 2.

Table 2. Simple Cone Model Results

Nominal P_0 (psi)	**Actual P_0 (psi)**	**Pixels Ablated**	**Run Time (s)**	**Ablation Rate (mm/s)**
100	98.4	2	0.18	1.8
100	99.1	2.7	0.18	2.4
100	100.2	3	0.2	2.3
200	194.2	3	0.17	2.8
200	195.5	5	0.19	4.1
200	196.1	2.5	0.08	5.3
300	295.3	2.8	0.05	8.9
300	291.9	2.5	0.04	9.9
300	293.9	4.3	0.11	6.2
400	394.1	4	0.19	3.4
400	392.4	3.8	0.1	6
400	393.2	5.2	0.17	4.9

A graphical view of the results with error bars accounting for 1/2 pixels of uncertainty can be seen in Figure 61. In general, the nose recession rates tended to increase with stagnation pressure, as expected. The notable exception, however, is the large recession rates recorded for the 300 psi cases. The most likely explanation for this deviation is the 300 psi cases all suffered from early chipping which drastically reduced the run times. While only a pixel or two of nose recession may have been observed, that rate was then extrapolated out when the runs were averaged by time. The result is a high calculated recession rate coupled with a large amount of uncertainty. The average run times for the 100, 200, 300, and 400 psi tests were 0.185, 0.145, 0.066, and 0.154 seconds respectively.

It is possible that the heat transfer rate reduces as the nose blunts due to ablation, resulting in lower recession rates as the run progresses. This implies that the shorter

run times are artificially inflated because they only experience the maximum recession rates. Furthermore, it may be possible that chipping occurred but was not visible to the plane of the camera, resulting in the appearance of ablation when captured within an image. It was generally observed that the shortest run times directly correlated with the largest average recession rate across all stagnation pressures. It is likely that one or both of these effects contributed to the larger recession rates observed during the shortest runs.

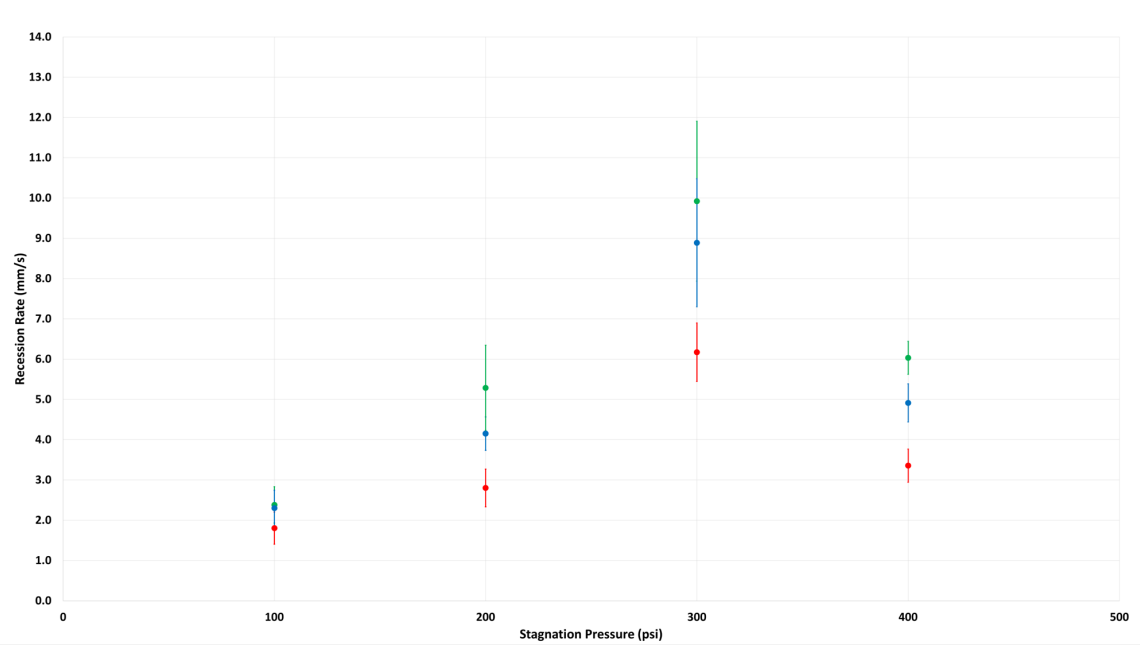

Figure 61. Cone Recession Rates with Error Bars

The results of the bi-conic model tests are presented in Table 3. Data from only a single run at 100, 200, and 300 psi were recorded due to limitations of Ludwieg Tube availability. These reported rates are again averages throughout the run. Unlike many of the simple cone model runs, however, all of these runs lasted through the entirety of quasi-steady period 1 and most of quasi-steady period 2. It is not known why the bi-conic models appeared to be more resistant to chipping compared to the simple cone models. It is possible that the slower manufacturing process produced a

more sturdy model. More runs with the bi-conic model are needed to demonstrate if the design is truly more resistant to chipping.

Table 3. Bi-conic Model Results

Nominal P_0 (psi)	**Actual P_0 (psi)**	**Pixels Ablated**	**Run Time (s)**	**Ablation Rate (mm/s)**
100	100.4	5	0.19	4.2
200	196.8	5.5	0.16	5.5
300	295.0	9	0.2	7.1

A graphical view of the results of the bi-conic model runs with bars accounting for 0.5 pixels of error in each direction can be seen in Figure 62. The bi-conic model appears to follow a more linear growth in recession rate when plotted with stagnation pressure compared to the simple cone model. These results more closely align with the expectation of an increase in recession rate with an increase in stagnation pressure. Additionally, due to the longer run times and greater recession rates, the calculated error for the bi-conic models is less than the error for the simple cone models.

The combination of lower error, higher observed recession rates, and less chipping may indicate that the models with a smaller half-angle might be a better alternative for exploring low-temperature ablation compared to 21° half-angle cones. The greater observed ablation rates of the bi-conic models enabled lower pressure tests to yield equal or greater amounts of nose recession compared to the simple cone model. This allowed lower-pressure tests which generally had fewer adverse effects, such as model movement and chipping, to be used. The bi-conic models were also easier to align during post processing.

4.3.6 Temporal Rate Results

The 300 psi bi-conic test experienced both a full test duration and a large amount of recession. The combination of these factors made it possible to examine the tem-

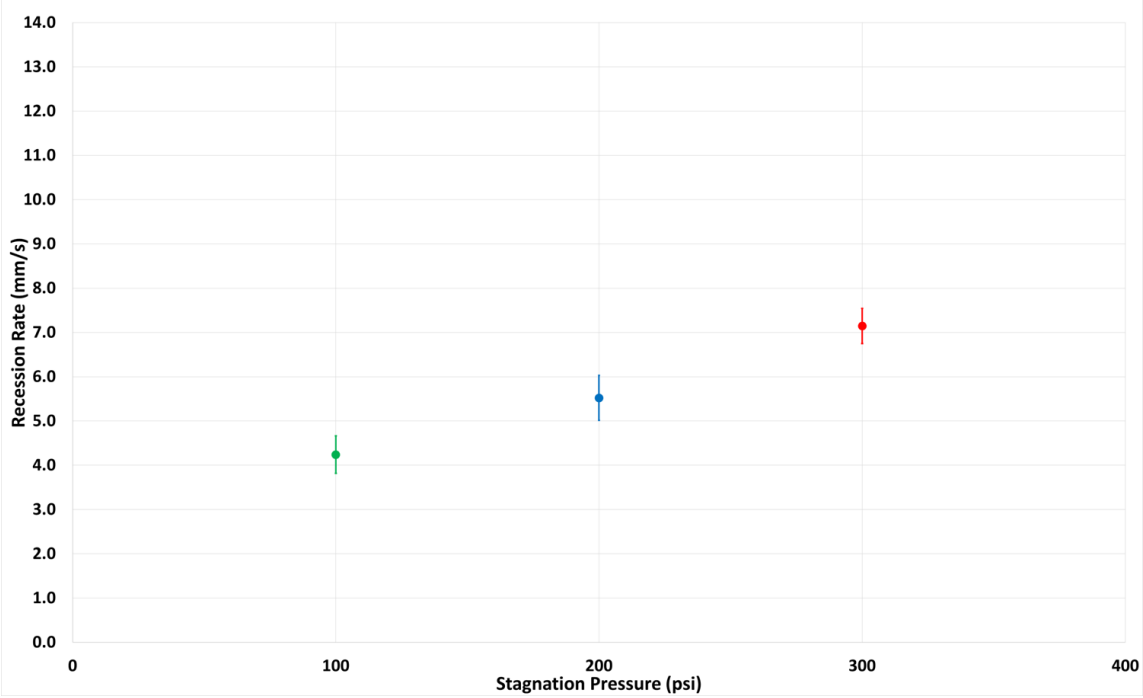

Figure 62. Bi-conic Model Recession Rates with Error Bars

poral recession rate of the dry ice model. Figure 63 shows the recession of the nose at 0.05 second increments. The error bars indicate 0.5 pixels of error to the recession measurement. Figure 64 shows the cumulative recession rate experienced by the model at 0.05 second increments. The error bars in Figure 64 also indicate 0.5 pixels in error. The calculated error decreases in each subsequent measurement as the number of recessed pixels increases. It can be seen in both figures that the recession rate is higher during the first 0.1 seconds of the test, when the leading edge is relatively sharp and the tunnel stagnation pressure is higher.

4.3.7 Stagnation Point Heating

An analytical solution for the convective heat transfer at the stagnation point of a sphere in hypersonic flow is described by the Fay-Riddell correlation. This correlation predicts that the heat transfer at the stagnation point of a hypersonic flow is inversely proportional to the nose radius. This finding, which many considered to be counter-

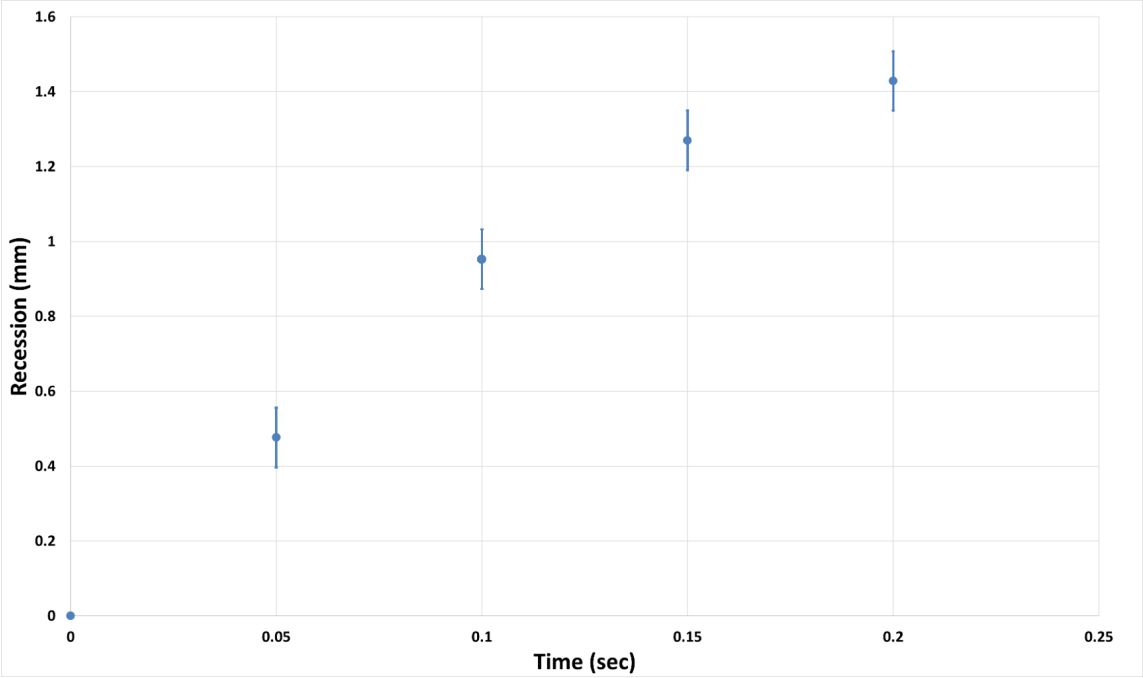

Figure 63. Temporal Recession of Bi-conic Model, 300 psi

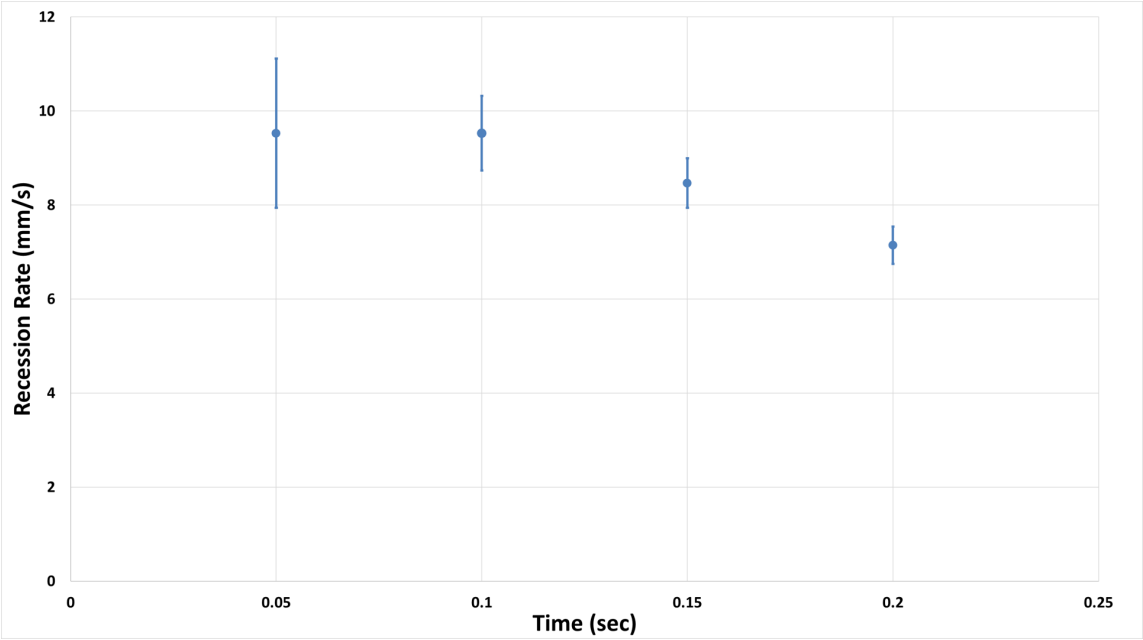

Figure 64. Cumulative Recession Rate of Bi-conic Model, 300 psi

intuitive, has shaped the way re-entry vehicles are designed.

A simplified version of the Fay-Riddell correlation is given by Bertin [4]:

$$\dot{q_s} = K\sqrt{\frac{\rho_\infty}{R_N}}U_\infty^3 \tag{8}$$

where $\dot{q_s}$ is the stagnation point convective heat transfer rate, U_∞ is the freestream velocity, ρ_∞ is the freestream density, R_N is the effective nose radius, and K is a heat-transfer factor. K is a function of the molecular weight, mass fraction, and transport parameter of the gas or mixture.

This correlation allows the stagnation point heating for vehicles of different sizes, velocities, and altitudes to be estimated via a relatively simple formula. It also opens up new methods of analysis for the dry ice model ablation rate, and can help provide context to the recession rates calculated in previous sections. A modified version of Equation 8 can be used to normalize the ablation rate results. By approximating the heat transfer rate with the observed ablation rate, and given that U_∞ equal for each run, the test results can be normalized by $\sqrt{\frac{\rho_\infty}{R_N}}$. This normalization will cause the results to converge to an approximation of the heat transfer factor.

The nose radius for each model was determined by overlaying a circle that matched the contour of the model leading edge onto the temporal sequence images that were used to determine the ablation rate. The radius of that circle could then be determined by using the ImageJ measuring tool. An example of this process on a bi-conic model can be seen in Figure 65. Another example of the measurement on a simple cone model can be seen in Figure 66. The nose radius measurement was performed on both images for each run, and an average nose radius was used for the calculation. An average of the first and second quasi-steady period freestream densities was also used for these calculations, with the exceptions of the runs that were too short to enter the second quasi-steady period.

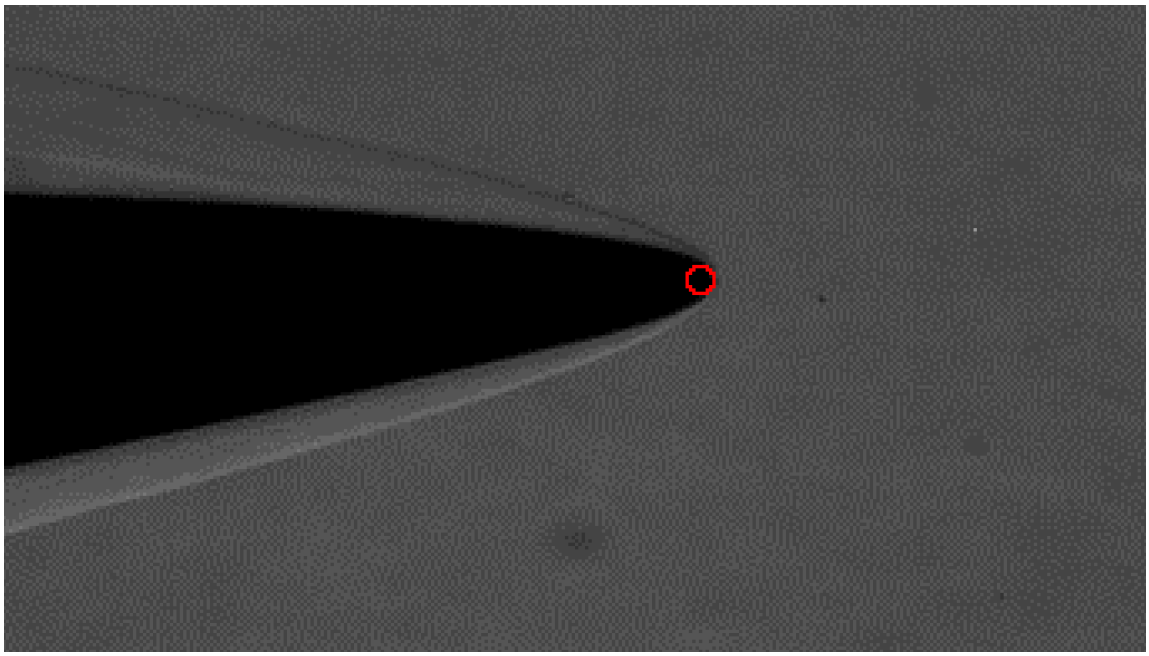

Figure 65. Estimating Nose Radius of a Bi-conic Model

Figure 67 shows the normalized recession rates for each run without error bars. The black data points represent the simple cone model, and the red data points represent the bi-conic model. Again, the 300 psi results for the simple cone model are likely over-estimations due to their short run time, but the 100, 200, and 400 psi data points appear to become more closely aligned. While only three points are examined, the bi-conic data points also appear to approach a constant.

The correlation in Equation 8 assumes that the total enthalpy of the freestream is much larger than the wall. This is true for most hypersonic environments, but it is not so for this research. A form of the Fay-Riddell correlation that includes an enthalpy ratio adjustment is given by Tauber et al. [31]:

$$\dot{q_s} = K\sqrt{\frac{\rho_\infty}{R_N}}(1 - g_w)(U_\infty^3) \tag{9}$$

where g_w is the ratio of wall enthalpy to total enthalpy. If the effects of conduction into the solid and radiation are neglected, then the heat flux leading to sublimation can

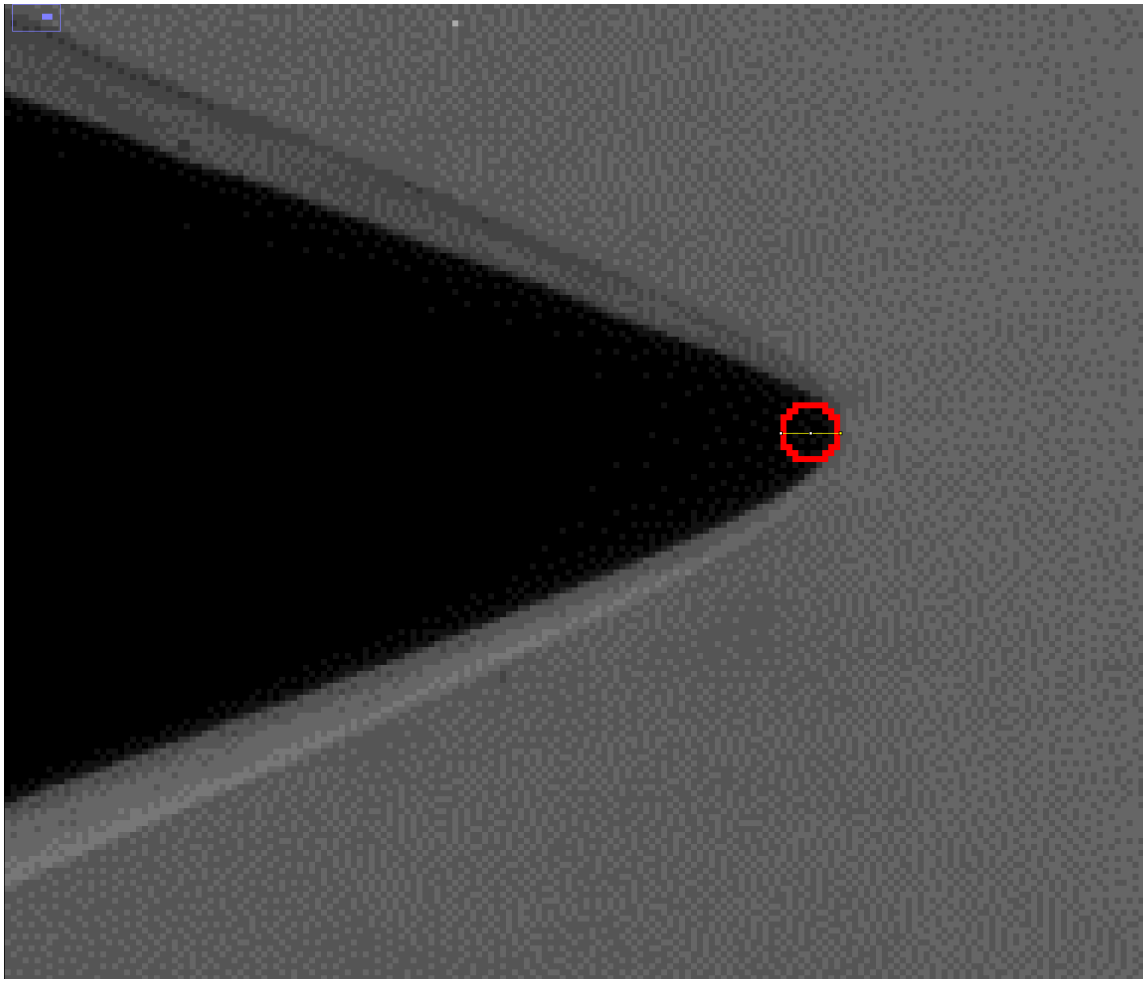

Figure 66. Estimating Nose Radius of a Cone Model

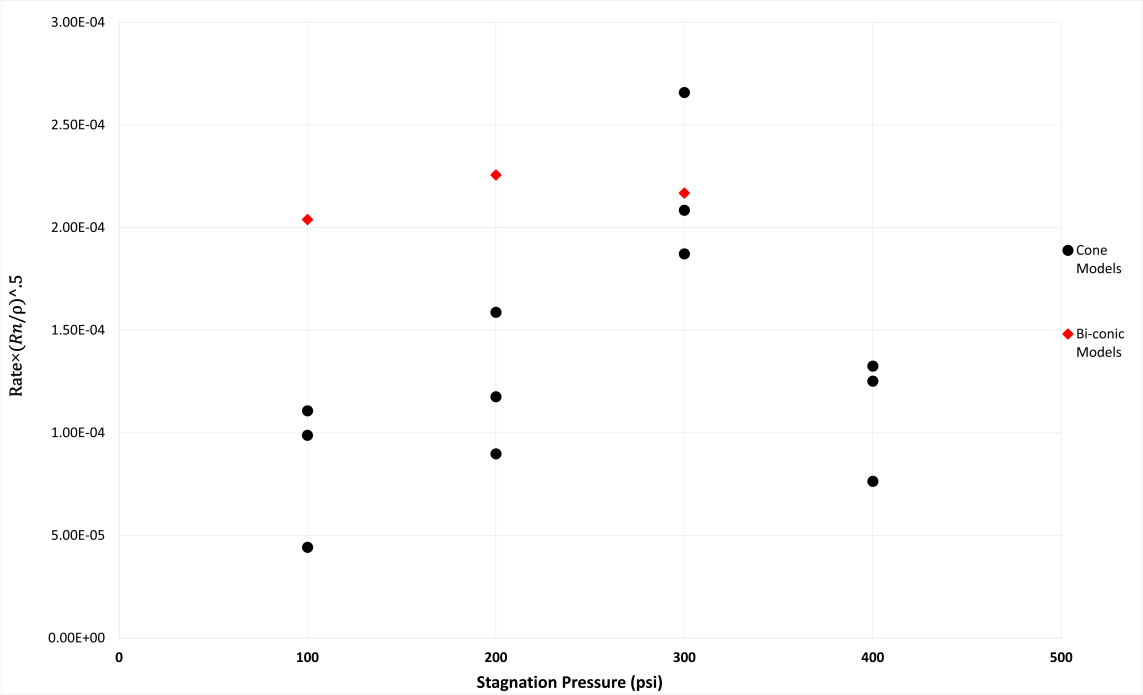

Figure 67. Normalized Recession Rates of all Runs

also be directly calculated if the recession rate is known with the following equation:

$$\dot{q_s} = \text{Recession rate} \times H_{\text{sub}} \times \rho_{CO_2} \tag{10}$$

where H_{sub} is the enthalpy of sublimation (571,000 J/kg) and ρ_{CO_2} is the density of the dry ice model (1400 kg/m^3). By using Equations 9 and 10, a value for K can be calculated and compared to the value prescribed by the Tauber et al.

The values for the 300 psi bi-conic run were first used for this analysis. Like the previous analysis, the averaged values for freestream density, nose radius, freestream velocity, and recession rates were used. The ratio of wall enthalpy to total enthalpy was calculated by the following equation:

$$g_w = \frac{c_{p1} T_{wall}}{c_{p2} T_0} \tag{11}$$

where c_{p1} is the specific heat capacity of the medium, T_{wall} is the wall temperature

(temperature of the dry ice model in this case), c_{p2} is the specific heat capacity of the flow, and T_0 is the stagnation temperature, which was 490K for all runs. The surface temperature of the dry ice was approximated to be 181K, which is the sublimation temperature of dry ice at the local stagnation pressure. The value of g_w was calculated to be 0.37 if air is assumed to be the gas at the surface of the model and a temperature of 181K. By contrast, the value of g_w was calculated to be 0.26 if gaseous CO_2 is assumed to be at the surface of the model and a temperature of 181K. The difference in g_w values is due to the lower value of specific heat capacity for CO_2. The calculated K constant values for the bi-conic model at 300 psi are 3.6 x 10^{-8} and 3.1 x 10^{-8} using the g_w values for air and CO_2 respectively. The Fay-Riddell correlation spells out 1.83 x 10^{-8} as the value for K according to Tauber et al. [31]. The K values given by these values are an overestimate, but the bi-conic models also experienced the greatest recession rates. When the calculation was repeated for a 200 psi run using a simple cone model, the result was an estimate of 2 x 10^{-8} and 1.7 x 10^{-8} using g_w for air and g_w for CO_2 respectively, which is in closer agreement with the literature.

This process was repeated for the 13 other test cases. The results of these calculations can be seen in Figures 68 and 69. The error bars were calculated by assuming an error of 0.5 pixels to both the measured nose recession and nose radius. The error values assumed an overestimation of both recession and nose radius for the positive values and an underestimation for the negative values. This results in the maximum error for each case. The black data points represent the simple cone models, the red represent bi-conic models, and the purple line is the K value given by Tauber et al.

It can be seen in both Figures 68 and 69 that the bi-conic model consistently overestimated the value of K. The simple cone model at stagnation pressures of 100, 200, and 400 psi, however, has many values at each pressure that approach the value

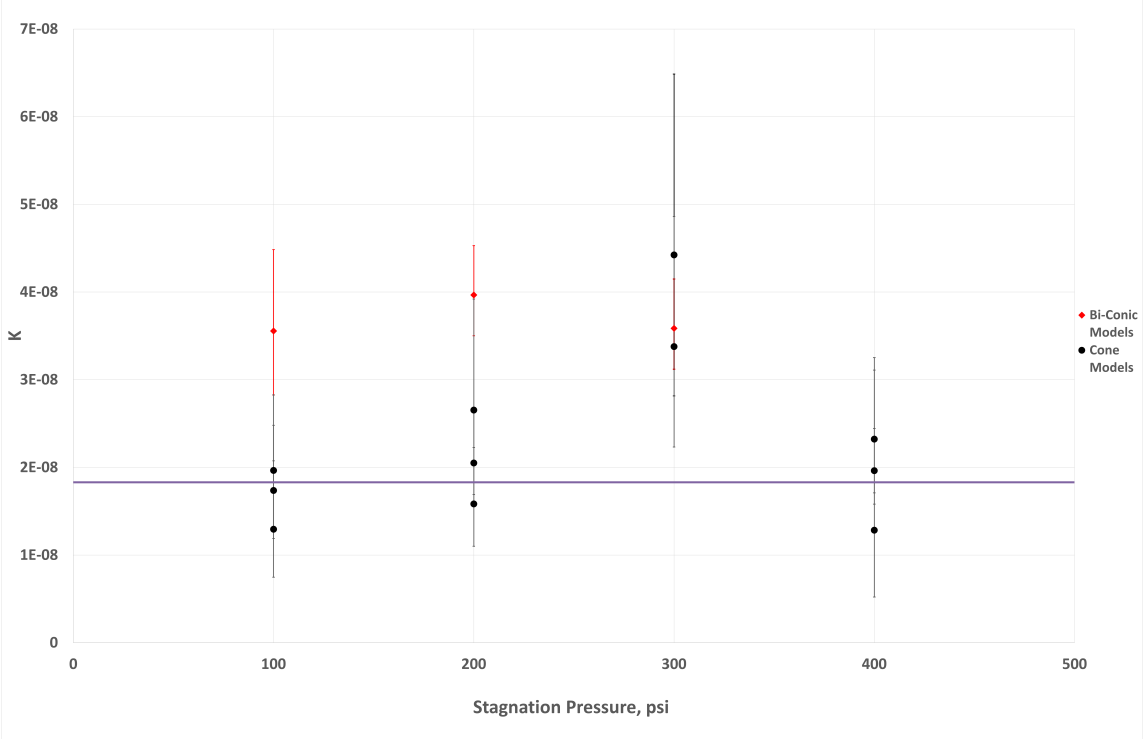

Figure 68. K Estimation using Air g_w

given by Tauber et al. When using g_w for air in this calculation, 3 of the 15 runs are within 10% of the value from literature, and 5 are with 20%. When using g_w for CO_2, 4 of the 15 runs are within 10% of the value from literature, and 5 were within 20%. This may indicate that dry ice models in the conditions created by the Ludwieg Tube can provide a reasonable approximation of flight vehicles in re-entry conditions.

It is likely that the 300 psi results are over-estimations of the true recession rate due to the shortened run times, which artificially increased the average recession rate, and therefore the calculated heat flux. It is also possible that the geometry of the bi-conic models caused the consistent overestimation of the K value. The nose radius of the bi-conic model extends for a longer duration compared to the simple cone model. This increases the observed recession rate, but may also impact the effective nose radius used in this correlation.

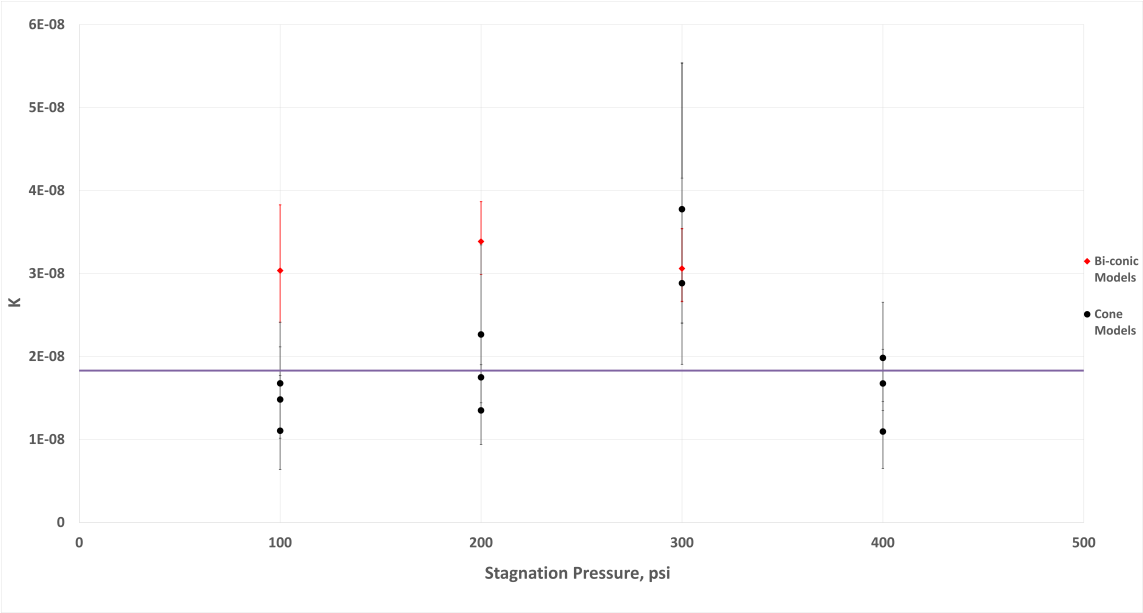

Figure 69. K Estimation using CO_2 g_w

V. Conclusions and Recommendations

Chapter 5 presents a summary of the research, significant findings of this research, and recommendations for future research.

5.1 Summary of Research

The purpose of this study was to explore the prospects for use of dry ice models in a low enthalpy tunnel to simulate the high-temperature ablation encountered by hypersonic vehicles in extreme flight conditions. This study developed a repeatable, systematic process for fabricating dry ice models with a high success rate, and created a methodology to test low-temperature ablators in the AFRL Mach 6 Ludwieg Tube. Upon developing this methodology, tests were performed to observe ablation characteristics of dry ice in a hypersonic flow, observe the coupling of shape change and ablation pattern, and explore boundary layer changes due to ablation products.

Tests were accomplished stagnation pressures of 100, 200, 300, and 400 psi, using both simple cone and bi-conic models. The unit Reynolds number varied from 2.6 x 10^6 to 23 x 10^6 m^{-1}. Schlieren visualization, paired with a high-speed camera, was used to capture nose recession at a frame rate of 20,000 FPS and a shutter speed of 249 ns. A continuous stream of liquid nitrogen was used to cool the surface of the dry ice holder to a temperature below 150 K to prevent sublimation during the tunnel charging time.

The ablation rate of each test was determined by measuring the nose recession between temporal schlieren images of the dry ice models. These results were normalized by freestream density and nose radius and were compared to stagnation point heating engineering methods from literature.

5.2 Significant Findings

Previous research by Callaway and others showed that the integrity of dry ice models posed a challenge. At the outset, this research was an exploratory endeavor into the capability of using dry ice models within the AFRL Ludwieg tube. A significant achievement of this effort was developing the method of forming models with aluminum molds utilizing commercially produced dry ice. This method significantly reduced the rate of failure during the manufacturing process compared to previous research. Additionally, these models were able to consistently survive the hypersonic environment produced by the Ludwieg Tube.

Furthermore, this research showed that increased stagnation pressures and narrower leading edges increased the observed ablation rate. Recession rates could be calculated by aligning images and measuring the difference in nose length. The nose radius could also be approximated by inscribing a circle that matched the contour of the nose tip and measuring the radius. The observed ablation rates began to converge when normalized by nose radius and freestream density across the spectrum of stagnation pressures. This study was somewhat limited by the camera resolution, but this can be overcome in future research with a different camera lens.

It was also found that if the assumption that all of the heat transfer at the stagnation point was directed to sublimation phase change, then a heating rate could be calculated. This heating rate compared favorably to the engineering method derived from the Fay-Riddell correlation. An estimate for the heat transfer factor could be backed out using the known freestream conditions, nose radius, and calculated heat flux. Five of the nine cone models returned estimates of the heat transfer factor that were within 20% of the value given in literature. Three (assuming air at the model surface) and four (assuming CO_2 at the model surface) of these estimates were within 10% of the value given in literature.

Finally, this research can conclude that dry ice models may be a useful in performing hypersonic store separation tests within the Ludwieg Tube. It was generally observed that ice models that were ejected during the runs did not travel too far down into the vacuum chamber of the Ludwieg Tube, and never caused any damage. Dry ice has the added benefit of easy clean up due to its low-temperature sublimation.

5.3 Recommendations

This research built upon Callaway's efforts in the AFIT small supersonic tunnel and established that dry ice models are a viable method for capturing ablation data in hypersonic flows within a Ludwieg Tube. There are several paths of future study that can be done from this work. Additionally, several recommendations can be made to improve the methodology of research similar to this.

One of the primary challenges was creating a reliable manufacturing process for constructing models suitable for testing within the Ludwieg Tube. While the one that was developed proved to be suitable, various improvements could be made. First, molding the dry ice models required standing in place for 10-15 minutes at a time holding the base of the model upright as it slowly sublimated downwards. Doing this by hand caused slight variations in the model angle of attack, which was particularly noticeable in the bi-conic models. Devising a method to hold the model upright against the mold should reduce this variability, as well as free up the researcher to perform other tasks. Additionally, using multiple molds simultaneously will greatly accelerate the process.

Another challenge was the dry ice models were in near-continuous motion throughout the run. This made post-processing image analysis more challenging and forced the viewing window to encompass a wider picture to insure the model did not move out of frame. Future research may explore the use of spring steel to keep constant

tension on the dry ice, or a "cheese grater design" where the ice can be slid in one direction but resists motion in another.

Once the issue of mid-run movement is solved, improving the resolution and zoom level of the schlieren imagery may enable capturing data that was not possible in this research. Better resolution at the nose will result in more accurate recession rate calculations. A higher frame rate further down the body may be able to capture laminar to turbulent transition due to mass addition. Higher resolutions and frame rates would allow much more accurate data to be captured and could lead to better identifying chipping versus ablation. The recession rates during the first and second quasi-steady periods could be compared to see what effect short run times have on average recession rates.

Appendix A. Safety Report

1.1 Introduction

This report evaluates the risk associated with utilizing dry ice (solid CO_2) models to both the AFRL Ludwieg Tube facility and personnel.

1.2 Personnel Safety

While CO_2 is generally considered to be non-toxic, it can present health hazards when it displaces oxygen in the air. The Occupational Safety and Health Administration (OSHA) uses a standard of 19.5% oxygen as the level below which an oxygen-deficient atmosphere exists. Human beings experience increasingly adverse health effects as the oxygen level drop below 19.5%. Concentrations of 16 to 19.5% are not fatal but are generally associated with increased breathing rates, accelerated heartbeat, and impaired thinking and coordination. Even a momentary loss of coordination could be devastating to the personnel or equipment if it occurs during the performance of a potentially dangerous activity, such as entering or exiting the test section [26].

To ensure safety to lab personnel, a limit of 19.5% oxygen was used to determine the maximum amount of CO_2 that could be present without harming personnel. For this analysis, it was assumed that the full volume of dry ice would sublimate and remain within the test section. The test section has a volume of $15.8m^3$ and is assumed to be at standard conditions of 300 K and 1 atm. Additionally, the base concentrations of N_2 and O_2 were assumed to be 78% and 21% respectively. Using these assumptions the amount of N_2 and O_2 present in the test section were determined to be 13.89 and 4.27 kg respectively [32]. The O_2 mole fraction, χ_{O_2}, was calculated by first determining each species mass fraction and mixture molecular

weight through the following equations:

$$Y_i = \frac{m_i}{m_{total}} \tag{12}$$

$$MW_{mixture} = \frac{1}{\sum \frac{Y_i}{MW_i}} \tag{13}$$

Where m_i is the total mass of species, Y_i is the species mass fraction, $MW_{mixture}$ is the mixture molecular weight, and MW_i is the species molecular weight. From there, the O_2 mole fraction was calculated by:

$$\chi_{O_2} = \frac{Y_{O_2} MW_{mixture}}{MW_{O_2}} \tag{14}$$

These calculations were performed with a range of CO_2 values to determine the maximum safe amount. It was found that 2.4 kg of CO_2 corresponded to a χ_{O_2} of 0.195. Therefore, to ensure the safety of personnel the dry ice models must be less than 2.4 kg. A similar analysis was performed on the basement atmosphere to determine the number of tests that could be accomplished before rendering it unsafe. Using a maximum test article mass of 2.4 kg, as well as the equations above, it was found that it would take 380 consecutive tests without air exchange to render the basement atmosphere unsafe.

1.3 Facility Safety

Another risk presented by the use of dry ice models is large pieces breaking off during tunnel operation. For this analysis, it was assumed that a dry ice sphere with a mass of 2.4 kg and a diameter of 14.32 cm completely detaches from the test stand and is propelled down the shaft. These calculations were done at the highest Reynolds number, which corresponded to values of Mach 6.1, a freestream temperature, T_∞, of

57.9 K, and a freestream pressure, P_∞, of 2106 Pa.

This analysis assumed that the only forces acting on the dry ice sphere were drag, which results in the equation:

$$\sum F = ma_x = C_D q S \tag{15}$$

where m is the model mass, a_x is 1-D acceleration, C_D is the drag coefficient, q is dynamic pressure, and S wetted surface area. Furthermore, the dynamic pressure is defined by $q = \frac{1}{2}\rho_\infty V_\infty^2$, where ρ_∞ is the freestream air density and V_∞ is the freestream velocity. The diameter of the sphere was calculated using a mass of 2.4kg and a density of 1562 kg/m^3. The speed of sound, a, was calculated by:

$$a = \sqrt{\gamma R T_\infty} \tag{16}$$

where γ is the ratio of specific heats, R is the universal gas constant. For this case, the gas was assumed to be calorically perfect ($\gamma = 1.4$) and R was 287.06 $\frac{J}{kg \cdot K}$. Freestream density, ρ_∞, was calculated through the equation of state for a perfect gas, $P_\infty = \rho_\infty R T_\infty$, and S was simply area of the sphere normal to the direction of the oncoming flow. According to Bailey and Hiatt, a reasonable drag coefficient for a sphere in hypersonic flight is $C_d = 0.901 - \frac{0.462}{M^2}$, which was used for this analysis [3].

A first order explicit Euler method was used to calculate the drag force, acceleration, and velocity of the sphere at each time step until it reached a shaft length of 10.3 meters. The impact velocity was determined to be 77.37 m/s. Plots of the distance vs time and distance vs velocity data can be seen in Figure 70 and Figure 71 respectively.

The blast shield in the vacuum tank was designed to survive the impact of a 7.4 gram stainless steel ball with a 9.4 mm diameter striking at 93 m/s. While the dry ice

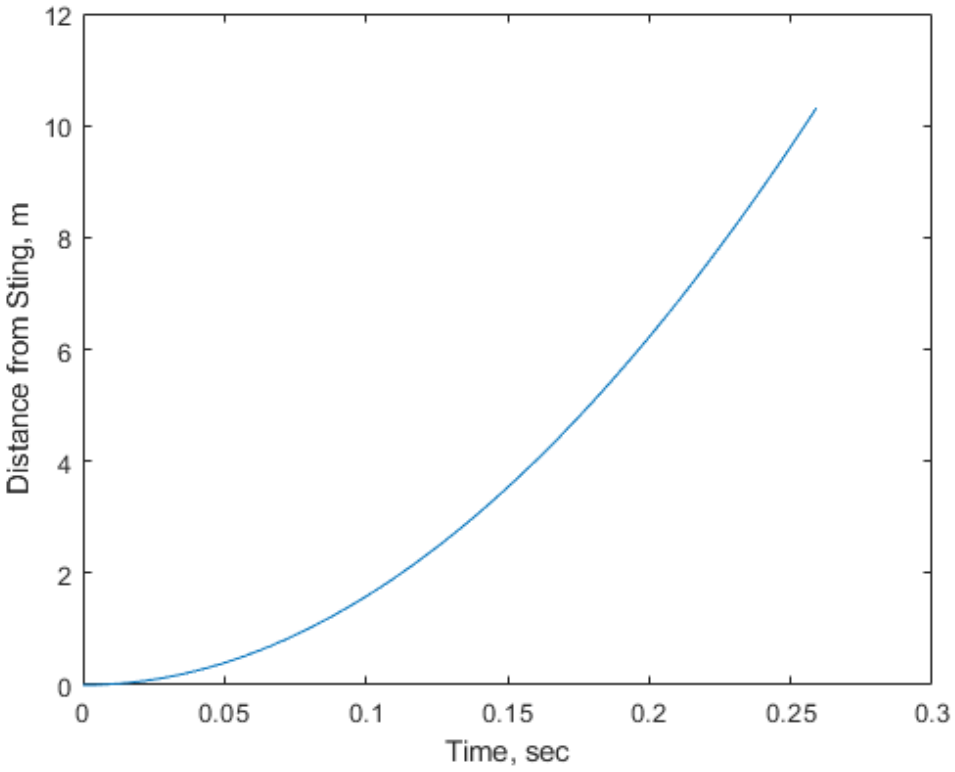

Figure 70. Dry Ice Sphere Distance vs Time

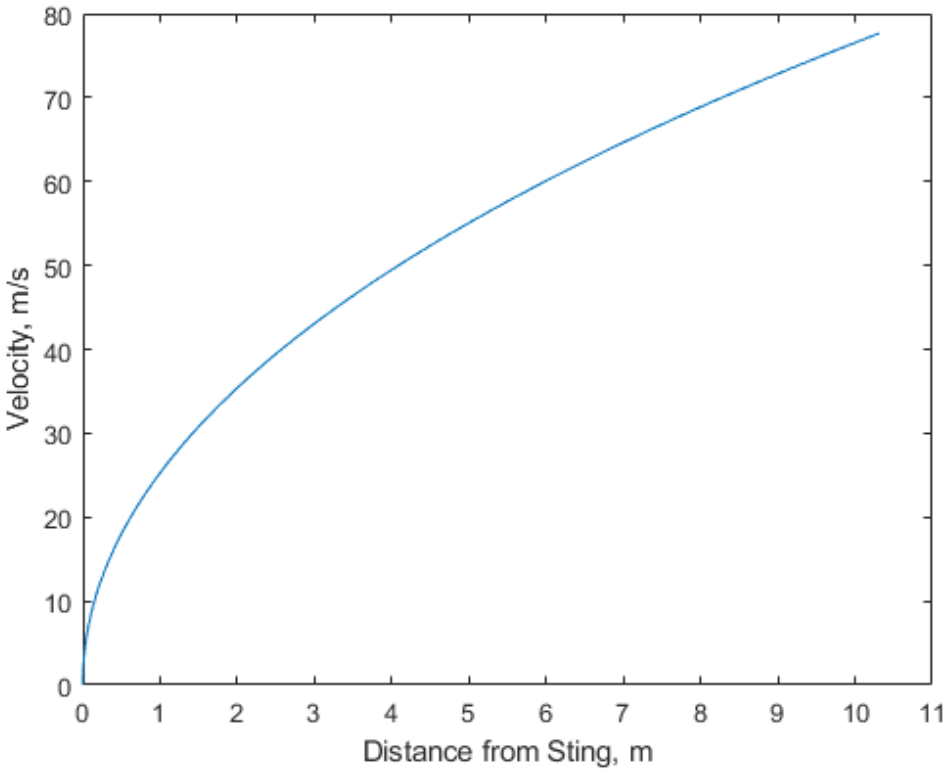

Figure 71. Dry Ice Sphere Distance vs Velocity

sphere contains significantly more kinetic energy due to its larger mass, that energy is imparted into the blast shield over a much larger area. The impact area was assumed to be the surface area of the sphere normal to the wall, or 0.0161 m^2. The ice sphere imparts about 97% of the energy per unit area compared to the stainless steel ball. This analysis, however, neglects the dynamics of a true collision between the dry ice sphere and the blast shield. Dry ice is not a particularly strong substance and shatters when dropped only a small distance. It is therefore reasonable to assume that a significant portion of the energy of the impact would be consumed by deforming the sphere itself rather than the blast shield. The force of this impact can be determined by dividing the energy of the impact by the crumple distance of the imposing object, which for the dry ice sphere would likely be the entire diameter of 0.1432 m. Dividing this force by the area of the impact results in the pressure exerted by the colliding object onto the blast shield. By making the conservative assumption that the stainless steel ball would also completely deform during the impact, it was determined that the dry ice sphere would only impart 6% of the pressure onto the blast shield compared to the stainless steel ball.

1.4 Recommendations

The risk to personnel and facility equipment will be drastically reduced by adhering to the maximum model mass recommendation and properly securing the model during tunnel operation. Additionally, the lab area is already equipped with O_2 sensors to ensure a safe working environment. Recommend approval for testing.

1.5 Dry Ice Holder

A dry ice holder was designed to secure the dry ice molds during tunnel operation that would minimize risks to the facility and influence the flow. After several iterations, the following design was chosen:

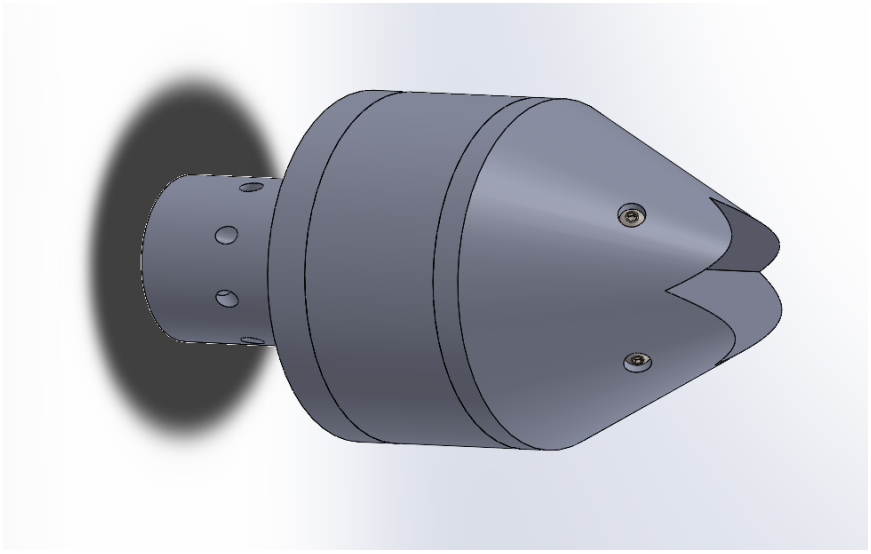

(a) Dry Ice Holder, Isometric view

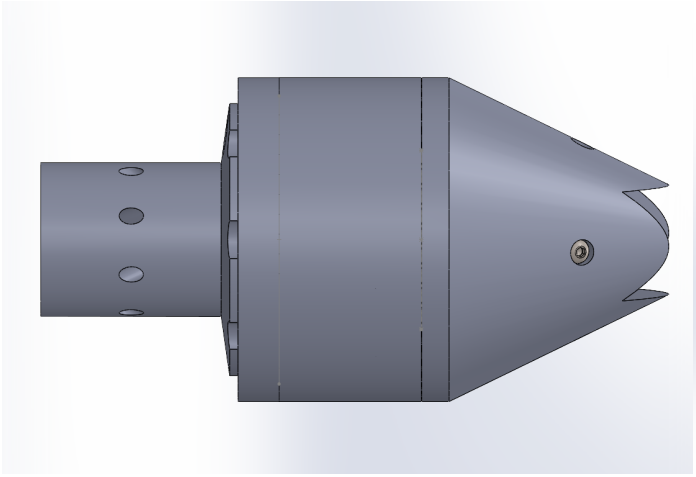

(b) Dry Ice Holder, Side view

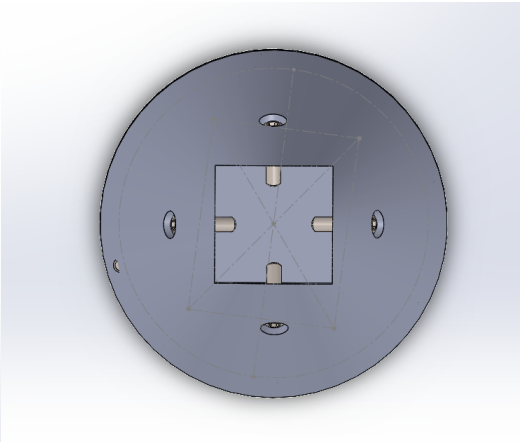

(c) Dry Ice Holder, Front view

The block of dry ice will be slid through the opening at the front and will then be formed into a cone by using a heated mold. The base of the holder that attaches to the tunnel sting shares the same design as previously tested models. The base has proven to be reliable, and therefore was not subject to this analysis. Screws will be

placed through the sides to hold the dry ice in place throughout the tests. The entire holder will be constructed from 303 stainless steel.

1.6 Dry Ice Holder Stress Analysis

A worst-case scenario for the Ludwieg Tube startup was analyzed to ensure the safety of the tunnel during tests. A normal shock propagates downstream after the actuation of the fast valve. The pressure across the normal shock can be calculated via normal shock relation, which is given by Oddo [27]

$$\frac{P_{t1}}{P_{t0}} = \left[\frac{(\gamma+1)M^2}{(\gamma-1)M^2+2}\right]^{\frac{\gamma}{\gamma-1}} \left[\frac{\gamma+1}{2\gamma M^2-(\gamma-1)}\right]^{\frac{1}{\gamma-1}} \tag{17}$$

where P_{t1} is the stagnation pressure downstream of the normal shock, P_{t0} is the stagnation pressure upstream of the normal shock, γ is the ratio of specific heats (assumed to be 1.4), and M is the freestream Mach number (6.1). The resulting downstream stagnation pressure across the shock under these conditions is 16.6 psia.

A worst-case scenario where the inside of the holder is pressurized while the outside is still at a vacuum was evaluated for this analysis. Additionally, it was also assumed that one half of the dry ice experienced pressure from the flow while the other half was at vacuum, resulting in a moment acting upon the holder. A simplified 2D static analysis was performed to determine the moment acting upon the dry ice that was similar to the methodology done by Oddo [27]. The cone profile was represented by an isosceles triangle, with a center of pressure located 1.66 inches from the base (1/3 of the height). In this model, that moment was resisted by only a single leading edge of the holder, which is also the thinnest part. In reality, there would be numerous other forces counter-acting the force from startup. This analysis should be fairly conservative. The free-body diagram below shows the forces acting upon the body, and the calculations to find the resultant force are:

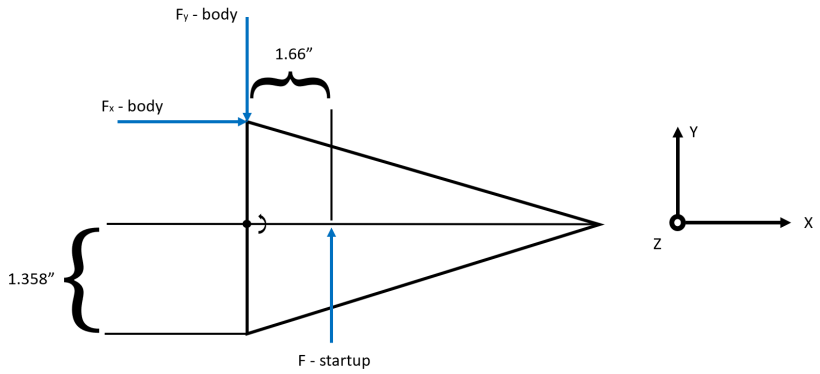

Figure 73. Free Body Diagram

Area of triangle: 1/2 x Base x Height = (0.5)(3 in)(5 in) = 7.5 in^2

Force on the cone: Pressure x Area = (16.6 lb/in^2)(7.5 in^2) = 124.5 lb

Sum of the moments:

$\sum_{Z}^{CCW+}$ M = ($F_{startup}$)(D_x) - (F_{x-body})(D_y) = (124.5 lb)(1.66 in) - (F_{x-body})(1.358 in)

The resultant force resisting the rotation induced from the moment is 152.8 lbs. The only forces in the y-direction are the startup force and body force which resists it. The internal pressure and forces were applied to the holder, and a stress analysis was performed using the Finite Element Analysis (FEA) toolbox built into SolidWorks. The material properties for 304 stainless steel were selected in the simulation because 303 stainless steel was not available. The material properties are comparable, but 304 SS has a lower yield strength than 303 SS. This analysis will underestimate the factor of safety of the constructed dry ice holder. The material properties for various medals are shown below [27]:

The FEA analysis produced by SolidWorks can be seen in Figure 74. SolidWorks predicted a maximum stress of 1.317 x10^4 psi, which was well below the yield strength of 3 x 10^4 psi. This results in a factor of safety of 2.69. A plot showing the safety factor of the holder can be seen in Figure 75.

Material Property	303 SS	304 SS	316 SS	6061-T6 Aluminum
Ultimate Tensile Strength (MPa)	620	505	550	124
Yield Tensile Strength (MPa)	240	215	240	55.2
Modulus of Elasticity (GPa)	193	193-200	193	68.9
Coefficient of Thermal Expansion, Linear 20°C (µm/m-°C)	17.2	17.3	16	23.6
Thermal Conductivity at 100°C (W/m-K)	16.2	16.2	16.3	180*
Density (g/cm^3)	8	8	8	2.7

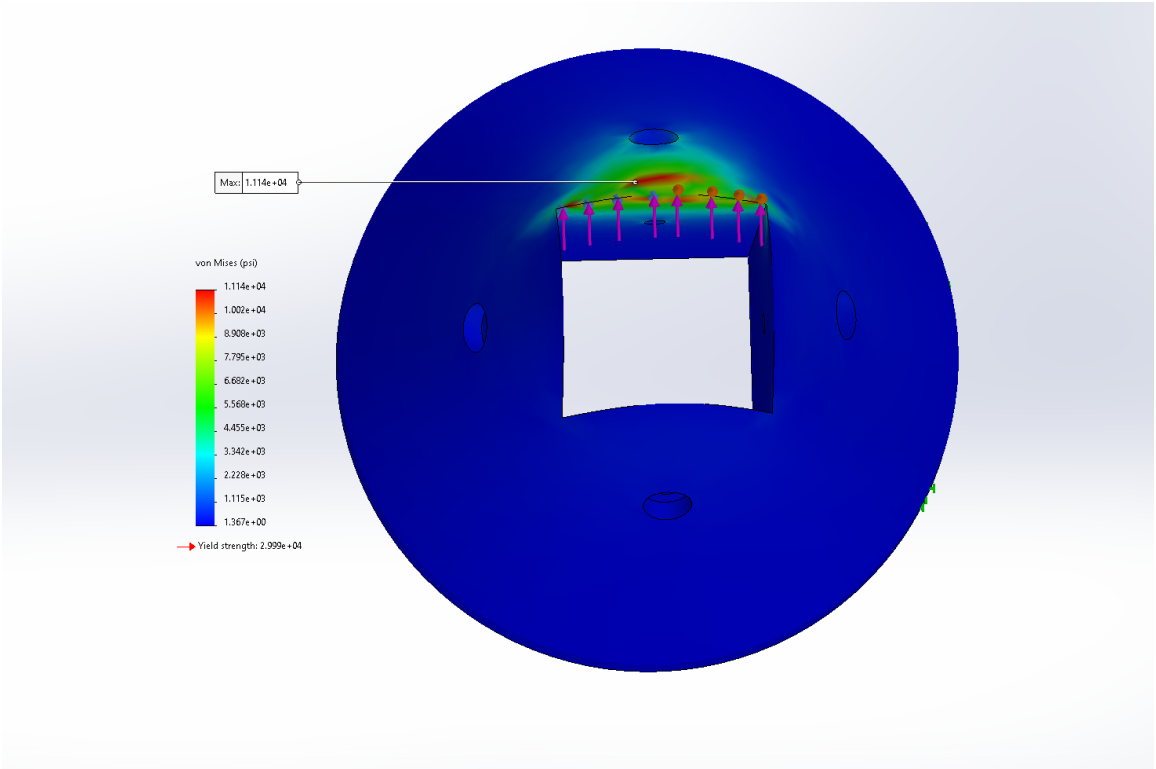

Figure 74. SolidWorks Stress Analysis

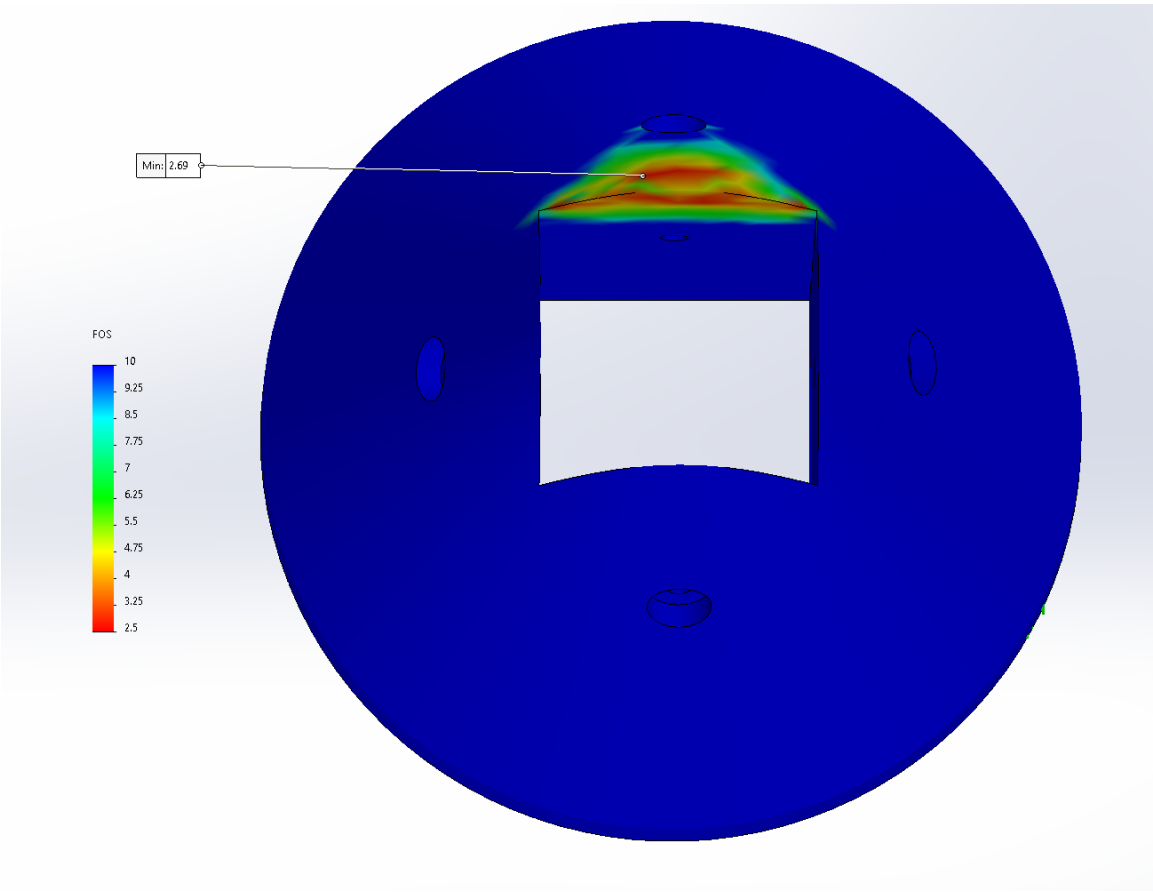

Figure 75. Factor Of Safety

Another structural concern surrounds the screws affixing the cone part of the holder to the base. For this analysis, the truncated conic stainless steel section of the holder and the dry ice block were treated as a single cone. The truncated cone was extrapolate out to where the leading edge would be if the dry ice block portion was not present. The forces on the bolt were calculated in a similar manner to the steps perform above.

Area of triangle: 1/2 x Base x Height = (0.5)(5.89)(6.32 in) = 18.6 in^2

Force on the cone: Pressure x Area = (16.6 lb/in^2)(18.6 in^2) = 308.97 lb

Sum of the moments:

$\sum_Z^{CCW+}$ M = ($F_{startup}$)(D_x) - (F_{bolt})(D_y) = (308.97 lb)(2.1in) - (F_{bolt})(2.75 in)

F_{bolt} = 236.7 lb

Cross-sectional area of the bolt: $A_c = (\pi/4)(D^2) = (\pi/4)(0.25\text{ in})^2 = 0.049\text{ in}^2$

M Effective Area: $A_{eff} = (\pi/4)(5.89\text{ in})^2 = 27.25\text{ in}^2$

The resulting tensile stress acting on a single bolt:

$\sigma_{bolt} = F_{Bolt}/A_c$ = (236.7 lb)/(0.049 in^2) = 4,821 psi

Factor of safety using a single bolt: FS = $\sigma_{ultimate}/\sigma_{Bolt}$ = (170,000 psi)/(4,821 psi) = 35.25

This analysis suggests that a single bolt provides more than adequate support to the dry ice model holder. The holder contains 8 bolts in total, so the total safety factor for the component is much greater than the safety factor predicted above.

It is commonly recommended to tighten screws to 75% of their yield strength to

ensure a secure connection [27].

$\sigma_{Bolt} = \sigma_{torque}$ - $\sigma_{startup}$

σ_{Bolt} = (0.75)(34,809 psi) - $\sigma_{startup}$ = 21,285 psi

Including this additional stress reduces the safety factor to 4.35. Given that these calculations are conservative in nature and still result with with a safety factor greater than 1, it is reasonable to apply the recommended torque to the 8 bolts.

Torque = Friction coefficient x Bolt Diameter x Tensile load

A friction coefficient of 0.2 is a reasonable for bolts with a plain finish [27].

Torque = (0.20)(1/4 in)(21,285 psi x A_C) ÷ (12 in) = 4.44 ft·lb.

1.7 Recommendations

Given that this was a simplified analysis with conservative assumptions, it is recommended that the proposed dry ice holder should be approved for testing within the AFRL Ludwieg Tube facility.

Appendix B. Ludwieg Tube Runs

Table 4. Ludwieg Tube Runs

Run #	**Nominal P_0 (psi)**	**Actual P_0 (psi)**	**Test Article**
1	40	55.0	Empty Holder
2	40	45.0	Simple Cone
3	100	100.0	Simple Cone
4	200	195.1	Simple Cone
5	100	98.1	Simple Cone
6	150	145.4	Simple Cone
7	300	296.1	Simple Cone
8	100	98.4	Simple Cone
9	150	146.5	Simple Cone
10	300	296.9	Simple Cone
11	200	194.2	Simple Cone
12	300	295.3	Simple Cone
13	400	394.0	Simple Cone
14	400	394.1	Simple Cone
15	500	495.5	Simple Cone
16	500	496.5	Simple Cone
17	500	494.9	Simple Cone
18	100	95.2	Simple Cone
19	200	193.3	Simple Cone
20	200	195.1	Simple Cone
21	100	99.5	Simple Cone
22	300	295.4	Simple Cone

23	400	393.2	Simple Cone
24	300	291.9	Simple Cone
25	400	392.4	Simple Cone
26	200	195.5	Simple Cone
27	200	195.2	Simple Cone
28	200	195.4	Simple Cone
29	200	195.6	Simple Cone
30	100	99.1	Simple Cone
31	200	196.1	Simple Cone
32	100	100.2	Simple Cone
33	300	293.9	Simple Cone
34	300	293.9	Simple Cone
35	100	98.9	Bi-conic
36	400	393.2	Simple Cone
37	300	294.6	Simple Cone
38	100	100.4	Bi-conic
39	200	196.7	Bi-conic
40	200	196.8	Bi-conic
41	200	195.5	Bi-conic
42	300	295.0	Bi-conic

Bibliography

1. Anderson, D. E. [1960], Investigation of ablation of ice bodies in hypersonic flows, Master's thesis, California Institute of Technology, Pasadena, CA.

2. Anderson, J. D. [2006], Hypersonic and High Temperature Gas Dynamics, 2 edn, American Institute of Aeronautics and Astronautics, Inc, Reston, Virginia.

3. Bailey, A. and Hiatt, J. [1971], 'Free-flight measurements of spher drag at subsonic, transonic, supersonic and hypersonic speeds for continuum, transition, and near-free-molecular flow conditions', Aedc-Tr-70-291 p. 97.

4. Bertin, J. J. [1994], Hypersonic Aerothermodynamics, 1 edn, American Institute of Aeronautics and Astronautics, Inc, Washington, DC.

5. Callaway, D. [2011], 'Photogrammetric Measurement of Recession Rates of Low Temperature Ablators Subjected To High Speed Flow', Air Force Institute Of Technology .

6. Callaway, D. W., Reeder, M. F., Greendyke, R. B. and Gosse, R. C. [2014], 'Ablation measurements and analysis of solid carbon dioxide models at Mach 3', Journal of Spacecraft and Rockets **51**(1), 213–225.

7. Combs, C. S., Clemens, N. T., Danehy, P. M. and Murman, S. M. [2017], 'Heatshield ablation visualized using naphthalene planar laser-induced fluorescence', Journal of Spacecraft and Rockets **54**(2), 476–494.

8. Cummings, R. M. [2022], 'Summary of progress for the dod hpcmp hypersonic vehicle simulation institute', AIAA Science and Technology Forum and Exposition, AIAA SciTech Forum 2022 pp. 1–11.

9. Curry, D. [1992], 'Thermal protection systems manned spacecraft flight experience', NASA Langley Research Center, Current Techology for Thermal Protection Systems pp. 19–41.

10. Davenport, C. [2020], 'Spacex is reinforcing heat shield of its dragon spacecraft ahead of planned october flight', Washington Post .

11. Embrador, J. C. [2021], 'Effects of Highly-Cooled Walls on Hypersonic Boundary Layer Transition and Turbulence'.

12. Field, M. and Louis, S. [n.d.], 'allation of the Galileo Probe Heat Shield AIAA / ASME 3rd Joint Thermop Fluids , Plasma and Heat Transfer Conference'.

13. Fletcher, D. [2014], Funamentals of hypersonic flow - aerothermodynamics, Technical report, von Karman Istitute, Belgium.

14. Gnoffo, P. A. [2007], 'A perspective on computational aerothermodynamics at NASA', Proceedings of the 16th Australasian Fluid Mechanics Conference, 16AFMC (December), 24–31.

15. Hankey, W. [1998], Re-Entry Aerodynamics, American Institute of Aeronautics and Astronautics, Inc., Washington, DC.

16. Hanson, R. [1968], Characterization of high enthalpy flows, Technical report, Stanfod University.

17. Hill, J. L. [2021], 'Experimental measurements of hypersonic instabilities over ogive-cylinders at mach 6'.

18. Kimmel, R. L., Borg, M., Jewell, J. S., Lam, K. Y., Bowersox, R., Srinivasan, R., Fuchs, S. and Mooney, T. [2017], 'AFRL ludwieg tube initial performance', AIAA SciTech Forum - 55th AIAA Aerospace Sciences Meeting (January).

19. Kohlman, D. L. and Richardson, R. W. [1969], 'Experiments on the use of dry ice ablating wind-tunnel models', Journal of Spacecraft and Rockets **6**(9), 1061–1063.

20. Labuda, D., Komives, J., Reeder, M. F., Borg, M. and Jewell, J. S. [2020], 'Schlieren imaging on cone variations in the afrl ludwieg tube facility', Aiaa Aviation 2020 Forum **1**, 1–18.

21. Laganelli, A. L. and Nestler, D. E. [1969], 'Surface ablation patterns - A phenomenology study', AIAA Journal **7**(7), 1319–1325.

22. Larson, H. and Mateer, G. [1968], 'Cross-hatching - A coupling of gas dynamics with the ablation process', (68).

23. Mason, W. [2016], 'Configuration aerodynamics'.

24. Moretti, G. and Abbett, M. [2003], 'A Time-Dependent Computaional Method for Blunt Body Flows', Journal of Spacecraft and Rockets **40**(5), 736–741.

25. Nachtsheim, P. R. and Larson, H. K. [1971], 'Crosshatched ablation patterns in Teflon', AIAA Journal **9**(8), 1608–1614.

26. Occupational Health and Safety Administration [2011], 'Occupational Safety and Health Standards - Respiratory Protection, Standard No. 1910.134'. https://www.osha.gov/laws-regs/regulations/standardnumber/1910/1910.134, accessed 2021-09-20.

27. Oddo, R. [2020], High-speed schlieren imaging of second mode disturbances in a super-cooled hypersonic boundary layer, Master's thesis, Air Force Institute of Technology, Wright-Patterson AFB, OH.

28. Onay, O. K. and Eyi, S. [2020], 'Ablation analyses of optimized nose tips for hypersonic vehicles', Journal of Thermophysics and Heat Transfer **34**(1), 78–89.

29. Pavlosky, J. and St Leger, L. [1974], Apollo experience report - thermal protection subsystem, Technical report, NASA TN D-7564.

30. Sherman, M. [1968], Entry thermal protection, Technical report, NASA SP-8014.

31. Tauber, M. E., Menees, G. P. and Adelman, H. G. [1987], 'Aerothermodynamics of transatmospheric vehicles', Journal of Aircraft **24**(9), 594–602.

32. Turns, S. R. [2012], An Introduction to Combustion, 3 edn, McGraw-Hill, New York, New York.

33. van Driest, E. [1952], Investigation of laminar boundary layer in compressible fluids using the crocco method, Technical report, NACA TN 2597.

34. van Driest, E. [1956], 'The problem of aerodynamic heating', Aeonautical Engineering Review (October), 26–41.

35. Zibitsker, A. L., McQuaid, J. A., Brehm, C. and Martin, A. [2022], 'Fully-Coupled Simulation of Low Temperature Ablator and Hypersonic Flow Solver', AIAA Science and Technology Forum and Exposition, AIAA SciTech Forum 2022 pp. 1–27.

REPORT DOCUMENTATION PAGE

Form Approved
OMB No. 0704–0188

1. REPORT DATE *(DD–MM–YYYY)*	2. REPORT TYPE	3. DATES COVERED *(From — To)*
24–03–2022	Master's Thesis	August 2020 — March 2022

4. TITLE AND SUBTITLE

Exploratory Measurement of Recession Rates of Low Temperature Ablators Subjected to Mach 6 Flow

5a. CONTRACT NUMBER

5b. GRANT NUMBER

5c. PROGRAM ELEMENT NUMBER

6. AUTHOR(S)

Kellet, Ross H., Capt, USAF

5d. PROJECT NUMBER

5e. TASK NUMBER

5f. WORK UNIT NUMBER

7. PERFORMING ORGANIZATION NAME(S) AND ADDRESS(ES)

Air Force Institute of Technology
Graduate School of Engineering and Management (AFIT/EN)
2950 Hobson Way
WPAFB OH 45433-7765

8. PERFORMING ORGANIZATION REPORT NUMBER

AFIT-ENY-MS-22-M-296

9. SPONSORING / MONITORING AGENCY NAME(S) AND ADDRESS(ES)

Air Force Research Laboratory
2145 5th Street, BUilding 24c
WPAFB, OH 45433-7542
(937) 713-6697 matthew.borg.3@us.af.mil

10. SPONSOR/MONITOR'S ACRONYM(S)

11. SPONSOR/MONITOR'S REPORT NUMBER(S)

12. DISTRIBUTION / AVAILABILITY STATEMENT

Approval for public release; distribution is unlimited.

13. SUPPLEMENTARY NOTES

14. ABSTRACT

The high speed/high-temperature effect of heat shield ablation was simulated in the low-enthalpy AFRL Mach 6 Ludwieg Tube using solid dry ice as a low-temperature sublimator. The experiments utilized both 21° half-angle cones and bi-conic models with a 7° half-angle leading edge followed by a 26° half-angle base contained within a cryogenic-cooled stainless steel holder. A method of fabricating dry ice test articles was developed using commercially procured dry ice and custom-made aluminum molds. Tests were performed at Mach 6.1 with a stagnation temperature of 490 K and stagnation pressures ranging from 40 - 500 psi. Unit Reynolds number ranged from 2.6 x 10^6 to 23 x 10^6 m^{-1}. High-speed Schlieren photography with a frame rate of 20 kHz was used for visualization and data analysis. The observed ablation rates compared favorably to previous research and were analyzed using the Fay-Riddell stagnation point heating correlation. This exploratory effort demonstrated the potential for other uses of dry ice test models in the facility, including for store separation experiments and localized particle-based flow visualization.

15. SUBJECT TERMS

Low Temperature Ablation, Hypersonics, Recession, Convective Heat Transfer, Stagnation Point, Dry Ice, High-Speed Flow

16. SECURITY CLASSIFICATION OF:			17. LIMITATION OF ABSTRACT	18. NUMBER OF PAGES	19a. NAME OF RESPONSIBLE PERSON
a. REPORT	b. ABSTRACT	c. THIS PAGE			Dr. Mark Reeder, AFIT/ENY
U	U	U	U	129	19b. TELEPHONE NUMBER *(include area code)* (937) 255-3636 x4530; mark.reeder@afit.edu